

6-28-2010

Progress in metamaterials : magnetic hybridization of electric dipole resonance and inhomogeneous structures for thin-film lenses

Svyatoslav Smolev

Follow this and additional works at: https://digitalrepository.unm.edu/ece_etds

Recommended Citation

Smolev, Svyatoslav. "Progress in metamaterials : magnetic hybridization of electric dipole resonance and inhomogeneous structures for thin-film lenses." (2010). https://digitalrepository.unm.edu/ece_etds/239

This Dissertation is brought to you for free and open access by the Engineering ETDs at UNM Digital Repository. It has been accepted for inclusion in Electrical and Computer Engineering ETDs by an authorized administrator of UNM Digital Repository. For more information, please contact disc@unm.edu.

**PROGRESS IN METAMATERIALS: MAGNETIC
HYBRIDIZATION OF ELECTRIC DIPOLE RESONANCE
AND INHOMOGENEOUS STRUCTURES FOR
THIN-FILM LENSES**

BY

SVYATOSLAV SMOLEV

M.S., Physics, Ural State Technical University, 2002
M.S., Optical Science, University of New Mexico, 2006

DISSERTATION

Submitted in Partial Fulfillment of the
Requirements for the Degree of

**Doctor of Philosophy
Engineering**

The University of New Mexico
Albuquerque, New Mexico

May 2010

© 2010, Svyatoslav Smolev

To My Parents and My Wife

Acknowledgments

First of all, I gratefully acknowledge Dr. Steven R. J. Brueck, my advisor and dissertation chair, for his inspiration, guidance, support and encouragement throughout the course of this work and for his assistance in, my professional development. He constantly stimulated and challenged my analytical thinking and greatly assisted with my scientific writing. I would like to give my special thanks to my committee members, Dr. Kevin Malloy, Dr. Jean-Claude Diels, Dr. Payman Zarkesh-Ha and Dr. Michael Sinclair for their valuable comments on my dissertation.

I greatly appreciate the collaboration and support of my friends and colleagues at the Center for High Technology Materials. Sincerer gratitude is extended to the past and present members of our research group and staff at CHTM, for their friendship and support during all of those years.

To my parents for their unconditional love, support and encouragement.

And finally to my wife Kira, your encouragement, comments, patience and love are the strongest support for the fulfillment of this work.

**PROGRESS IN METAMATERIALS: MAGNETIC
HYBRIDIZATION OF ELECTRIC DIPOLE
RESONANCE AND INHOMOGENEOUS STRUCTURES
FOR THIN-FILM LENSES**

BY

SVYATOSLAV SMOLEV

ABSTRACT OF DISSERTATION

Submitted in Partial Fulfillment of the
Requirements for the Degree of

**Doctor of Philosophy
Engineering**

The University of New Mexico
Albuquerque, New Mexico

May 2010

**Progress in Metamaterials: Magnetic Hybridization of Electric Dipole
Resonance and Inhomogeneous Structures for Thin-Film Lenses**

by

Svyatoslav Smolev

M.S., Physics, Ural State Technical University, 2002

M.S., Optical Science, University of New Mexico, 2006

Ph.D., Engineering, University of New Mexico, 2010

ABSTRACT

From earlier theoretical work and practical implementation, understanding of negative index metamaterials (NIMs) has advanced rapidly. Much effort has been put into extending NIMs in the near-infrared (NIR) and in visible regions, where simple scaling of the magnetic response of the structures used for RF breaks down at the NIR. As a solution, a new structure in the form of a fishnet has emerged, and has been shown to successfully act as a new metamaterial in the infrared and visible regions. Attention in the research community is now turning to the direct applications. Here we report progress in the field of metamaterials for the magnetic hybridization of the electric dipole resonance and inhomogeneous metamaterial structures.

From the fundamental and, possibly, application points of view, it is of interest to consider the coupling between the metamaterial magnetic resonance and electric dipole resonances of the absorbing species located in the metamaterial unit cell.

Simple resonance coupling model and numerical rigorous coupled wave analysis (RCWA) were used to investigate the effect of adding a dielectric with a dipole absorption peak to a fishnet metamaterial. *Anti-crossing behavior and an exchange of oscillator strength* as the metamaterial structural resonance is tuned through the absorption resonance were obtained. Response of the NIM structure with a dielectric material without an absorber shows only a single resonant peak, resulting from the coupling of the broadband negative ϵ with the structurally resonant negative μ associated with the LC circuit between the two metal plates. With the addition of a dipole absorber in the dielectric, the NIM exhibits doubly resonant behavior. Presence of an *electric dipole* resonance in the dielectric of the fishnet structure manifests itself in a modification of the *magnetic permeability*, which in turn modifies the negative index behavior. A set of experimental samples were fabricated using standard lithographic processing. An Al-BCB-Al fishnet structure was used. Transmission data was obtained by FTIR. Plotting positions of the resonance peaks in the transmission response against ω_0 clearly shows coupling between the resonances with hybridization behavior

First step in development of possible application for the metamaterials was done by Driscoll in 2006. He demonstrated a free space focusing by means of Split Ring Resonator structure. We take the next step and demonstrate that fishnet inhomogeneous metamaterial structures can be used for the thin-film lenses in the NIR regime. Here we report the first numerical demonstration of a flat, thin-film (< 250 nm) GRIN positive lens operating in the NIR (~ 1.55 μm) and based on the fishnet structure. This represents a significant advance toward applications as well as steps forward in design complexity and construction technique.

Complex RCWA based, parametric studies and the optimization for the largest achievable phase shift with smallest variation in transmission have been performed. Proposed $(64 \times 64)\lambda^2$ area experimental samples will have small edge effects and act as $f/26$ lens. The F number can be significantly improved by stacking several layers of NIMs. Preliminary experimental results show a successful pattern transferring in the photoresist layer by the use of Imaging Interferometric Lithography (IIL) tool.

TABLE OF CONTENT

CHAPTER 1 INTRODUCTION.....	1
1.1 Negative index of refraction.....	1
1.2 First experimental realizations of NIMs.....	5
1.3 Scaling of the negative index metamaterials to the optical frequencies	10
1.4 Exploration of new properties and potential applications for NIMs.....	15
1.4.1 NIM slab lens.....	15
1.4.2 Hyper lens and super lens	20
1.4.3 Cloaking.....	23
1.4.4 Free space microwave focusing by a negative index gradient lens	25
1.4.5 Optical Switching Device with a Negative-Index Metamaterial.....	28
1.5 New applications and physics developed in the course of this thesis	31
1.6 References	38
CHAPTER 2 RESONANT COUPLING TO A DIPOLE ABSORBER INSIDE A METAMATERIAL: HYBRIDIZATION OF THE NEGATIVE INDEX RESPONSE	43
2.1 Introduction	43
2.2 Simple physical model	44
2.3. Numerical modeling.....	49
2.3.1 Extraction of the optical parameters of the metamaterial structure.....	49
2.3.2 Results of RCWA numerical simulation	54

2.4. Experimental demonstration	58
2.4.1 Design of experiment (DOE).....	58
2.4.2 Fabrication of the experimental samples	65
2.4.3 Experimental results	67
2.5 Conclusions	74
2.6 References	76

CHAPTER 3 IMAGING INTERFEROMETRIC LITHOGRAPHY:

DEMONSTRATION OF $\sim \lambda/(3NA)$ HALF-PITCH FEATURES BY 244-NM, 0.9 NA OPTICAL TEST BED.....	77
3.1 Introduction	77
3.2 Nanofabrication techniques.....	80
3.2.1 Interferometric Lithography (IL).....	80
3.2.2 IIL - Imaging interferometric lithography	86
3.2.2.1 Introduction, theory and previous work.....	86
3.2.2.2 Pupil Plane Filters (PPF).....	95
3.2.2.3 PROLITH modeling.....	97
3.3 Experimental setup.....	104
3.4 Experimental Protocol.....	110
3.4.1 Sample preparation	110
3.4.2 Photoresist/ARC Stack	110
3.4.3 Exposures.....	114

3.5 Fabrication of periodical and arbitrary structures	115
3.5.1 Fabrication of the periodic grating in the PR	115
3.5.2 Fabrication of the arbitrary Manhattan structure in the PR	118
3.5 Conclusions	128
3.6 References	130

**CHAPTER 4 GRADIENT INDEX OPTICAL LENS (~1.55 μm) USING
INHOMOGENEOUS METAMATERIALS 132**

4.1 Introduction	132
4.2 Design of proposed structure.....	134
4.3 Parametric study and numerical modeling.....	139
4.3.1 RCWA numerical simulation	139
4.3.2 Parametric study and simulation results	140
4.3.2.1 Evaluation of different dielectrics for fixed layers thicknesses	142
4.3.2.2 Evaluation of different dielectric layer thickness for individual dielectric	146
4.3.2.3 Evaluation of different total combined thickness of 3 layers for individual dielectric.....	152
4.3.2.4 Evaluation of different metal layer thickness for individual dielectric....	159
4.3.2.5 Evaluation of effect of decreasing the dielectric layer thickness for individual dielectric	163
4.3.2.6 Summary and the results of the numeric parametric study	167
4.4 Design of experiment	170

4.5 Conclusions	176
4.6 References	178
CHAPTER 5 FUTURE WORK	176
5.1 Potential application for the hybridization of magnetic and dipole resonances....	176
5.2 Experimental demonstration of the GRIN optical lens	177
5.3 Imaging Interferometric Lithography.....	179
APPENDIX A	180

Chapter 1 Introduction

1.1 Negative index of refraction

Metamaterials, first discovered by Veselago in 1968 [1] are a new class of nanostructured materials that offer novel optical properties, such as a negative index of refraction. He considered a special case of negative refractive index and laid the fundamental work for the theory of negative refraction. We will now briefly discuss key developments of his theoretical work.

For an isotropic medium, the refractive index is given by:

$$n = \sqrt{\epsilon \mu} \quad (1.1)$$

The complex permittivity (ϵ) and permeability (μ) can be written as $\epsilon = \epsilon_1 + i\epsilon_2$ and $\mu = \mu_1 + i\mu_2$. If both the permittivity (ϵ) and permeability (μ) are real and negative, the three vectors \mathbf{E} , \mathbf{H} and \mathbf{k} form a left-hand relation, which is opposite to the case when they are positive. Thus, this special type of unconventional material is called a left handed material. Equation (1.1) can be rewritten as:

$$n^2 = (\epsilon_1 + i\epsilon_2)(\mu_1 + i\mu_2) \quad (1.2)$$

By equating the real and imaginary parts on both sides of equation (1.2), we get:

$$n_1^2 = \epsilon_1 \mu_1 - \epsilon_2 \mu_2 \quad (1.3)$$

$$2n_1n_2 \quad (1.4)$$

Causality requires that the imaginary part of refractive index be positive, so that the sign of real part of index n_1 is solely determined by $(\mu_1\epsilon_2+\mu_2\epsilon_1)$. At optical frequencies, the magnetic response in all natural materials is considered to be negligible, i.e. $\mu_1 \sim 1$ and $\mu_2 \sim 0$. Thus, n_1 has the same sign as ϵ_2 , which is also positive due to the causality requirements. However, if we consider some materials that do have $\mu_1 < 0$ and $\epsilon_1 < 0$, then the real part of refractive index n_1 would be negative because the condition $(\mu_1\epsilon_2+\mu_2\epsilon_1) < 0$ is met. This type of material is called negative index metamaterial (NIM).

Next, The Poynting vector S is given by:

$$S = \frac{c}{4\pi} \vec{E} \times \vec{H} \quad (1.5)$$

Suppose a plane wave that propagates in negative index metamaterial has following time - space dependence: $\exp(-i\omega t + ikz)$, and has the electric field along x direction and the magnetic field along y direction. Then, the propagation vector is given by $\mathbf{k} = (n\omega/c)\mathbf{e}_z$, where a complex $n = n_1 + in_2$ has a negative real part (n_1) related through the Kramers-Kronig dispersion relationship to the positive imaginary part (n_2). In the following derivation, we drop the exponential dependence of time and space and can rewrite electrical field as $\mathbf{E} = E_0 \mathbf{e}_x$, where \mathbf{e}_x is a unit vector along x direction. The magnetic field can be expressed as:

$$\vec{H} = \frac{c}{4\pi} \vec{k} \times \vec{E} = \frac{c}{4\pi} \frac{n}{c} E_0 (\mathbf{e}_z \times \mathbf{e}_x) = \frac{E_0}{4\pi} \mathbf{e}_y \quad (1.6)$$

Combining Eqn. (1.5) and Eqn. (1.6) leads to:

$$\vec{S} = \frac{c}{4\pi} e_z \quad (1.7)$$

Where ζ is the impedance given by:

$$\zeta = \sqrt{\frac{\mu}{\epsilon}} \quad (1.8)$$

The impedance relative to this media determines the reflectance at the boundary between two different mediums. Causality requires the real parts of ζ to be positive.

As it is mentioned above, the real part of ζ is always positive, thus, the direction of the wave vector \vec{k} and the Poynting vector \vec{S} are opposite if the real part of the index is negative. Veselago, in his theoretical work reached the same conclusion by assuming lossless NIM and, since negative effective permeability at the resonance will have losses, we generalized our conclusion by allowing the optical parameters to be complex.

One very important conclusion that comes directly from the negative refractive index is the negative refraction. Refraction is one of the most fundamental phenomena in optics. When light is incident from one media onto another media of different refractive index at a certain angle other than normal, the light will be bent away from its original course as shown in Figure 1.1.

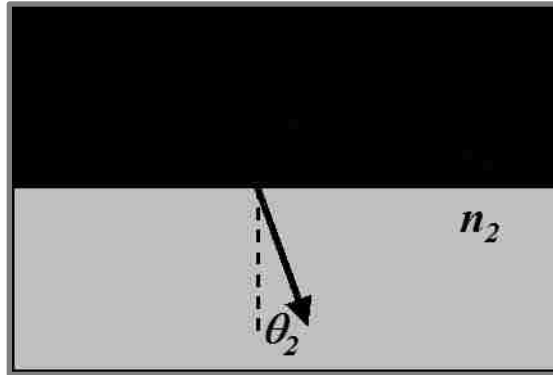


Fig. 1.1 Schematic illustration representing refraction of light at the boundary of two media with different refractive indexes.

This effect is well described in mathematics by the famous Snell's law, which relates the incident angle and the refraction angle with the refractive indexes of the two media.

$$n_1 \sin(\theta_1) = n_2 \sin(\theta_2) \quad (1.9)$$

For both incident and outgoing media with positive refractive index, the refracted beam is always on the opposite side of the surface normal, away from the incident beam, so that the momentum along the interface is conserved.

But in the case of negative refraction, because the real part of the index is negative, the refraction angle is negative according to Eqn. (1.9). Thus, as shown in Figure 1.2, both the incident beam and the refracted beam are on the same side of the surface normal.

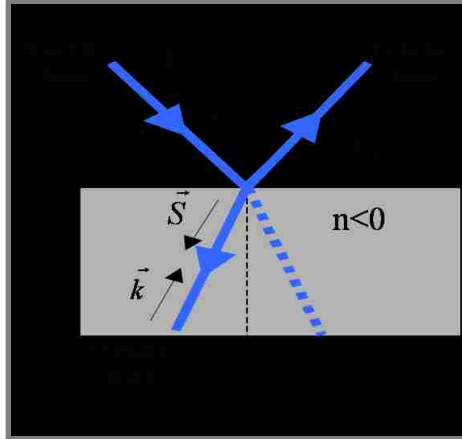


Fig. 1.2 Schematic illustration of negative refraction when beam is incident from the media with $n > 0$ to NIM media $n < 0$; the reflected beam and the incident beam are on the same side from normal. Dashed line represents ordinary case where lower media has $n > 0$.

Furthermore, the opposite directions of the energy flow and the phase velocity in NIM result in many interesting phenomena, such as reverse Doppler effect and reverse Cerenkov radiation. The reversed Doppler effect states that when a light source is moving towards a receiver, the frequency of the light emitted by the source red shifts when it reaches the receiver and vice versa, which is contrary to the Doppler effect in a normal medium.

1.2 First experimental realizations of NIMs

Since there are no naturally occurring materials with negative permeability, it seemed impossible to artificially create materials with negative index of refraction until in 1999, Pendry *et al.* [2] proposed metallic dielectric composite structure, now known as a famous split ring resonator (SRR), to achieve negative magnetic response. In his work, he considered a double SRR structure, as it is shown in the Figure 1.3. Later (see section 1.3), it was demonstrated that a single SRR can also exhibit a negative magnetic response.

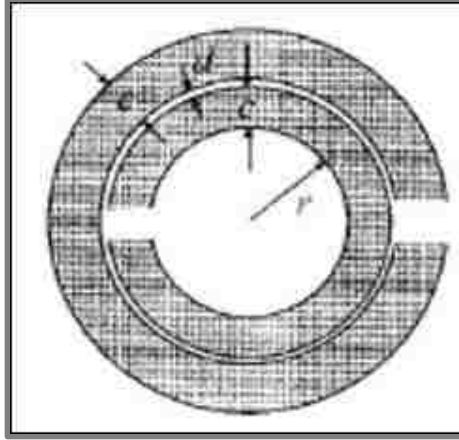


Fig. 1.3 Graphical representation of a double split ring resonator (SRR) structure that leads to a negative magnetic response, proposed by Pendry in 1999.

The double SRR consists of two concentric metallic rings, each one with an opening in the opposite directions. This structure is equivalent to an R-L-C circuit, the inductance is associated with the two loops, and the capacitance is formed between the two concentric metal rings and the dielectric gap in between, and the resistance is due to the Ohmic loss of the metal. When a beam of light is incident on the SRR with magnetic field perpendicular to the structure, a current is induced in the two rings. At the vicinity of the resonant frequency, which is given as $\omega_{resonant} = (LC)^{-1/2}$, the magnetic response is strongest. Depending on which side of the resonance frequency the incoming light is, the magnetic field generated by the induced current can be either in the same direction or in opposite direction of the external magnetic field H , causing the effective permeability to be either greater or less than unity. For the designed structure, over a certain frequency range, the induced magnetic field could be stronger than the external magnetic field and in the opposite direction, leading to a negative permeability. A typical dispersion curve of an effective medium consisting of SRRs is shown in Figure 1.4 [2]. A strong modulation of the real part of the permeability exists around the resonance, accompanied with a sharp

absorption peak for the imaginary part, which is a standard characteristic of a Lorentz resonance curve.

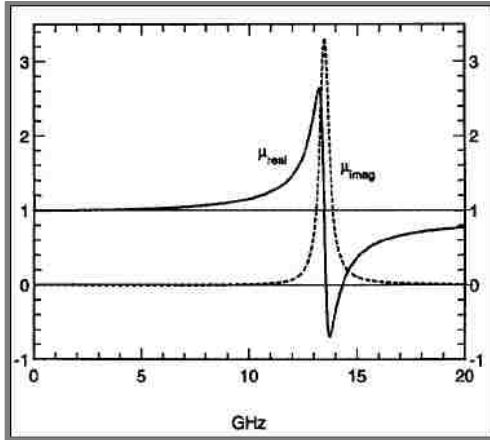


Fig. 1.4. Typical plot showing the magnetic response of real and imaginary part of the effective permeability (μ) of the SRR structure.

In 2000, Smith *et al.* [3,4], followed by the results demonstrated in other research groups [5], reported the first experimental demonstration of artificial NIM operating in the microwave region. He showed that an organized array of SRR structures combined with array of metal wires can create media that exhibit a negative index of refraction. Each unit cell of this structure was made to be much smaller than the incident wavelength and their combinations were treated as the effective media. Figure 1.5 shows this structure.

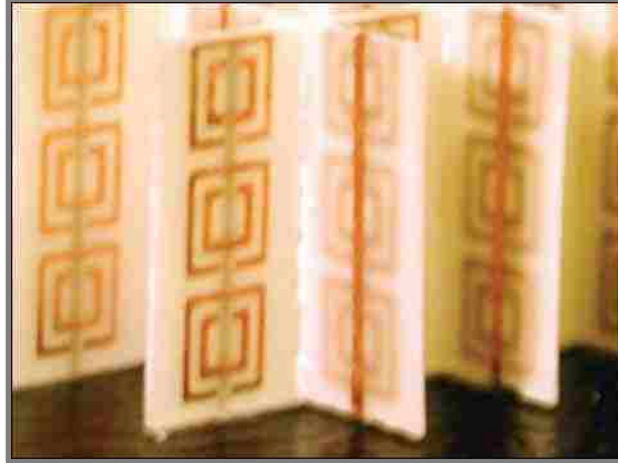


Fig. 1.5 First experimental NIM structure designed for microwave wavelengths that consist of double SRR and array of metal wires.

All naturally occurring metals will show negative permittivity response if the frequency of the incident light is below plasma frequency of the metal. But natural metals have plasma frequencies in the ultraviolet or visible range, which are many orders of magnitude higher than microwave frequencies. Thus, metals are very close to perfect ($\epsilon \rightarrow -\infty$) in microwave frequency band. So in order to construct negative permittivity $\epsilon(\omega)$ in the microwave region, it is desirable to decrease the plasma frequency of the metal. Pendry *et al.* has theoretically demonstrated very low plasma frequency in an array of thin metallic wires [6].

In the Drüde model, the plasma frequency for a bulk metal can be expressed as:

$$\omega_p = \sqrt{\frac{ne^2}{m_{eff}}} \quad (1.10)$$

Where n is the density of electrons, m_{eff} is the effective mass. In the case of a 2D array of thin metallic wires, the effective density of electrons would be reduced to:

$$n_{eff} = n \left(1 - \frac{r^2}{a^2} \right) \quad (1.11)$$

Where the geometrical parameters are shown in Figure 1.6:

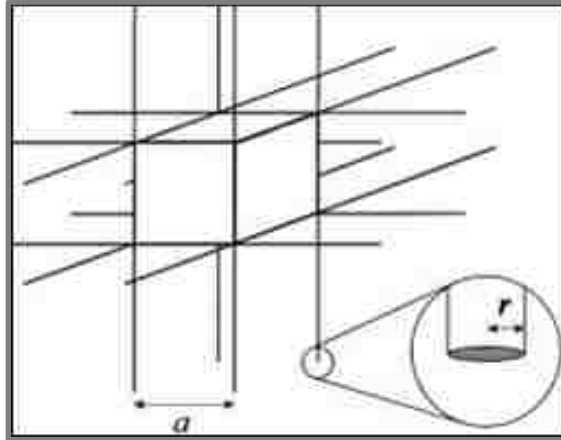


Fig. 1.6 Array of metallic wires used to demonstrate the decrease of the plasma frequency in the effective media. Geometrical parameters are indicated in the figure.

Furthermore, the effect of the self-inductance of the structure can be considered as a contribution to the effective mass of the electrons, which is given as:

$$m_{eff} = m \left(1 + \frac{r^2 e^2 n}{2} \ln(a/r) \right) \quad (1.12)$$

Thus, both the increase of effective mass of electrons and decrease of the electron density help to reduce the plasma frequency of the structure. These facts can be utilized to obtain mildly negative permittivity in the microwave region [7].

1.3 Scaling of the negative index metamaterials to the optical frequencies

Since first realization of metamaterials, many research groups put their efforts in scaling magnetic resonant structures to the higher frequencies with the ultimate goal of obtaining negative refraction at optical frequencies. Yen *et al.* [8] have demonstrated the first magnetic resonant structure in the THz range, as shown in Figure. 1.7

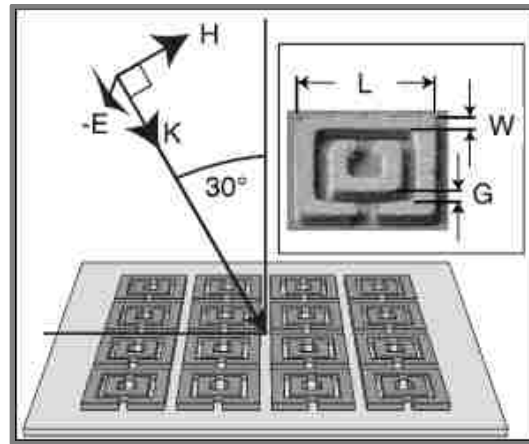


Fig. 1.7 Schematic illustration of the planar SRR array that demonstrates magnetic negative response in the THz regime. Insert shows SEM picture of the SRR with the geometrical parameters: $L = 26 \mu\text{m}$, $W = 4 \mu\text{m}$, $G = 2 \mu\text{m}$.

This structure is a scaled version of a square double SRR lying flat on a quartz substrate with a smallest dimension of $2 \mu\text{m}$, the gap between the inner and outer rings. This structure was fabricated by contact lithography, which is suitable for features bigger than $1 \mu\text{m}$. The resonant frequency of the structures is around 1THz which corresponds to a wavelength around $300 \mu\text{m}$. To extend the resonance of this structure to the optical frequency of 100 THz, the smallest feature would need to be scaled down to 20 nm.

Soon after, two groups have independently demonstrated magnetic resonators in the mid-infrared with very different approaches and fabrication methods [9,10]. Linden *et al.* [9] used a scaled single split ring resonator, as shown in Figure 1.8.

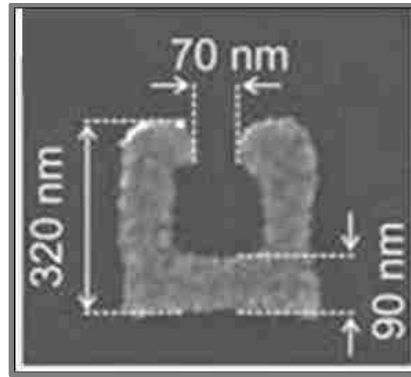


Fig. 1.8 SEM image of the single SRR used by Linden *et al.* in demonstration of the magnetic resonant structure at 100 THz.

The structure is equivalent to an L-C circuit, with the loop as the inductor and the gap as a capacitor. The structure was fabricated using e-beam lithography with the smallest feature around 70 nm (the gap). The L-C resonance can be excited either by a time varying electric field across the capacitor, or a time varying magnetic field perpendicular to the inductor loop. In this work, the resonance of the L-C circuits was excited for the polarization parallel to the gap. Both the transmission and reflectance have a good fit by the simulation, and simulation was used to extract the permeability, which was found to be negative at around 100 THz or a wavelength of 3 μm .

In 2005, Zhang *et al.*[10], demonstrated an array of vertical staple structures, that was fabricated using interferometric lithography (IL) combined with self-aligned semiconductor processing techniques, as shown in the Figure 1.9. The resonant frequency of the staple structure was found to be around 65 THz ($\sim 5 \mu\text{m}$).

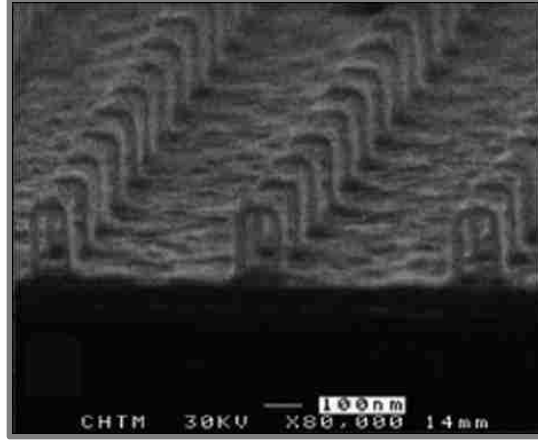


Fig. 1.9 SEM image of the gold staples fabricated by Zhang using IL and self-aligned semiconductor processing. Negative magnetic resonance was found to be at $\sim 5 \mu\text{m}$ wavelength or $\sim 65 \text{ THz}$.

However, neither Linden nor Zhang were able to achieve a double negative index of refraction, which requires having simultaneous combination of negative permeability and permittivity. Simple scaling of the SRR structure with the array of thin metallic wires was extremely difficult due to fabrication complications and changes in the physical response of the structure. At low frequency regimes, the magnetic resonance frequency of SRR scales reciprocally with the structural size. At high frequencies, however, this linear scaling breaks down [11]. In some narrow frequency band, the key components SRR and wire simultaneously provide a negative effective permeability μ_{eff} (due to a resonance of circular currents around the SRR) and a negative effective permittivity ϵ_{eff} with plasma frequency ω'_p greatly reduced compared to that of bulk metal ω_p , as a result, mainly, of the magnetic field energy dominating the kinetic energy of the current carrying electrons. At high frequencies, the kinetic energy of the electrons in the metal (in both the SRRs and the wires) cannot be neglected anymore in comparison with the magnetic energy. As the magnetic resonance frequency is pushed higher by reducing the structural size of the SRR, a breakdown of the linear scaling, which, together with a diminishing strength of

the SRR resonance due to the increase of the losses, ultimately renders the SRR dysfunctional.

Solutions to the problem of pushing the performance of a metamaterial structure in the near-infrared (NIR) region was demonstrated, independently by Zhang *et al* [12] and Shalaev *et al* [13] in 2005.

Shalaev demonstrated an array of pairs of parallel gold nanorods as shown in the Figure 1.10. This structure has a negative refractive index at the optical communication wavelength of $\sim 1.5 \mu\text{m}$.

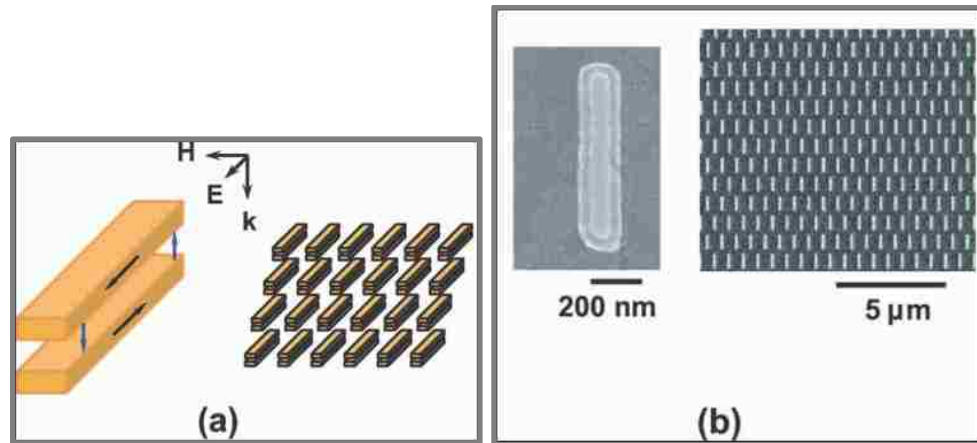


Fig. 1.10 a) Schematic illustration of the array of the nanorod pairs used by Shalaev, b) FEM image of the nanorod structure exhibiting negative index of refraction at $\sim 1.5 \mu\text{m}$.

Negative index behavior results from the plasmon resonance in the pairs of nanorods for both the electric and the magnetic components of light. However, this structure requires very precise overlapping of the negative resonances in the magnetic and electric components in order to achieve double negative refractive index. Further investigation showed that it is a non-trivial task to achieve this overlap, especially when pushing the regime of operation in the shorter wavelengths.

Zhang *et al.*[12] come up with a different structure that is now well known as a “fishnet” metamaterial as it shown in the Figure 1.11.

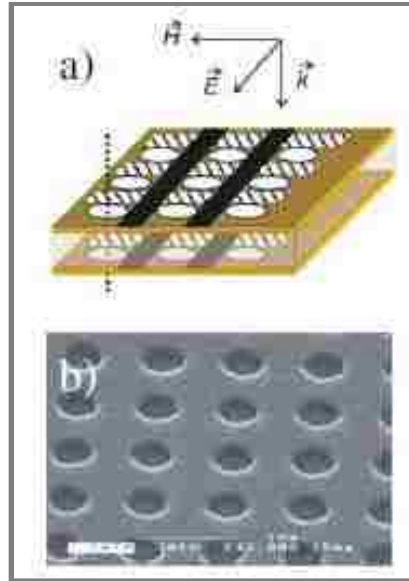


Fig. 1.11(a) schematic of the multilayer structure consisting of an Al_2O_3 dielectric layer between two Au films perforated with a square array of holes (838 nm pitch; 360 nm diameter) atop a glass substrate. For the specific polarization and propagation direction shown, the active regions for the electric (dark regions) and magnetic (hatched regions) responses are indicated. (b) SEM picture of the fabricated structure.

The negative index of refraction in this structure comes from two parts: (1) a negative electric permittivity (ϵ) that results from an array of thin metal wires parallel to the direction of electric field; and (2) a negative magnetic permeability (μ) resulting from a pair of finite-width metal strips separated by a dielectric layer along the direction of the incident magnetic field. If the frequency of the incident light is below the plasma frequency of the metal, then a broadband negative permittivity can be realized. A width and a period of the lines that are usually on the order of $\sim \lambda/2n$ of a wavelength of the incident light provide negative permeability in this structure. Combination of the broadband negative ϵ and tunable negative μ makes a fishnet metamaterial structure more flexible and a promising base for future improvements than pairs of parallel nanorods.

Indeed, a report has shown a negative index response from the fishnet structure in the visible wavelength region at ~ 780 nm in 2007 [14]. And the newest demonstration by

S. Xiao *et al.* [15] has pushed the performance of the fishnet metamaterial structure in the yellow light region at ~ 580 nm.

To date, much effort has been devoted to the fabrication of these materials, the characterization of their linear optical properties, and the extension of their operation wavelengths. Since then, understanding of negative index metamaterials (NIMs) has advanced rapidly. Current theoretical and experimental work is directed towards exploring new properties and potential applications for NIMs.

1.4 Exploration of new properties and potential applications for NIMs

1.4.1 NIM slab lens

Veselago [1] was the first to discuss the possibility of using a slab of negative index material as an imaging lens. A schematic of the proposed imaging system is shown in the Figure 1.12.

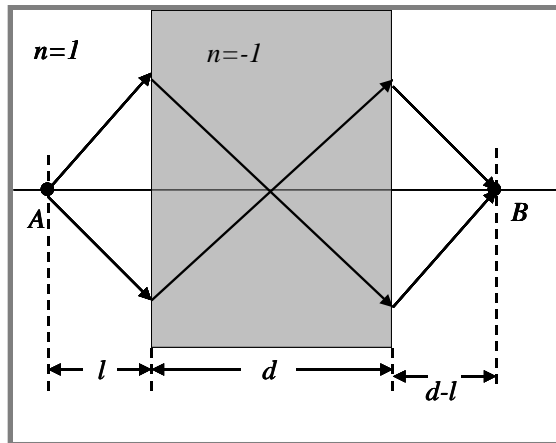


Fig. 1.12 Schematic illustration of the imaging system using a slab of NIM

For a light source at position A with a distance of l smaller than the thickness d of the negative index slab, there are two images, one inside the negative index slab, the other out of the slab at a distance $d - l$ away from the edge (point B).

In 2000, Pendry *et al.* [16] first theoretically demonstrated that a slab of lossless NIM could recover the evanescent field as well as the propagating fields and hence act as a “perfect lens”. It is known that there is a limit to the resolution of a conventional lens because only propagating waves can be used to construct the image, leading to a diffraction limit with a minimum feature of \sim half of the wavelength. By using a lossless NIM slab, both the propagating and evanescent components could be combined to construct the image, which could overcome the diffraction limit.

However, the possibility of creating a perfect lens has been widely debated among the research community [17,18]. The main concern is that even very small absorption can damage the ability of a NIM slab to amplify the evanescent wave. This can be illustrated by performing a set of calculation for the system shown in Figure 1.13, a slab of NIM surrounded by lossless positive index media.

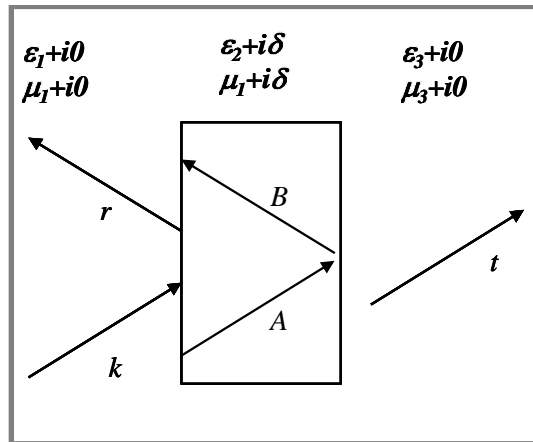


Fig. 1.13 Schematic illustration for the slab geometry calculations. Slab is a double negative metamaterial. Both cladding regions have lossless permittivity and permeability

A small loss term is added to both the permittivity and permeability of the NIM slab. Solving for the boundary condition at the two interfaces gives:

$$1 + \frac{A}{\beta} = t \left[A e^{-\gamma L} + \beta e^{-\gamma L} \right] \quad (1.13)$$

Where:

- $\gamma = \sqrt{k_x^2 - k_0^2}$ is the decay constant;
- $\text{Re}(\gamma_i) > 0$ and $A = (k_x/k_0)$ is the transverse wave vector (real) normalized to the free space wave vector. The square root is always taken with a positive real part.

Solving the boundary conditions for the coefficient r, A, B and t gives:

$$1 - \frac{A}{\beta} = t \left[A e^{-\gamma L} - \beta e^{-\gamma L} \right] \quad (1.14)$$

$$t = \frac{2}{1 - \frac{A}{\beta}} \quad (1.15)$$

$$r = \frac{(1 - \frac{A}{\beta})(1 - \frac{A}{\beta})e^{-\gamma L} - (1 + \frac{A}{\beta})(1 + \frac{A}{\beta})e^{-\gamma L}}{2} \quad (1.16)$$

$$A = \frac{2(1 - \frac{A}{\beta})e^{-\gamma L}}{1 - \frac{A}{\beta}} \quad (1.17)$$

$$B = \frac{2(1 - \Gamma_{12})e^{-\gamma L}}{1 - \Gamma_{12}e^{-2\gamma L}} \quad (1.18)$$

Thus, the electric and magnetic field inside the NIM slab are:

$$H_y = A e^{-\gamma z} + B e^{\gamma z} \quad (1.19)$$

$$E_x = \frac{1}{\epsilon_2} (A e^{-\gamma z} - B e^{\gamma z}) \quad (1.20)$$

Next we are going to consider the case when $\epsilon_1 = \epsilon_3 = 1$ and $\mu_1 = \mu_3 = 1$, and the $\epsilon_2 = (-1 + \delta_1)$, $\mu_2 = (-1 + \delta_2)$. We are looking at the expression for the denominator ψ . In the lossless limit, where $\Gamma_{12}, \Gamma_{23} \rightarrow -1$, the second term dominates. This gives the limit for the perfect imaging, $r \rightarrow 0$, $A \rightarrow 0$, $B \rightarrow 1$ and $t \rightarrow \exp(\gamma_2 L)$. When the losses are increasing, then the first term will increase very fast because of the amplifying effect from the exponential term. When the first term becomes comparable to the second term, both A and B are around 0.5, and the transmission drops to approximately half of that of perfect imaging. This occurs at:

$$\left| (1 - \Gamma_{12})(1 - \Gamma_{23})e^{-\gamma L} \right| = \left| (1 + \Gamma_{12})(1 + \Gamma_{23})e^{\gamma L} \right| \quad (1.21)$$

Assuming that δ_1 and δ_2 are much smaller than 1 and $(\Lambda^2 - 1)$, then Γ_{12} can be approximated by:

$$\frac{\sqrt{\frac{1}{2} \left(\frac{1}{\Lambda} + \frac{1}{\Delta} \right)}}{\left(\frac{1}{\Lambda} + \frac{1}{\Delta} \right) \sqrt{\frac{1}{2} \left(\frac{1}{\Lambda} + \frac{1}{\Delta} \right)}} \frac{1}{2} \frac{\sqrt{\frac{1}{2} \left(\frac{1}{\Lambda} + \frac{1}{\Delta} \right)}}{\sqrt{\frac{1}{2} \left(\frac{1}{\Lambda} + \frac{1}{\Delta} \right)}} \quad (1.22)$$

And

$$\frac{1}{\sqrt{\frac{1}{2} \left(\frac{1}{\Lambda} + \frac{1}{\Delta} \right)}} \quad (1.23)$$

Substitute Eq. (1.22) and Eq. (1.23) into Eq. (1.21), finally we have:

$$\ln\left(\frac{1}{2}\right) \frac{1}{\sqrt{\frac{1}{2} \left(\frac{1}{\Lambda} + \frac{1}{\Delta} \right)}} k_0 \sqrt{\frac{1}{2} \left(\frac{1}{\Lambda} + \frac{1}{\Delta} \right)} \quad (1.24)$$

In the case when $\Lambda \gg 1$ and $\Delta \sim \delta_1$, Eq. (1.24) can be approximated as:

$$\frac{1}{\sqrt{\frac{1}{2} \left(\frac{1}{\Lambda} + \frac{1}{\Delta} \right)}} \ln\left(\frac{1}{2}\right) / \left(2 \sqrt{\frac{1}{2} \left(\frac{1}{\Lambda} + \frac{1}{\Delta} \right)} \right) \quad (1.25)$$

A similar result was obtained by Smith *et al.* [19]. An important point that needs to be taken from this derivation is that the dependence of the resolution enhancement Λ on the deviation from the perfect lens condition is very critical and is very strongly dependent on the thickness of the material and the loss of NIM. For example: in order to achieve a resolution enhancement Λ of 10 for $L = 0.1\lambda$, we should have losses in the range of $\delta = 2 \times 10^{-3}$. That means that we have to have a very thin-film slab with a very low loss, however, in the practical world we have δ on the order of 0.1. All that, put together, makes the use of this slab lens for the purposes of the perfect lens impractical.

The application of NIM as a super lens would be highly limited due to the very high dependence on the loss and thickness of the NIM slab. This super lens being created

will work only within very short distance between the object and the image and would not have any potential for the far-field applications.

However, there are still a lot of attempts among the research community to experimentally demonstrate focusing by the NIMs beyond the diffraction limit [20,21, 22]. Those efforts lead to creation of “hyper lens” developed and demonstrated by the X. Zhang research group [23].

1.4.2 Hyper lens and super lens

The members of the X. Zhang research group Hyesog Lee *et al.* in 2007 [24] considered the following problem: that since high spatial frequency information carried by evanescent waves only exists in the near field of an object, only the propagating light reaches the far-field image plane and the resolution of the conventional microscope is limited to half of the wavelength. They proposed the idea of the hyperlens that will break the diffraction limit by magnifying the sub-diffraction-limited objects and projecting the magnified images to the far field. The hyperlens, as it shown in the Figure 1.14, is composed of a curved periodic stack of Ag (35 nm) and Al₂O₃ (35 nm) deposited on a half-cylindrical cavity fabricated on a quartz substrate.

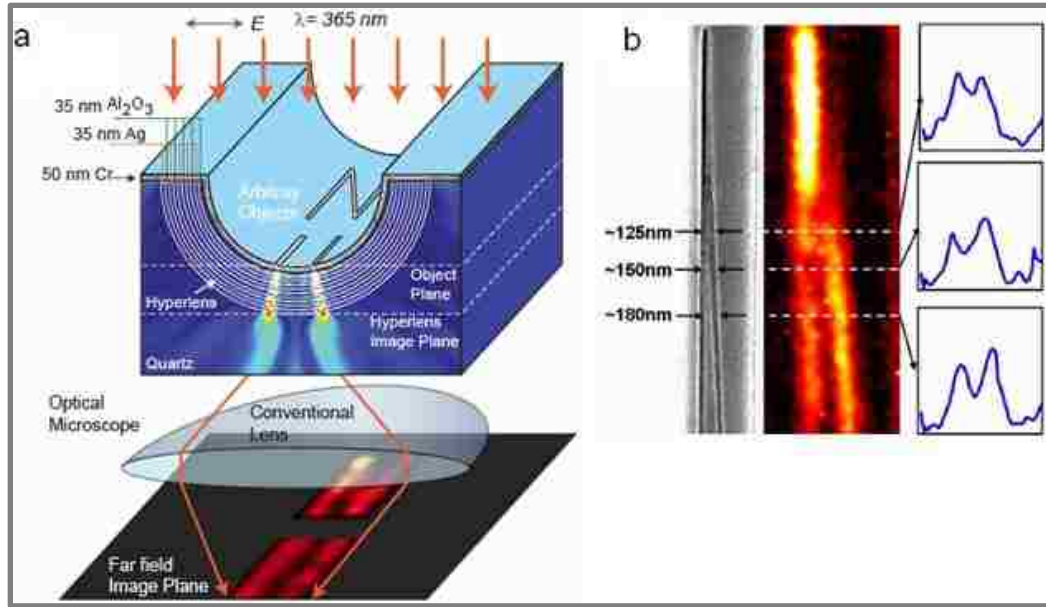


Fig. 1.14 Magnifying optical hyperlens. (a) Schematic of hyperlens and numerical simulation of imaging of sub-diffraction-limited objects. (b) Left: SEM image of tilted line pair object with indicated gap sizes. Middle: image captured by optical microscope through hyperlensing. Right: intensity profiles of the three indicated cross sections showing resolved 125nm gap (top).

This anisotropic metamaterial has electric permittivities in opposite signs in two orthogonal directions, which not only enables waves with large tangential wave vectors to propagate in the medium but also achieves an image magnification. Experimental results demonstrating far-field imaging with resolution down to 125nm at 365nm working wavelength were shown by Zhaowei Liu *et al.*[25] also in 2007.

Another idea of perfect imaging was developed from the near field superlens approach [26]. Basic idea is very similar to the one described above. A far-field imaging system cannot retrieve evanescent waves which contain sub-wavelength details of an object but decays within the near field. Utilizing the physics of surface plasmons, a thin silver slab, a superlens, is able to amplify and restore the evanescent field and image with sub-diffraction-limited resolution. Figure 1.15 shows a schematic illustration of the near-field thin silver slab superlens.

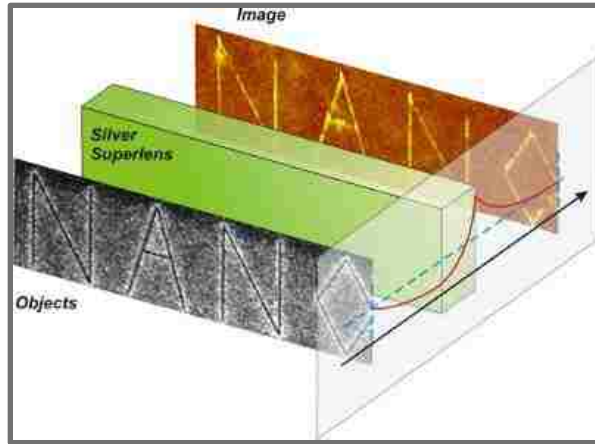


Fig. 1.15 Schematic illustration of the near field silver slab superlens developed by X. Zhang research group.

Later, this concept was extended in the far field regime [27, 28]. The far-field superlens (FSL) can reconstruct the sub-diffraction-limited images from the far-field measurement. A FSL is made of a silver slab and a one-dimensional sub-wavelength silver grating, as it shown in the Figure 1.16.

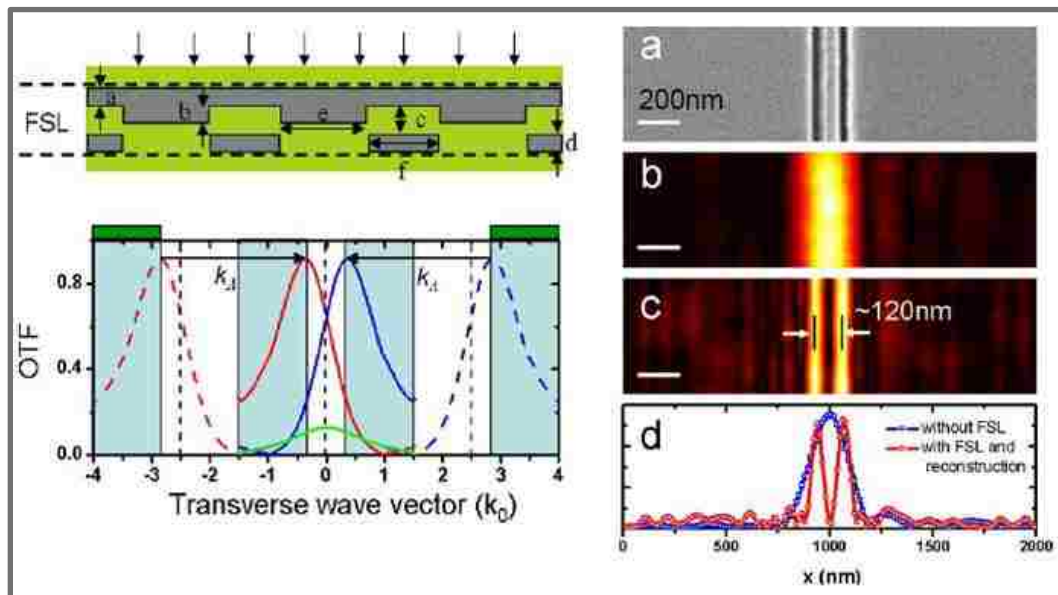


Fig. 1.16 Left: Top: schematic of the silver FSL. Bottom: calculated otf of the optimized FSL under p-polarized incident light with vacuum wavelength of 377 nm. Right: far-field imaging of a pair of nanowires. (a) SEM image of an object nanowire pair with 50 nm wide slit and 70 nm gap; (b) diffraction-limited image from a conventional optical microscope; (c) FSL image that resolves the sub-diffraction objects due to strong evanescent enhancement via surface plasmon excitation at FSL; (d) the averaged cross-section image profiles from (b) and (c).

The silver slab of the FSL enhances the evanescent waves and the sub-wavelength grating of the FSL converts the enhanced evanescent waves into the propagating waves. Subsequently, the high spatial frequency information can be collected in the far field, and the sub-diffraction-limited images can be reconstructed. Experimental demonstration of the one-dimensional sub-diffraction-limited imaging by the FSL was reported in 2007 [29]. It was shown that a FSL could image a sub-wavelength object consisting of two 50nm wide lines separated by 70nm working at 377nm wavelength.

This demonstrates an alternative version of the far field imaging resolution, but it is still not quite at the stage of practical implementation.

1.4.3 Cloaking

In 2006, D. Schurig *et al.* [30] suggested that a cloak of invisibility is, in principle, possible, at least over a narrow frequency band. He based this idea on the new approach to the design of electromagnetic structures that was proposed by Pendry *et al.*[31] and U. Leonhardt *et al.* [32] in 2006. In this approach, the paths of electromagnetic waves are controlled within a material by introducing a prescribed spatial variation in the constitutive parameters. By using these transformation optics, Schurig rendered a volume effectively invisible to incident radiation. The design process for the cloak involves a coordinate transformation that squeezes space from a volume into a shell surrounding the concealment volume. In the first practical realization of such a cloak, a copper cylinder was “hidden” inside a cloak constructed according to the previous theoretical prescription. Figure 1.17 shows the results of the numerical simulation as well as the experimental demonstration of the cloaking.

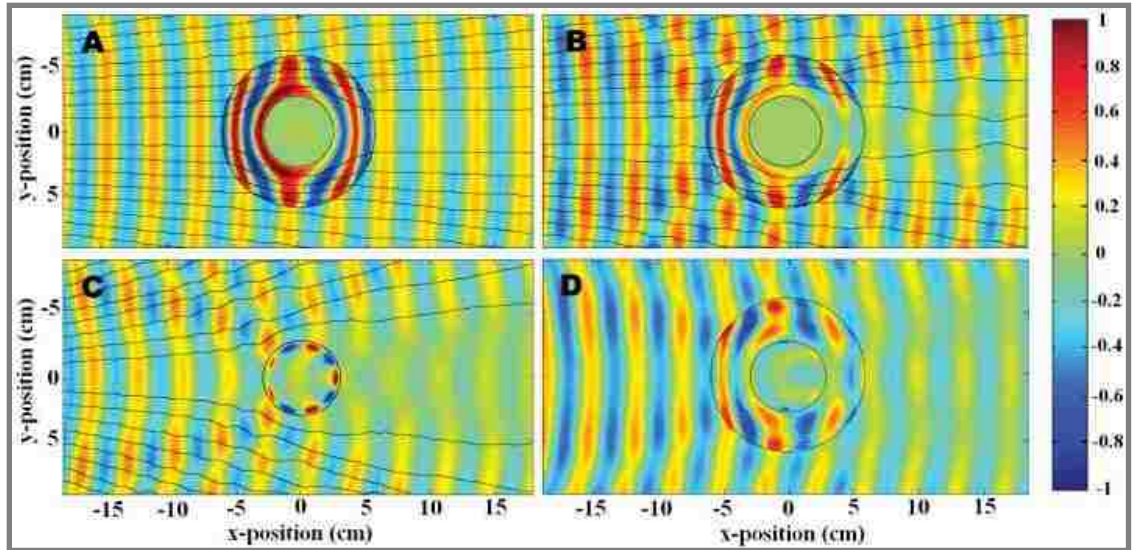


Fig. 1.17 Snapshots of time-dependent, steady-state electric field patterns, with stream lines [black lines in (a to c)] indicating the direction of power flow (i.e., the Poynting vector). The cloak lies in the annular region between the black circles and surrounds a conducting Cu cylinder at the inner radius. The fields shown are (a) the simulation of the cloak with the exact material properties, (b) the simulation of the cloak with the reduced material properties, (c) the experimental measurement of the bare conducting cylinder, and (d) the experimental measurement of the cloaked conducting cylinder.

The cloak was constructed with the use of artificially structured metamaterials, designed for operation over a band of microwave frequencies and based on the SRR structure as it shown in the Figure 1.18.



Fig. 1.18 Snapshot of the SRR based cloaking devise proposed by Schurig in 2006.

The cloak decreased scattering from the hidden object, while at the same time reducing its shadow, so that the cloak and object combined began to resemble empty space.

Though demonstrated invisibility was imperfect because of the approximations used and material absorption, this result did provide the first experimental display of the electromagnetic cloaking mechanism.

But, more importantly, this experiment demonstrates the feasibility of implementing media specified by the transformation optics method with metamaterial technology. This means that we can take a metamaterial structure and, by using transformation optics, design it such that it will ever inhibit necessary properties or will respond in the desired way. Use of this principal was demonstrated by T. Driscoll *et al.* who showed a free space microwave focusing by a negative-index gradient lens [33].

1.4.4 Free space microwave focusing by a negative index gradient lens

T. Driscoll presented a radial GRIN lens, built from elements similar to the SRRs and grid of metallic wire as shown in the Figure 1.19.

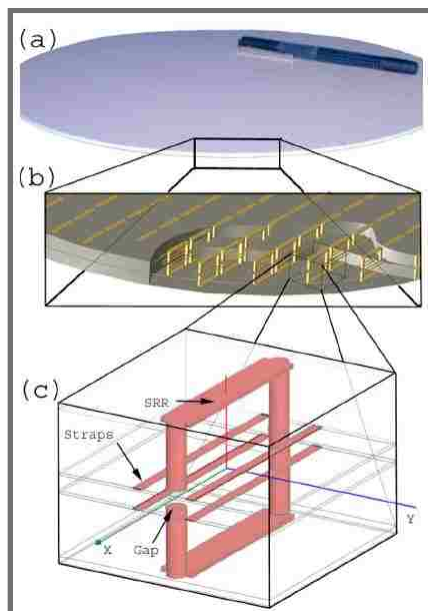


Fig. 1.19 Three tier diagram showing: a) actual picture of a lens disk; b) blow-up illustrating unit-cell array; c) further blown up single unit cell with SRR and wire elements. Magnetic field is applied in along y direction, electric field is along x .

This durable, lightweight, and modular lens operates as a positive gain spherical lens, focusing in two dimensions to achieve a focal spot amplitude +7 dB over incident.

A bi-planar geometrically “flat” lens with a radially varying gradient index of refraction ranging from -2.67 (edge) to -0.97 (center) was designed. In transferring this lens design to the metamaterial structure, the radial gradient is mapped onto a Cartesian array of unit cells with 50 steps over the radius. Each unit cell is a SRR and wire, shaped to have a specific magnetic and electric resonance. A 2 mm thick disk, 15 cm in radius, with this gradient is shown to behave as an $f/9$ lens at the microwave frequency of incident light ($\lambda_{\text{incident}} = \sim 29$ cm). In analyzing these data, one should take into consideration that at 10 GHz, this lens is only $\sim 10\lambda$ in diameter and, the diffractive edge effects may play an important role in its behavior. Figure 1.20 shows data for an eight-layer lens (in black) and a four-layer lens (in gray). Dashed lines are experimental data for the root-mean-square (RMS) field amplitude and solid curves are Microwave Studio simulation results for the same eight-layer and four-layer lenses, along the optical axis ($x = 0, y = 0, \text{ translate } z$) at 10.3 GHz, normalized to incident field amplitude.

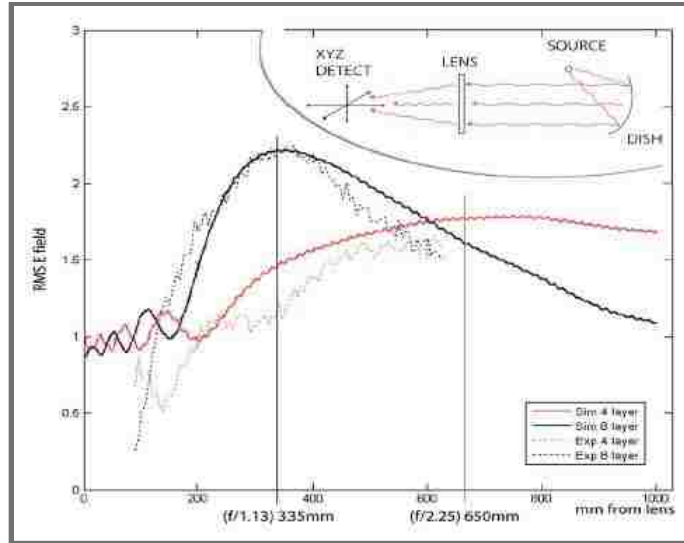


Fig. 1.20 RMS electric-field amplitude in both simulation (solid) and experiment (das) along the optical axis for GRIN lenses comprised of eight layers (black) and four layers (red).

This eight- layer and four-layer lenses have f -numbers of 1.13 and 2.25, respectively. The focal lengths predicted by these f -numbers are marked as vertical lines in Figure 1.20.

This experimental demonstration represents a significant step in design complexity and manufacturing advances. It shows one of the first practical applications for the metamaterial based structure operating in the microwave regime.

Up to this point we were talking about ever development in the potential applications for the metamaterials, that are in the early stage or demonstrates first experimental results but still not quite at the level of practical implementation, or we looked at the more practical results that were developed for the microwave wavelengths. However the infrared (IR) spectral region have shown to be of a particular interest because metal properties are in-between their very high conductive properties in the RF and the lossy plasmonic characteristics in the visible. As it was discussed earlier simple scaling of the RF structures to the IR regime is very difficult and requires adaptation of

the new metamaterials structure. In order to address this interest in the IR spectral region in the next section we will look at a worked performed by Z. Ku in the professor S. R. J. Brueck research group that demonstrates an practical example of use of metamaterials to create new and fast optical switch and then we will propose some new physical challenges and potential applications for the NIM structures.

1.4.5 Optical Switching Device with a Negative-Index Metamaterial

Practical background for development of all-optical signal processing is to eliminate the performance and cost penalties of optical-electrical-optical conversion, and is important for continuing advances in terabits/second (Tb/s) communications. Because of generally weak ($[X^{(2)}]^2$ or $X^{(3)}$) optical nonlinearities, all-optical Kerr-effect and three/four-wave mixing modulators require macroscopic propagation lengths, from centimeters in the case of periodically poled LiNbO₃ to kilometers for fiber-based approaches. Semiconductor optical amplifiers (SOA) offer larger nonlinearities, but these active devices add optical noise and require significant additional area for carrier injection and heat dissipation. High-Q crystalline semiconductor structures, modulated by optical carrier injection, are inherently slow as a result of long carrier lifetimes, although progress is being made in sweeping carriers out of the active region. Metamaterials can offer not only novel optical properties such as a negative index of refraction but also new capabilities for optical-optical interactions because they use much stronger structurally induced resonance over a short propagation length, on the order of hundreds of nm. Up to date, much effort has been devoted to the characterization of their linear optical properties. However, only limited results have been presented on the modulation of these properties in the terahertz [34, 35] (~20 ps response) and NIR [36] (~60 ps response)

spectral regions. In a recent report [37], soon followed by the results of R. Shen [38], K. Dani has demonstrated the first experimental result of subpicosecond optical switching with a negative index metamaterial. In his work the metamaterial includes a subwavelength LC resonance tank circuit with metal and semiconductor components to provide the negative permeability. An optical carrier injection was used to modify the conductivity of the semiconductor and dynamically affect the resonance behavior. A Tb/s modulator based on a tri-layer fishnet structured negative-index metamaterial (NIM) with ~ 600 fs device response and 20% modulation depth in the near-IR as the first generation device was reported. Figure 1.21 shows a schematic illustration of the proposed NIM structure.

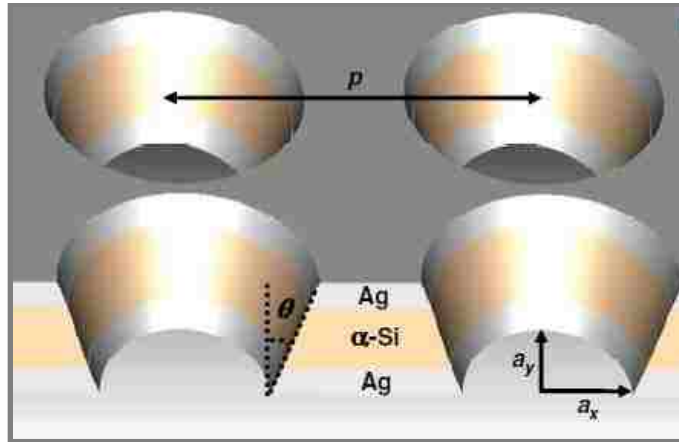


Fig.1.21 Schematic view of elliptical negative-index metamaterial (eNIM). Geometrical parameters of eNIM, $p = 345$ nm; $a_x = 81$ nm; $a_y = 119$ nm; and q (sidewall-angle) = 18° . The eNIM is composed of 28 nm thick silver (Ag); 68 nm thick amorphous silicon (a-Si); and 28 nm thick silver (Ag). The direction of polarization incoming light is parallel to the narrower stripe width between apertures (x -axis).

Ultrafast modulation of the eNIM optical properties was studied using a sub-100 fs, visible pump pulse to photoexcite carriers above the R-Si bandgap (~ 731 nm), and the timeresolved change in transmission was measured with a near-IR probe pulse. The pump-induced percentage change in transmission ($\Delta T/T$), that is, the switching ratio, is measured as a function of pump-probe delay (Δt), pump fluence, pump wavelength,

probe wavelength (1.0-1.5 μm), and probe polarization. Figure 1.22 shows the results of the experiment.

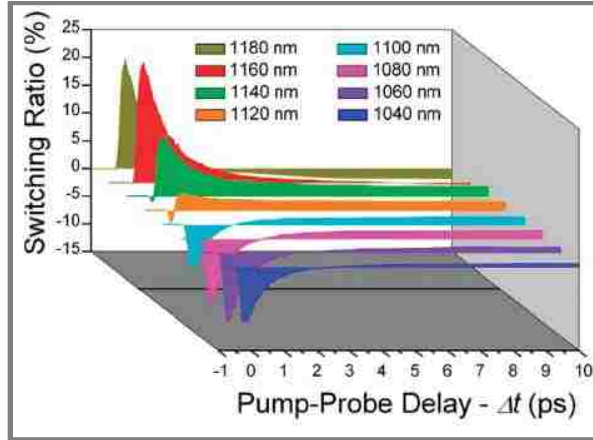


Fig. 1.22 eNIM pump-probe signal at different probe wavelengths (550 nm pump wavelength). Experimental data versus pump-probe delay.

An ultrafast dual-band all-optical switching device with a NIM at telecommunication wavelengths was demonstrated. This subpicosecond pump-probe response has the potential for all-optical Tb/s communication, while the nanometer-scale thickness results in a compact device easily integrated with other photonic devices and applications. Experimental demonstration of this device represents a next step in better understanding of properties and possibilities offered by metamaterials as well as advance in quest of possible applications.

This concludes our overview of the history, development and latest progress in the field of negative index metamaterials. In the next section we will briefly talk about key moments describing new application and physics proposed and developed in the course of this dissertation.

1.5 New applications and physics developed in the course of this thesis

As it was mentioned earlier the infrared spectral region is of a particular interest for the modern research community. If we look at the electric permittivity of the metal defined as:

$$\varepsilon(\omega) = 1 - \frac{\omega_p^2}{\omega(\omega + i\gamma)} \quad 1.26$$

where ω_p is the plasma frequency, ω is the frequency of the incident light and the γ is the damping term, then we can distinguish 3 regions based on the change in the metal properties. When $\omega > \omega_p$ we are in the UV regime and the metal has a very poor performance. When $\omega < \omega_p$ and $\omega \gg \gamma$ we are in the IR regime and the metals have a lossy plasmonic characteristics. And finally when $\omega \ll \gamma$ we are in the RF regime and metals have a highly conductive properties. We will be working in the plasmonic regime in the IR wavelength range. In the far infrared (FIR) wavelength spectra most commonly used dielectric have an absorption peak. It is of interest to consider the coupling between the metamaterial resonance and an absorbing species located in the metamaterial unit cell. We will present the experimental data and physical models for the fishnet metamaterial structure, where the dielectric spacer layer contains a simple Lorentzian like electric-dipole resonance. Simple resonance coupling model was constructed to investigate the effect of adding a dielectric with a dipole absorption peak to a fishnet metamaterial. Anti-crossing behaviors and an exchange of oscillator strength as metamaterial structural resonance is tuned through the absorption resonance were obtained.

Rigorous coupled wave analysis, an algorithm used to calculate the normal incidence transmission and reflection of periodic structures, was used for detailed numerical modeling. Response of the fishnet structure with a dielectric material without an absorber shows only a single resonant peak, resulting from the coupling of the broadband negative ϵ with the structurally resonant negative μ associated with the LC circuit between the two metal plates. With the addition of a dipole absorber in the dielectric, the fishnet exhibits doubly resonant behavior. Presence of an *electric dipole* resonance in the dielectric of the fishnet structure manifests itself in a modification of the *magnetic permeability*, which in turn modifies the negative index behavior. Anti-crossing behavior of the two resonances is obtained. RCWA calculation and the simple model are in good agreement.

A set of experimental samples were fabricated using standard lithographic processing. An Al-BCB-Al fishnet structure was used. Transmission data was obtained by FTIR. Plotting positions of the resonance peaks in the transmission response against ω_0 clearly shows coupling between the resonances with hybridization behavior. Detailed discussion and results can be found in the Chapter 2.

Scaling of the metamaterial fishnet structure to the near-infrared wavelengths, in particular to the near infrared specter ($\sim 1.55 \mu\text{m}$), and to the more challenging visible frequencies requires creation of the robust, highly adaptive optical tool. As the resonance wavelength of the metamaterial structure is pushed in the shorter spectra processing tools faces the tough demands for higher and higher resolution capabilities. We are addressing those challenges by creating an Imaging Interferometric Lithography tool.

The minimum half-pitch feature optical lithography can access is given by the well-known equation, $CD=0.25\lambda/(n\sin\theta)$, where λ is the exposure wavelength, n is the refractive index of the immersion medium and the two beams propagate at angles of $\pm\theta$ with respect to the wafer surface normal. For 244-nm exposures tool in air ($n = 1.0$) and a maximum numerical aperture of 0.9, the minimum accessible half-pitch is 68-nm. For an imaging system, the ultimate resolution does not reach this level as a result of the need to capture the information in the pattern-dependent sidebands around the fundamental frequency. Assuming that a bandwidth of $\sim 10\%$ around the center frequency is needed for a typical pattern, a system with these capabilities should be able to print ~ 75 -nm half-pitch patterns. Typically, resolution enhancement techniques such as optical proximity correction (OPC) and phase-shift masks (PSM) are necessary to approach this resolution with typical patterns.

Imaging Interferometric Lithography (IIL), combining off-axis illumination at the limits of the pupil along with pupil-plane filters, to ensure a uniform frequency-space coverage and multiple exposures covering different regions of spatial frequency space, is a relatively new imaging concept that provides an approach to accessing this fundamental, linear-systems-resolution limits of optics, with simple binary chrome-on-glass masks without any requirement for either OPC or PSM. IIL eases many of the constraints that limit the capabilities of conventional optical lithography and offers a path to the ultimate linear systems limits of optics of dense CDs of $\sim\lambda/3NA$ ($NA=n\sin\theta$ for immersion) for arbitrary patterns. Thus, IIL is similar to quadrupole off-axis illumination with a small partial coherence for each off-axis illumination beam, and with the quadrupole oriented along the principal (x, y) axes of a Manhattan geometry pattern to

maximize the extent of the spatial frequency capture. The x - and y -axis spatial frequencies are covered with separate off-axis illumination exposures. The choice of proper polarization for the high spatial frequency components in orthogonal directions dramatically improves the image contrast and the resist patterns. TE polarization retains full contrast while the contrast of TM is reduced and phase shifted at higher angles. As NAs are increased even further with the use of liquid immersion techniques, control over the light polarization will become a critical issue.

Quadrupole (and double-exposure dipole) off-axis illumination inherently overemphasize low frequencies because each of the exposures redundantly covers the same low-frequency information, while the high frequencies are covered only in individual exposures. Pupil plane filters can be used to eliminate these multiple coverages and thereby provide a uniform transfer function and an improved image.

We have constructed a $22\times$ reduction imaging interferometric lithography testbed using a 244-nm, cw Ar-ion laser source and a small-field 0.9- NA imaging lens. Demonstrations of printing non-periodic (arbitrary) 113-, 100-, 90- and 86-nm ($\kappa_1 \sim 0.32$) half-pitch patterns are reported [39, 40]. Good imaging was achieved with simple binary, WYSIWYG, chrome-on-glass masks without the use of any additional RETs. Experiments are currently underway with smaller patterns to evaluate the resolution limit of the system.

Extension to smaller patterns can be evaluated using the simple scaling equation $CD \propto \lambda/NA$. Switching to a 193-nm source and a 1.3 NA (for H_2O immersion) leads directly to 61-nm half-pitch from 113-nm, 55-nm half-pitch from 100-nm and ~ 45 -nm

half-pitch from 86-nm – again without the need for any mask-based RETs such as phase shift or OPC.

The essential point is that robust imaging for a 45-nm half-pitch is available using IIL without any additional mask-based RETs. The implication is that IIL will allow minimization of the use of mask-based RETs, thereby reducing mask cost. Also it provides an excellent highly adaptive experimental optical tool that meets modern demands for high resolution. Detailed discussion and results can be found in the Chapter 3.

Since we have an access to the optical tool that provides us with reliable sub 100 nm resolution we can turn our attention towards practical application for the metamaterials operating in the NIR wavelength spectra. Here we present the first theoretical simulations of a slab GRIN positive lens operating in the NIR ($\sim 1.55 \mu\text{m}$) and based on our recently reported structure [41]. This represents a significant advance toward applications as well as steps forward in design complexity and construction technique. We demonstrate results of numerical simulation along with the preliminary experimental results for the 1D focusing [42] Full 2D simulation is currently being developed.

The NIM structure: a negative electric permittivity (ϵ) that results from an array of thin metal wires parallel to the direction of electric field and a negative magnetic permeability (μ) resulting from a pair of finite-width metal stripes separated by a dielectric layer along the direction of the incident magnetic field. Zhang's theoretical work [43], leads to the conclusion that values of ϵ and μ , at a fixed wavelength of the incident light, can be independently controlled by manipulating the width of the metal

wires, shifting the resonance frequency of the structure and so changing the value of the refractive index $n = \sqrt{\mu\epsilon}$, while keeping small variations in the impedance and hence in the transmission. In 2007 Ku showed that NIMs with rectangular holes [44], have better impedance matching hence better transmission.

A full parametric study was performed on a 4 – layered Au/Dielectric/Au/Substrate “fishnet” type structure with rectangular apertures in order to understand the impact of changing physical sizes (pitch and CD) of the unit cell as well as the materials used for the dielectric layer. Optimization of the different parameters (physical size of the unit cell, layers thicknesses, and dielectric materials) were performed in order to obtain largest possible phase shift while restricting the transmission variation across the sample to $\leq 10\%$. These studies with 3 types of dielectric materials – Sapphire, Silicon Nitride and amorphous Si revealed the three best performing structures.

Theoretical simulation of the graded index optical lens with inhomogeneous NIMs has shown that for the $(64 \times 64)\lambda^2$ area experimental samples, with small edge effects, a $f/26$ lens can be achieved. We think that the F number can be significantly improved by stacking several layers of NIMs structures which should provide us with higher phase shift and thus stronger focusing. Detailed discussion and demonstration of the simulation and preliminary experimental results can be found in Chapter 4.

The outline for the thesis work is:

- In Chapter 2 the magnetic hybridization of the electric dipole resonance in the fishnet metamaterial is demonstrated. Detailed physical model and more rigorous numerical calculation along with the experimental data are presented.

- In the Chapter 3 experimental demonstration of the Imaging Interferometric Tool capable of reaching the ultimate linear system resolution limits of optics of dense CDs $\sim\lambda/3NA$ is presented. Detailed discussions including experimental results along with modeling results from the PROLITH simulation tool are reported.
- In the Chapter 4 the first numerical simulation of an inhomogeneous metamaterials for the thin-film lenses is presented. Detailed numerical simulations and preliminary experimental results for a slab GRIN lens operating in the NIR ($\sim 1.55 \mu\text{m}$) wavelength regime are demonstrated.
- Appendix A has a list of conference presentations and publications that has been done in the course of this work.

1.6 References

1. G. Veselago, The electrodynamics of substances with simultaneously negative values of ϵ and μ , *Sov Phys. Uspekhi* vol. 10, pp. 509,1968.
2. J. B. Pendry, A. J. Holden, D. J. Robbins, and W. J. Stewart “Magnetism from Conductors and Enhanced Nonlinear Phenomena” *IEEE Trans. on Microwave Theory and Tech.*, **47**, 2075 (1999).
3. D. R. Smith, W. J. Padilla, D. C. Vier, S. C. Nemat-Nasser, and S. Schultz, “Composite medium with simultaneously negative permeability and permittivity,” *Phys. Rev. Lett.* **84**, 4184-4187 (2000).
4. R. A. Shelby, D. R. Smith, and S. Schultz, “Experimental verification of a negative index of refraction,” *Science* **292**, 77-79 (2002).
5. A. A. Houck, J. B. Brock, and I. L. Chuang, *Phys. Rev. Lett.* **90**, 137401 (2003).
6. J. B. Pendry, A. J. Holden, W. J. Stewart, I. Youngs “Extremely Low Frequency Plasmons in Metallic Mesostructures” *Phys. Rev. Lett.*, **76**, 4773 (1996).
7. J. B. Pendry, A. J. Holden, D. J. Robbins and W. J. Stewart “Low frequency plasmons in thin-wire structures” *Journal of Physics: Condensed Matter*, **10**, 4785 (1998).
8. T. J. Yen, W. J. Padilla, N. Fang,, D. C. Vier, D. R. Smith, J. B. Pendry, D. N. Basov and X. Zhang, “Terahertz Magnetic Response from Artificial Materials” *Science* **303**, 1494 (2004).
9. S. Linden, C. Enkrich, M. Wegener, J. Zhou, T. Koschny, C. M. Soukoulis, “Magnetic Response of Metamaterials at 100 Terahertz” *Science* **306**, 1351 (2004).

-
10. S. Zhang; W. J. Fan; B. K. Minhas; A. Frauenglass; K. J. Malloy and S. R. J. Brueck, "Midinfrared resonant magnetic nanostructures exhibiting a negative permeability", *Phys. Rev. Lett*; **94**, 037402 (2005).
 - 11 J. Zhou, Th. Koschny, M. Kafesaki, E. N. Economou, J. B. Pendry and C. M. Soukoulis, "Saturation of the Magnetic Response of Split-Ring Resonators at Optical Frequencies", *Phys. Rev. Lett*; **95**, 223902 (2005).
 - 12 S. Zhang, W. Fan, N. C. Panoiu, K. J. Malloy, R. M. Osgood and S. R. J. Brueck, "Experimental demonstration of near-infrared negative-index metamaterials," *Phys. Rev. Lett.* **95**, 137404 (2005).
 - 13 V. M. Shalaev, W. Cai, U. K. Chettiar, H-K. Yuan, A. K. Sarychev, V. P. Drachev and A. V. Kildishev, "Negative index of refraction in optical metamaterials," *Opt. Lett.* **30**, 3356-3358 (2005).
 - 14 G. Dolling, M. Wegener, "Negative index metamaterial at 780 nm wavelength", *Opt. Lett.* **32**, N1 (2007).
 - 15 S. Xiao, U. K. Chettiar, A. V. Kildishev, V. P. Drachev, and V. M. Shalaev, "Yellow-light negative-index metamaterials," *Opt. Lett.* **34**, 3478-3480 (2009).
 - 16 J. B. Pendry, "Negative refraction makes a perfect lens," *Phys. Rev. Lett.* **85**, 3966-3969 (2000).
 17. N. Garcia and M. Nieto-Vesperinas, "Left-Handed Materials Do Not Make a Perfect Lens", *Phys. Rev. Lett.*, **88**, 207403 (2002).
 18. J. B. Pendry, Comment on "Left-Handed Materials Do Not Make a Perfect Lens" *Phys. Rev. Lett.* **91**, 099701 (2003).

-
19. D. R. Smith, D. Schurig, M. Rosenbluth, S. Schultz, S. A. Ramakrishna and J. B. Pendry, "Limitations on subdiffraction imaging with a negative refractive index slab", *Appl. Phys. Lett.*, **82**, 1506 (2003).
- 20 P. Vodo, P. V. Parimi, W. T. Lu, and S. Sridhar, *Appl. Phys. Lett.* **86**, 201108 (2005).
- 21 C. G. Parazzoli, R. B. Greegor, J. A. Nielsen, M. A. Thompson, K. Li, A.M. Vetter, M. H. Tanielian, and D. C. Vier, *Appl. Phys. Lett.* **84**, 17 (2004).
- 22 R. B. Greegor, C. G. Parazzoli, J. A. Nielsen, M. A. Thompson, M. H. Tanielian, and D. R. Smith, *Appl. Phys. Lett.* **87**, 091114 (2005).
- 23 <http://xlab.me.berkeley.edu/research/hyperlens.html>
- 24 Hyesog Lee, Zhaowei Liu, Yi Xiong, Cheng Sun and Xiang Zhang, "Development of optical hyperlens for imaging below the diffraction limit", *Optics Express*, **15**, 15886, (2007).
- 25 Zhaowei Liu, Hyesog Lee, Yi Xiong, Cheng Sun and Xiang Zhang, "Far-Field Optical Hyperlens Magnifying Sub-Diffraction-Limited Objects", *Science*, **315**, 1686, (2007).
- 26 Nicholas Fang, Hyesog Lee, Cheng Sun, Xiang Zhang, "Sub-Diffraction-Limited Optical Imaging with a Silver Superlens", *Science*, **308**, 534-537, (2005).
- 27 Stéphane Durant, Zhaowei Liu, Jennifer M. Steele, and Xiang Zhang, "Theory of the transmission properties of an optical far-field superlens for imaging beyond the diffraction limit", *J. Opt. Soc. Am. B*, **23**, No. 11, 2383-, 2392, (2006).
- 28 Zhaowei Liu, Stéphane Durant, Hyesog Lee, Yuri Pikus, Nicolas Fang, Yi Xiong, Cheng Sun, and Xiang Zhang, "Far-field Optical Superlens", *Nano Letters*, **7**, 403, (2007).

-
- 29 Zhaowei Liu, Stéphane Durant, Hyesog Lee, Yuri Pikus, Yi Xiong, Cheng Sun and Xiang Zhang, "Experimental studies of far-field superlens for sub-diffractive optical imaging", *Optics Express*, **15**, 6947,(2007).
- 30 D. Schurig, J. J. Mock, B. J. Justice, S. A. Cummer, J. B. Pendry, A. F. Starr, D. R. Smith "Metamaterial electromagnetic cloak at microwave frequencies" *Science* **314**, 977, (2006).
- 31 J. B. Pendry, D. Schurig, D. R. Smith, *Science*, **312**, 1780 (2006).
- 32 U. Leonhardt, *Science*, **312**, 1777 (2006).
- 33 Free space microwave focusing by a negative-index gradient lens, T. Driscoll, D.N. Basov, A.F. Starr, P.M. Rye, S. Nemat-Nasser, D.Schurig and D.R. Smith, *Appl. Phys. Lett.* **88**, 081101 (2006).
- 34 Padilla, W. J.; Taylor, A. J.; Highstrete, C.; Lee, M.; Averitt, R. D. *Phys. Rev. Lett.* **96**, 107401, (2006).
- 35 Chen, H. T.; Padilla, W. J.; Zide, J. M. O.; Bank, S. R.; Gossard, A. C.; Taylor, A. J.; Averitt, R. D. *Opt. Lett.*, **32**, 1620–1622, (2007).
- 36 Kim, E.; Shen, R. Y.; Wu, W.; Ponizovskaya, E.; Yu, Z.; Bratkovsky, A. M.; Wang, S.; Williams, R. S., *Appl. Phys. Lett.*, **91**, 173105, (2007).
- 37 Keshav M. Dani, Zahyun Ku, Prashanth C. Upadhy, Rohit P. Prasankumar, S. R. J. Brueck, and Antoinette J. Taylor, "Subpicosecond Optical Switching with a Negative Index Metamaterial", *Nano Letters*, **9**, 3565-3569 (2009).
- 38 David J. Cho, Wei Wu, Ekaterina Ponizovskaya, Pratik Chaturvedi, Alexander M. Bratkovsky, Shih-Yuan Wang, Xiang Zhang, Feng Wang and Y. Ron Shen, "Ultrafast modulation of optical metamaterials", *Optics Express*, **17**, 20, 17652, (2009).

-
- 39 A. Frauenglass, S. Smolev, A. Biswas, S.R.J. Brueck, *Jour. Vac. Sci. Technol.* **22**, 3465-3469 (2004).
- 40 Svjatoslav Smolev, A. Biswas, A. Frauenglass, and Steven R. J. Brueck, "244-nm imaging interferometric lithography test bed", *Proc. SPIE*, Vol. **6154**, 61542K (2006).
- 41 Shuang Zhang, Wenjun fan, N. C. Panoiu, K. J. Malloy, R. M. Osgood, S. R. J. Brueck, "Demonstration of metal–dielectric negative-index metamaterials with improved performance at optical frequencies", *J. Opt. Soc. Am. B*, Vol. **23**, No. 3, (2006).
- 42 S. Smolev, S. R. Bruck, "Graded index optical lens using inhomogeneous metamaterials", in *Proc. Conference on Lasers and Electro-Optics, Advanced Materials and Methods*, San Jose, (2008).
- 43 Shuang Zhang, Wenjun Fan, K. J. Malloy and S. R. J. Brueck, N. C. Panoiu and R. M. Osgood, "Near-infrared double negative metamaterials", *Optics Express*, Vol. **13**, No. 13, 4922, (2005).
- 44 Zahyun Ku and S. R. J. Brueck, "Comparison of negative refractive index materials with circular, elliptical and rectangular holes", *Optics Express*, Vol. **15**, No. 8, 4515, (2007).

Chapter 2 Resonant Coupling to a Dipole Absorber Inside a Metamaterial: Hybridization of the Negative Index Response

2.1 Introduction

As discussed in the Chapter 1, research activity in the physics and applications of the negative index metamaterials (NIMs) has grown tremendously since first theoretical introduction and experimental demonstration. Negative index metamaterials have been demonstrated across the wide range of wavelengths, from the microwaves (RF) and to visible. The infrared spectral region is of a particular interest for the modern research community. If we look at the electric permittivity of the metal defined as:

$$\varepsilon(\omega) = 1 - \frac{\omega_p^2}{\omega(\omega + i\gamma)} \quad (2.1)$$

where ω_p is the plasma frequency, ω is the frequency of the incident light and the γ is the damping term, then we can distinguish 3 regions based on the change in the metal properties. When $\omega > \omega_p$ we are in the UV regime and the metal has a very poor performance. When $\omega < \omega_p$ and $\omega \gg \gamma$, we are in the IR regime and the metals have a lossy plasmonic characteristics. And finally when $\omega \ll \gamma$ we are in the RF regime and metals have a highly conductive properties. We will be working in the plasmonic regime in the IR wavelength range, where metamaterials are easy to fabricate due to a relatively large size. There is a strong coupling within the metamaterial and the effective permittivity (ε) is negative everywhere and effective permeability (μ) is negative at the resonance. However most commonly used dielectrics have an absorption peak in the wavelength region of interest. Usually we are trying to avoid this peak in the design

process but for some applications like novel optical sensors, optical switches or spectroscopy it is of interest to consider the coupling between the metamaterial resonance and an absorbing species located in the metamaterial unit cell. Understanding an effect of adding a dipole absorption resonance in the dielectric in proximity of the metamaterial resonance is very important from physical and application points of view.

In this Chapter numerical model and experimental results for a fishnet metamaterial with the dielectric spacer layer containing a simple Lorentzian electric-dipole resonance are demonstrated. A classical anti-crossing behaviour with hybridization of resonances and exchange of the oscillator strength is observed. Detection of absorption in novel sensors and use of absorption excitation to alter and switch the metamaterial optical properties are possible applications for these phenomena.

2.2 Simple physical model

A simple resonance coupling model was constructed to investigate the physical effect of adding a dielectric with a dipole absorption peak to a fishnet metamaterial. The negative index of refraction in this structure comes from two parts: (1) a negative electric permittivity (ϵ) that results from an array of thin metal wires parallel to the direction of electric field; and (2) a negative magnetic permeability (μ) resulting from a pair of finite-width metal stripes separated by a dielectric layer along the direction of the incident magnetic field. Figure 2.1 shows a side view of the fishnet metamaterial structure.

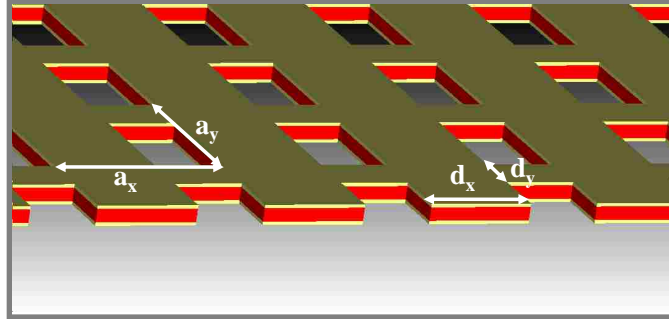


Fig. 2.1 Side view of the fishnet metamaterial structure. Geometrical parameters are indicated and the dielectric material (red) is sandwiched between metal layers (brown).

An array of paired metallic stripes oriented along the direction of magnetic field vertically separated by a dielectric layer can exhibit a magnetic (LC tank circuit demonstrated on the Figure 2.2) resonance with a negative effective permeability over a limited wavelength range and often can be described using a Lorentzian-like response [1,2]. The resonance wavelength has a linear relation to the stripe linewidth.

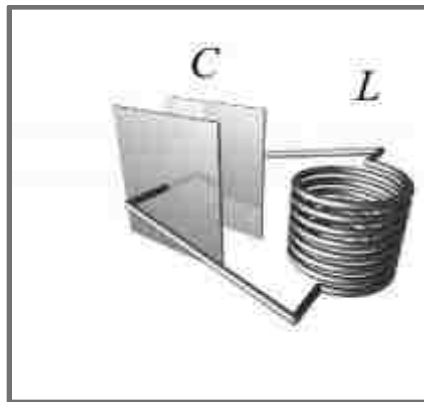


Fig. 2.23 Graphical representation of simple LC circuit model that can be used to describe physical behaviour of fishnet metamaterial.

Following O'Brien *et al.*[2, 3], we describe the effective permeability of the fishnet structure for the magnetic field applied perpendicular to the plane of the unit cell as:

$$\mu_{\text{eff}} = \frac{F}{1 - F} \quad (2.2)$$

Where the metamaterial resonance is characterized by a resonance frequency $\omega_0 = 9.1 \mu\text{m}$ (0.136 eV). Figure 2.3 shows a plot of the modeled, by the set of empiric number, effective permeability μ_{eff} as a function of ω . Those empiric numbers were chosen to mimic the effective permeability response of a standard fishnet structure and are: a linewidth $\gamma_0 = 0.33$, and a fill factor $F (\sim 0.2)$.

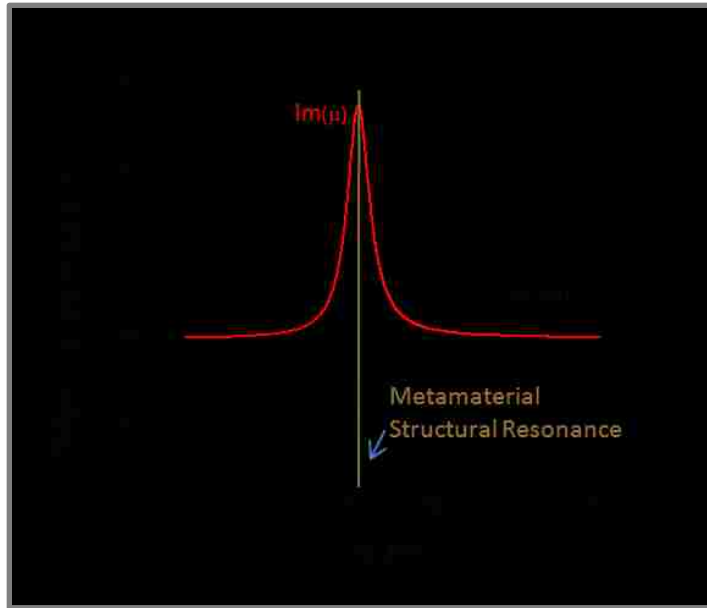


Fig. 2.3 Plot of the effective permeability (μ_{eff}) of the fishnet metamaterial with *metamaterial structural resonance* (MSR) $\omega_0 = 9.1 \mu\text{m}$; linewidth (γ_0) = 0.33; and fill factor (F) = 0.2.

In terms of the equivalent circuit parameters:

$$\blacksquare \blacksquare \frac{1}{LC} \blacksquare \frac{1}{LC} \blacksquare_{bs} \quad (2.3)$$

Here C_0 is the capacitance without the absorber, and the absorber dielectric function in the form of a simple Lorentzian electric-dipole resonance has been explicitly separated out.

Using the standard [4] expression for a Lorentzian absorption:

$$\epsilon_{obs} = 1 + \frac{A}{\omega_1^2 - \omega^2 - j\gamma_1\omega} \quad (2.4)$$

Where $A = 8 \times 10^{-4}$ and is related to the oscillator strength, $\gamma_1 = 3.5 \times 10^{-3}$ is the inverse linewidth, and $\omega_1 = 9.5 \mu\text{m}$ (0.130 eV) is the resonance frequency of the electric dipole transition. Figure 2.4 shows plot of the absorber dielectric function.

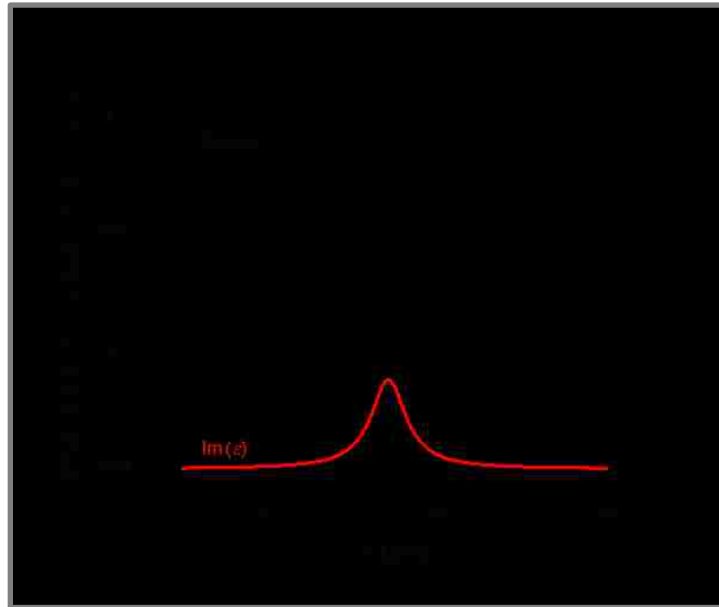


Fig. 2.4 Plot of the absorber dielectric function with resonant frequency (ω_0) = 9.5 μm ; linewidth (γ_0) = 3.3 $\times 10^{-5}$; and fill factor (A) = 8 $\times 10^{-4}$.

Substituting complex eqn. 2.3 back in the eqn. 2.2 will give an effective permeability response in the presence of the absorption peak as a function of the frequency ω as it shown on Figure 2.5.

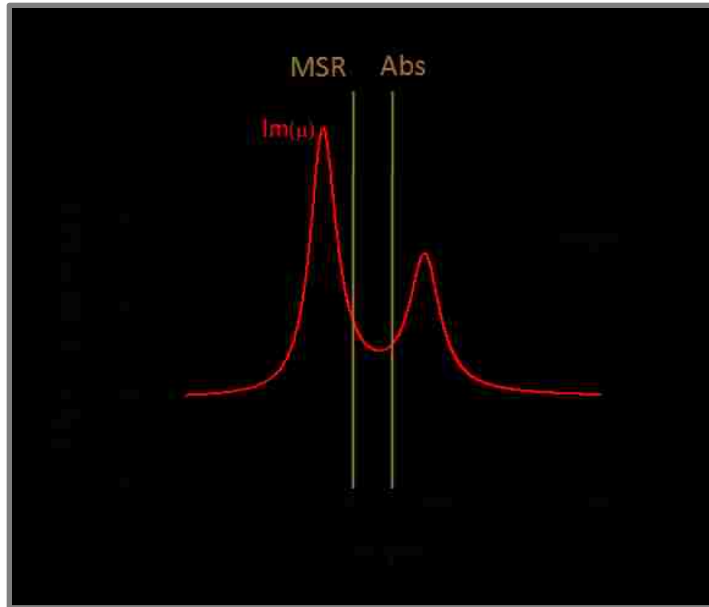


Fig. 2.5 Plot of the effective permeability (μ_{eff}) of the fishnet metamaterial with the presence of the absorber peak. Metamaterial structural resonance (MSR) (ω_0) = 9.1 μm ; linewidth (γ_0) = 0.33; and fill factor (F) = 0.2. Absorber resonant frequency (Abs) (ω_0) = 9.5 μm ; linewidth (γ_0) = 3.3×10^{-5} ; and fill factor (A) = 8×10^{-4} .

When there is no absorber present in the material, a conventional single resonance peak is visible in the effective permeability response, however adding the dipole absorber near the structural resonance leads to hybridization of the electric dipole and magnetic dipole resonances, and a double peak result. Tuning the metamaterial structural resonance through the absorber resonance we obtain an anti-crossing behavior as it shown in Figure 2.6.

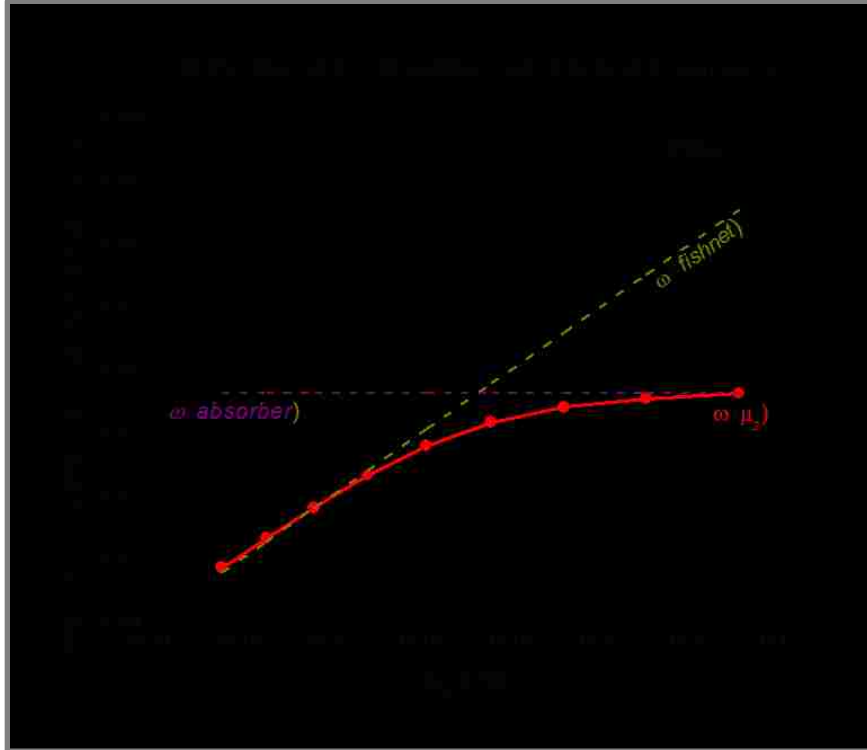


Fig. 2.6 Hybridization of resonances with an anti-crossing behaviour and sharing of oscillator strength as the metamaterial structural resonance is tuned through the absorption resonance.

The magnitude of the anti-crossing gap is determined by the oscillator strength A .

Next step will be to demonstrate the same effect using the more rigorous coupled wave analysis and also compare it to the result from the commercial microwave studio software (CST).

2.3. Numerical modeling

2.3.1 Extraction of the optical parameters of the metamaterial structure

Rigorous coupled-wave analysis (RCWA) [5,6], is a commonly used algorithm to calculate the transmission and reflection of periodic structures, and is used for detailed numerical modeling of the resonance hybridization behavior. This algorithm can calculate transmission and reflection coefficients. Those coefficients are then used to

extract, using the method proposed by Smith *et al.* [7], effective parameters of the fishnet structure such as:

- n – effective refractive index,
- η - impedance,
- ε – effective permittivity and
- μ - effective permeability

For a uniform layer of material with thickness of d , with both the incident and outgoing media as air ($n_{inc} = 1$, $n_{out} = 1$), the complex coefficients of transmission and reflection are given as

$$\frac{1}{t} \cos(nkd) - \frac{i}{2} \left(\frac{1}{t} - \frac{r}{t} \right) \sin(nkd) \quad (2.5)$$

$$\frac{r}{t} - \frac{i}{2} \left(\frac{1}{t} + \frac{r}{t} \right) \sin(nkd)$$

If t and r are known, we can invert equation (2.4) to obtain n , which is given by

$$\cos(nkd) = \frac{1 - \frac{r^2}{t^2}}{2t} \quad (2.6)$$

And next, the impedance η is expressed in terms of t , r and n as

$$\frac{i}{t} \left(\frac{1}{t} - \frac{r}{t} \right) \cos(nkd) \quad (2.7)$$

$$\sin(nkd)$$

In equations (2.6) to (2.7), all the parameters are complex. Care needs to be taken when using equation (2.6) to determine the complex values of n because of the cosine

function has multiple branches. Because the metamaterial structure is passive, we can instantly determine that the sign of the imaginary part of n has to be positive. For the real part of n , simulating the metamaterial slab with different thickness can help determine which branch to take. An alternative way is to first determine the refractive index in the long wavelength limit far off the resonance, and trace back the value of n across the resonance because n and the derivative of n have to be continuous in wavelength across the whole range.

Next, we generalize the calculation for the case of unsymmetrical incident and outgoing media. For the incident medium of air and outgoing medium with an index of n_{sb} , the coefficient of transmission and reflection are given as

$$\begin{aligned} \frac{1}{t} &= \frac{n_{sb}}{2} \cos(nkd) + \frac{1}{2} (n_{sb} - 1) \sin(nkd) \\ \frac{r}{t} &= \frac{n_{sb}}{2} \cos(nkd) - \frac{1}{2} (n_{sb} - 1) \sin(nkd) \end{aligned} \quad (2.8)$$

After inverting equations (2.8), we obtain the expressions for n and η as

$$\begin{aligned} \cos(nkd) &= \frac{1 - n_{sb}^2 r^2}{[n_{sb}(1 - r^2) + t^2]} \\ \frac{i}{t} &= \frac{\cos(nkd)}{n_{sb} \sin(nkd)} \end{aligned} \quad (2.9)$$

However there is another approach originally proposed by Pendry *et al.*[8], which uses averaging of the fields to extract needed effective parameters.

Because of the inhomogeneous nature of metamaterials, electrical field and magnetic field need to be averaged in order to obtain the effective permeability and permittivity. The effective permittivity and permeability are defined as

$$\begin{aligned} \mathbf{B}_{ave} &= \langle \mathbf{B} \rangle \\ \mathbf{H}_{ave} &= \langle \mathbf{H} \rangle \\ \mathbf{D}_{ave} &= \langle \mathbf{D} \rangle \\ \mathbf{E}_{ave} &= \langle \mathbf{E} \rangle \end{aligned} \quad (2.10)$$

Where B_{ave} , H_{ave} , D_{ave} and E_{ave} are the electrical magnetic fields averaged over one unit cell of the composite structures. The question arises as how to average the fields. According to Pendry, the averaging can be obtained from the integral form of Maxwell equations,

$$\begin{aligned} \oint_C \mathbf{H} \cdot d\mathbf{l} &= \int_S \mathbf{D} \cdot d\mathbf{S} \\ \oint_C \mathbf{E} \cdot d\mathbf{l} &= - \int_S \mathbf{B} \cdot d\mathbf{S} \end{aligned} \quad (2.11)$$

Where the line integral is taken over the loop "C" enclosing the area "S". From equation 2.10, it is intuitive to use line integrals to average \mathbf{H} and \mathbf{E} and to average \mathbf{B} and \mathbf{D} using area integral. Assuming the unit cell of the metamaterials is a cubic system with a side length of "a", the averaging of \mathbf{H} is given as

$$\begin{aligned}
(H_{ave})_x &= \frac{1}{V} \int_V E_x^{(a,0,0)} H_x^{(0,0,0)} dV \\
(H_{ave})_y &= \frac{1}{V} \int_V E_y^{(0,a,0)} H_y^{(0,0,0)} dV \\
(H_{ave})_z &= \frac{1}{V} \int_V E_z^{(0,0,a)} H_z^{(0,0,0)} dV
\end{aligned} \tag{2.12}$$

This averaging technique is also applied to the E field. For the B field, the average is given as

$$\begin{aligned}
(B_{ave})_x &= \frac{1}{S} \int_S B_x dS \\
(B_{ave})_y &= \frac{1}{S} \int_S B_y dS \\
(B_{ave})_z &= \frac{1}{S} \int_S B_z dS
\end{aligned} \tag{2.13}$$

And the same formula is used for D field. Finally, the average permittivity ϵ and permeability μ are computed by equation (2.10).

For some simple structures, this method can lead to a closed form, making the calculation of the effective parameters of a metamaterial very convenient. However, for more complex structures where numerical simulation has to be used to calculate the fields, the process of computing average fields becomes very tedious.

Comparing Pendry's method of averaging fields and Smith's methods of extraction the optical parameters, Smith's approach is more accurate and more efficient for our purposes because at each wavelength, only 4 parameters (the real and imaginary parts of t

and r) are required instead of the electric and magnetic fields at a great number of positions inside one unit cell at small grid spacing. Therefore we incorporate Smith's method in our RCWA numerical simulation.

2.3.2 Results of RCWA numerical simulation

In our model the incident light is normal to the surface and both the incident and outgoing media are air. The effect of adding a substrate to the model calculation will be discussed later in this chapter.

A common fishnet structure, as shown on the Figure 2.7, was used for the modeling. The orthogonal pitches of the 2D gratings (a_x , a_y) and the linewidth (critical dimensions, CD: d_x , d_y) used to model a fishnet structure with the resonance at $\sim 9.2 \mu\text{m}$ are listed in Table 2.1.

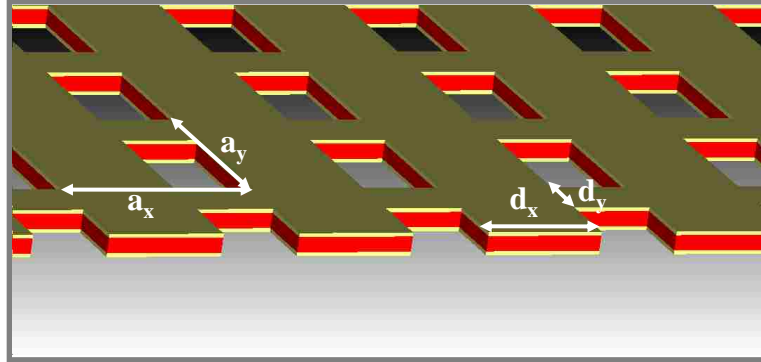


Fig. 2.6 Side view of the metal-dielectric-metal fishnet structure with the geometrical parameters indicated.

Table 2.1 Geometrical parameters for a fishnet structure with structural resonance at $\sim 9.2 \mu\text{m}$.

Pitch (a_x , a_y)	CD (d_x)	CD (d_y)	$n_{\text{dielectric}}$	Al Thickness	Diel. Thickness
$5.2 \mu\text{m}$	$3.12 \mu\text{m}$	$1.56 \mu\text{m}$	1.5	100 nm	800 nm

During our numerical modelling we used same pitch size in the x- and y- direction and results obtained with this approach made us believe that we have a good starting point. However it is possible to have different pitch sizes for the orthogonal directions

and it will be interesting to perform a separate parametric study investigating this effect. Such parametric study will be performed in the future and will not be addressed in the scope of this work.

As an additional validation check for our numerical RCWA model we performed a separate simulation in the commercial software known as a Microwave Studio or CST. This software package is widely used for microwave engineering and analysis, but it can also address our needs. Process for this software starts with creation of a single unit cell with geometrical parameters that will produce a resonance fishnet metamaterial structure with $\lambda_{resonant} = 9.3$. This is our metamaterial structural resonance (MSR).

Numerically modelled, by the RCWA and CST, transmission (left) and effective refractive index (right) response of the fishnet structure with a dielectric material ($n = 1.5$) without an absorption resonance are shown in Fig.2.8.

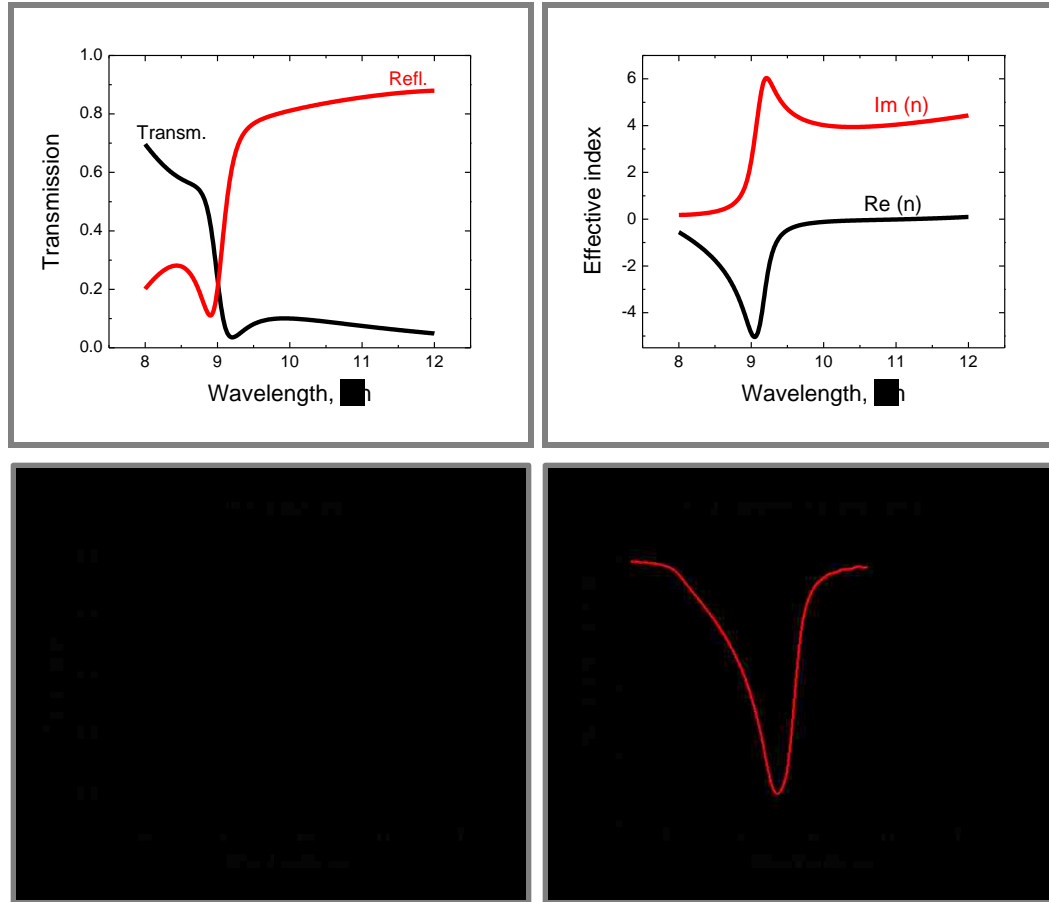


Fig. 2.8 Top: RCWA calculated transmission (left) and effective refractive index (right) of the fishnet structure with dielectric material ($n = 1.5$) without an absorber: a single resonance at $\sim 9.2 \mu\text{m}$ is clearly visible. Bottom: CST calculated transmission (left) and effective refractive index (right) of the fishnet structure with dielectric material ($n = 1.5$) without an absorber. A single metamaterial structural resonance at $\sim 9.3 \mu\text{m}$ is visible. Both models show very good agreement.

As expected, only a single resonant peak is observed in both models, which results from the coupling of the broadband negative permittivity with the structurally resonant negative permeability associated with the LC circuit between the two metal plates.

The addition of a dipole absorber in the dielectric changes the response of the fishnet structure such that it exhibits doubly resonant behavior. This can be observed in the Figure 2.9 showing the modeled by the RCWA and CST, response of the fishnet metamaterial when the dipole absorption resonance is centered at $9.5 \mu\text{m}$.

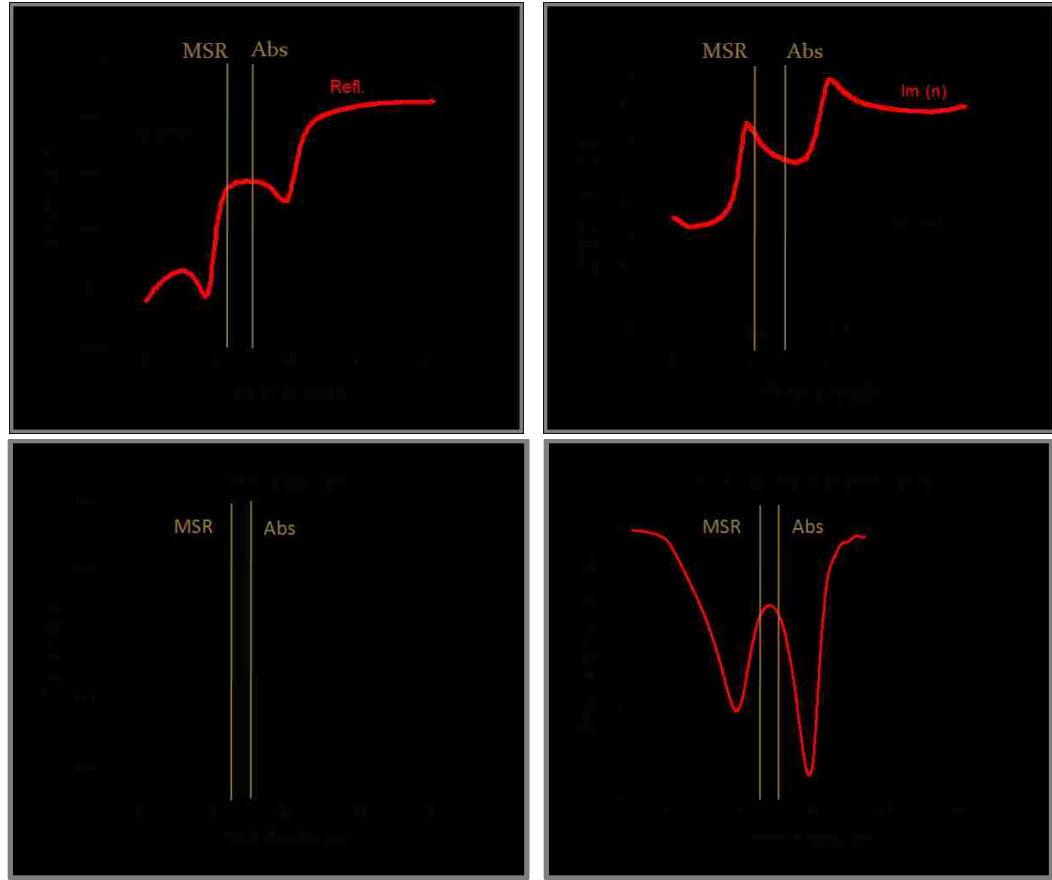


Fig. 2.9: Top: RCWA calculated transmission (left) and effective refractive index (right) of the fishnet structure with the presence of the dipole absorber in the dielectric. Metamaterial structural resonance (MSR), $\omega_0 = 9.2 \mu\text{m}$, and absorption resonance, $\omega_1 = 9.5 \mu\text{m}$. Hybridization of the resonances is clearly visible in the presence of absorber. Bottom: CST calculated transmission (left) and effective refractive index (right) of the fishnet structure with the presence of the dipole absorber in the dielectric. Metamaterial structural resonance (MSR), $\omega_0 = 9.3 \mu\text{m}$, and absorption resonance, $\omega_1 = 9.5 \mu\text{m}$. Hybridization of the resonances is clearly visible in the presence of absorber.

It is interesting to note that the presence of an *electric dipole* resonance in the dielectric of the fishnet structure manifests itself in a modification of the *magnetic permeability*, which in turn modifies the negative index behavior. We have observed an excellent qualitative agreement between RCWA and CST numerical models.

Figure 2.10 shows the anti-crossing behavior of the two resonances obtained with the RCWA simulation for the fishnet with absorber structure and compared with the results of the simple physical model as the center of the dipole transition is tuned through

the bare metamaterial resonance. We also observe an exchange of oscillator strength as the resonances cross.

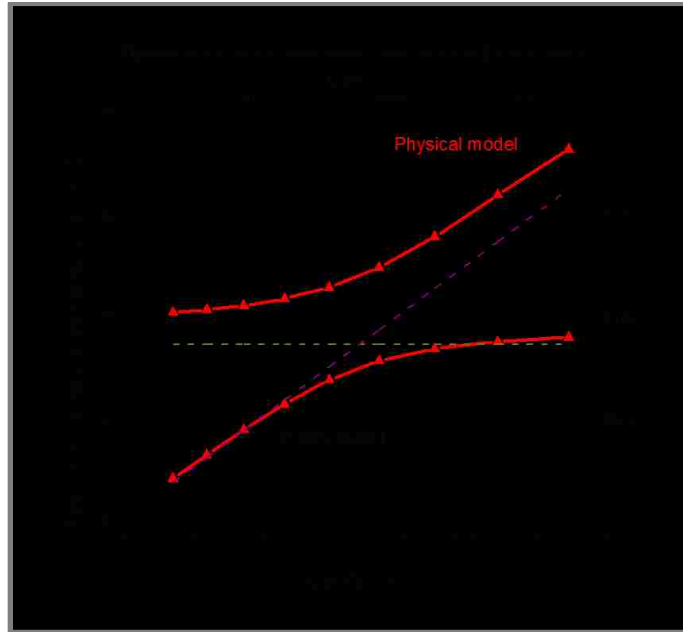


Fig. 2.10 Anti-crossing behavior of the structural and absorption resonances as the electric dipole resonance is tuned through the bare fishnet resonance is clearly observed. A bare fishnet resonance at $9.2 \mu\text{m}$ (0.135 eV) and absorber resonance at $9.5 \mu\text{m}$ (0.130 eV) are assumed. Good qualitative agreement between detailed RCWA calculation (black) and simply physical model (red) is obtained.

There is a good qualitative agreement between simple physical model and RCWA model demonstrating the same anti-crossing behavior.

In the next section we will perform the experimental demonstration of the theoretically observed effect.

2.4. Experimental demonstration

2.4.1 Design of experiment (DOE)

For the experimental demonstration, a fishnet structure consisting of Al and bisbenzocyclobutene – (BCB) was fabricated on a BaF_2 substrate (refractive index of ~ 1.42). The layers of the structure were Al (thickness of 100 nm) on top of BCB

(thickness of 800 nm) on top of Al (thickness of 100 nm). Thicknesses within the functional layer were selected to optimize and maximize transmission of the structure. Figure 2.11 shows measured n ($\text{Re}(n)$) and k ($\text{Im}(n)$) profiles for the BCB dielectric material [9]. There are two absorption peaks in the longwave-infrared (LWIR), one at $8 \mu\text{m}$ (0.155 eV) and another one at $9.5 \mu\text{m}$ (0.130 eV). Since there is no control over position of naturally occurring absorption peaks in the material, we tuned structural resonance of the fishnet structure over range of the 7.4 (0.167 eV) - 10.3 (0.120 eV) μm , covering both absorption peaks in BCB material.

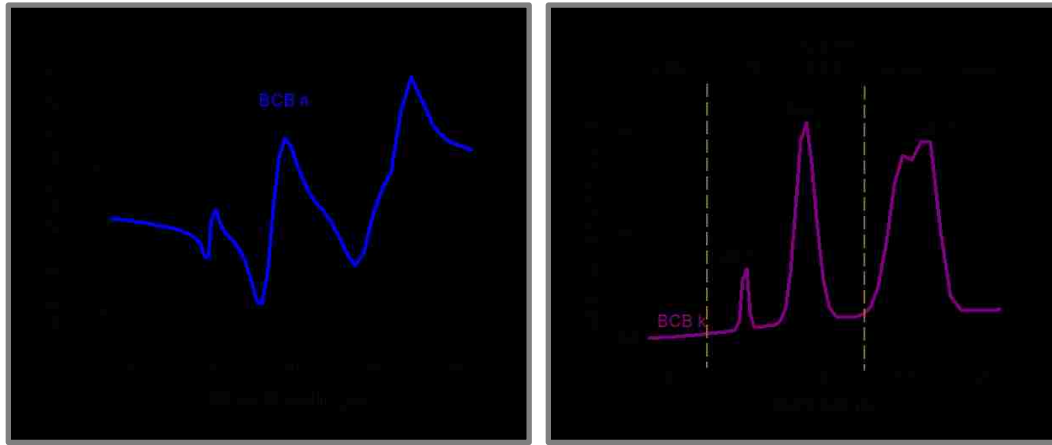


Fig. 2.11 Measured n and k data profiles for the BCB dielectric material used in the designed fishnet structure. 2 distinguishable absorption peaks at $8 \mu\text{m}$ (0.155 eV) and at $9.5 \mu\text{m}$ (0.130 eV) are present in the wavelength range of interest (area between vertical dashed lines).

A set of 7 samples were designed to completely cover the wavelengths of interest. Table 2.2 shows designed physical parameters for each individual sample designated by point A, B and so on.

Table 2.2 Physical parameters for experimental demonstration of hybridization effect: Pitch and CD's in x and y directions for each of 7 samples designated by the points A, B and so on.

Point	Pitch, μm	CD _x , μm	CD _y , μm
Point A	4.4	2.64	1.32
Point B	4.6	2.76	1.38
Point C	4.8	2.88	1.44
Point D	5.0	3.0	1.5
Point E	5.2	3.12	1.56
Point F	5.4	3.24	1.62
Point G	5.6	3.36	1.68

After initial design, numerical RCWA model was carried to verify desired anti-crossing behaviour. Next several figures show results of this RCWA simulation. We start tuning the structural fishnet resonance from the short to long wavelength region. As a fishnet metamaterial resonance is approaching and crossing the first BCB absorption peak we see the transmission and effective refractive index responses as there are demonstrated in the Figure 2.12.

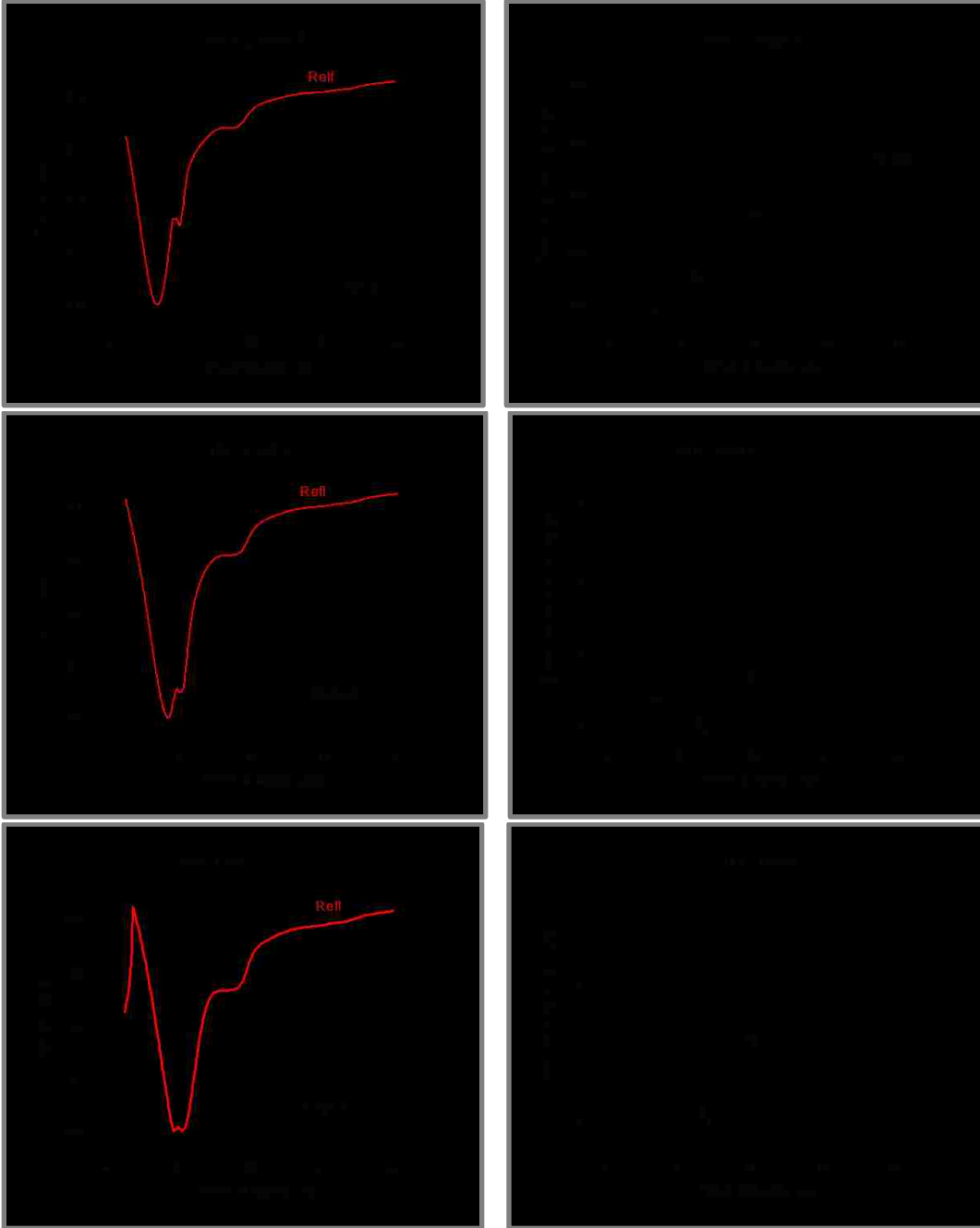


Fig. 2.12 RCWA simulation: transmission response (left) and effective refractive index (right) calculated for **Top**: Point A with the structural resonance at $7.7 \mu\text{m}$ (0.161 eV); **Middle**: Point B with structural resonance at $8.0 \mu\text{m}$ (0.155 eV); **Bottom**: Point C with structural resonance at $8.3 \mu\text{m}$ (0.149 eV).

Three resonance dips are distinguishable in the effective refractive index response as a structural resonance approaches (at $7.7 \mu\text{m}$ (0.161 eV)) and crosses (at $8.0 \mu\text{m}$ (0.155 eV)) the first BCB absorption peak at $7.9 \mu\text{m}$ (0.157 eV). Those hybridized resonance dips are marked as n' , n_1 and n_2 on the top and middle plots of the Figure 2.12. They are

results from the coupling between the structural resonance peak and the closely located first BCB absorption peak and much stronger second BCB absorption resonance at $9.5 \mu\text{m}$ (0.130 eV).

However once a bare structural resonance (at $8.3 \mu\text{m}$ (0.149 eV)) passes the, weaker, first BCB absorption peak, second, much stronger absorption resonance becomes dominant and only two hybridization dips, marked as n_1 and n_2 , are observed on the bottom plot of the Figure 2.12. Weaker BCB absorption resonance (at $7.9 \mu\text{m}$) manifests itself in the small dip in the transmission and effective refractive index response curves at $\sim 8.0 \mu\text{m}$.

Next few figures demonstrates the similar behaviour where the bare structural resonance is approaching and crossing the second, dominating, BCB absorption peak and as a result only 2 hybridized dips are observed in the fishnet metamaterial response. And a first, weaker, BCB absorption resonance, also manifests itself in the form of small dip on all plots at an approximate wavelength of $7.9 \div 8.0 \mu\text{m}$.

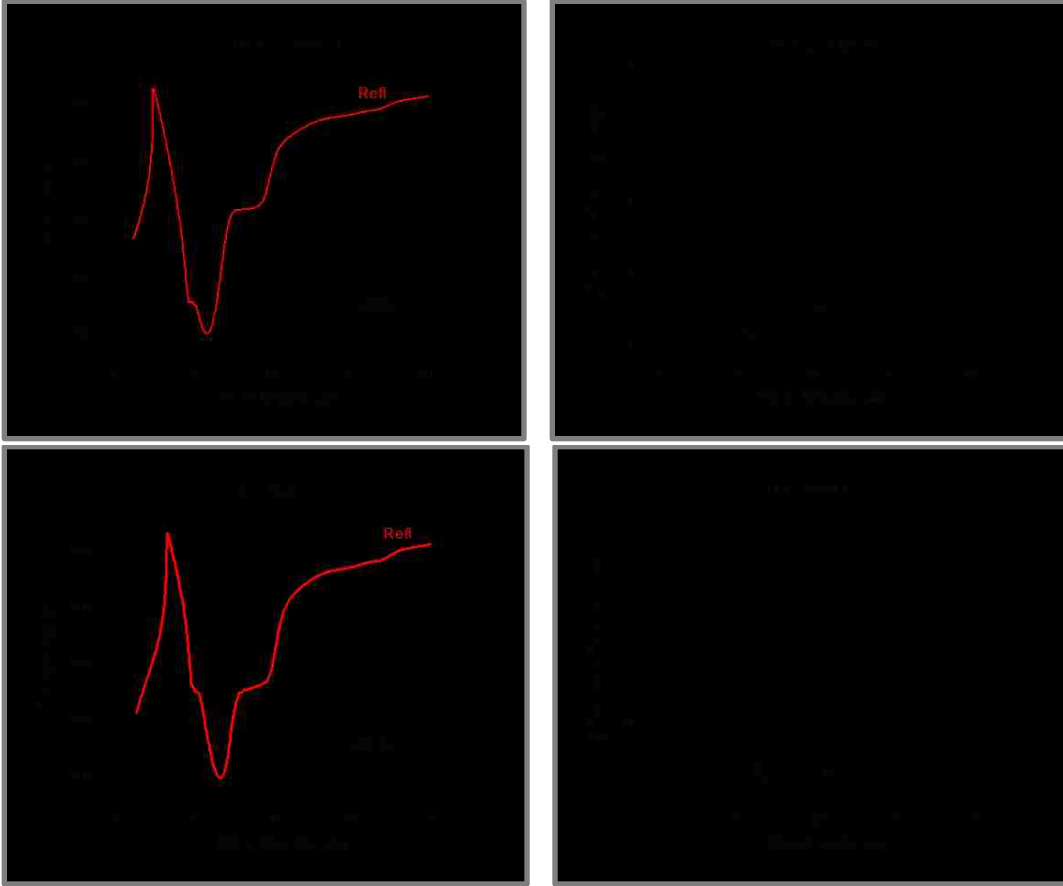


Fig. 2.13 RCWA modelled transmission response (left) and effective refractive index (right) calculated for **Top:** Point D with structural resonance at $8.7 \mu\text{m}$ (0.142 eV); **Bottom:** Point E with structural resonance at $9.1 \mu\text{m}$ (0.136 eV).

In the Figure 2.13 the bare structural resonance was approaching the second BCB absorption resonance and two hybridization dips, marked as n_1 and n_2 are observed on the transmission and effective refractive index fishnet response curves. In the Figure 2.14 the structural resonance crosses the dominant, second, BCB absorption peak.

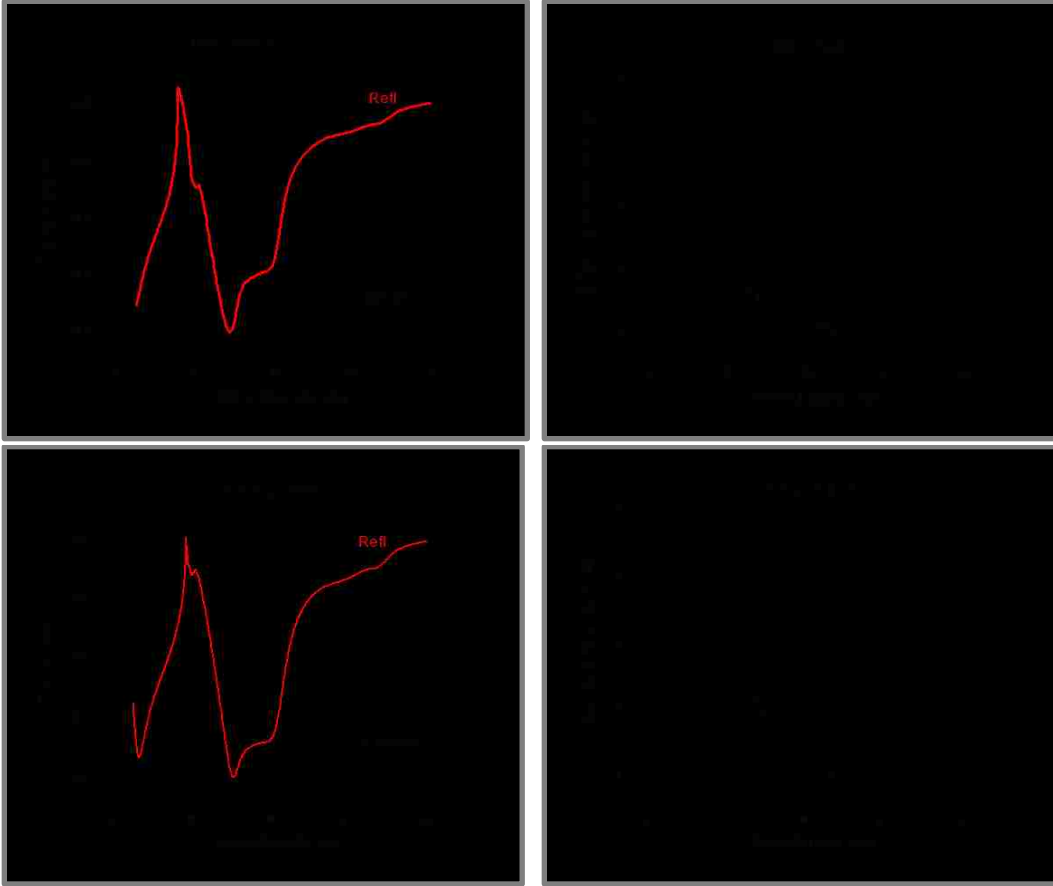


Fig. 2.14 RCWA modelled transmission response (left) and effective refractive index (right) calculated for **Top:** Point F with structural resonance at $9.5 \mu\text{m}$ (0.130 eV); **Bottom:** Point G with structural resonance at $9.8 \mu\text{m}$ (0.126 eV).

As the structural resonance crosses the second BCB absorption resonances we observe the similar behaviour where only 2 hybridized dips are present and a first BCB absorption peak has only a very weak effect and again manifests itself in the form of small dip at $\sim 7.9 \div 8.0 \mu\text{m}$.

Final result demonstrating classical anti-crossing behaviour of resonances obtained by the numerical RCWA simulation is shown in the Figure 2.15. Because there are two absorption peaks present in the BCB material within the range of interest a more complex, but following the similar trend, anti-crossing behaviour of resonances is observed than it was predicted by our previous RCWA and simple physical models.

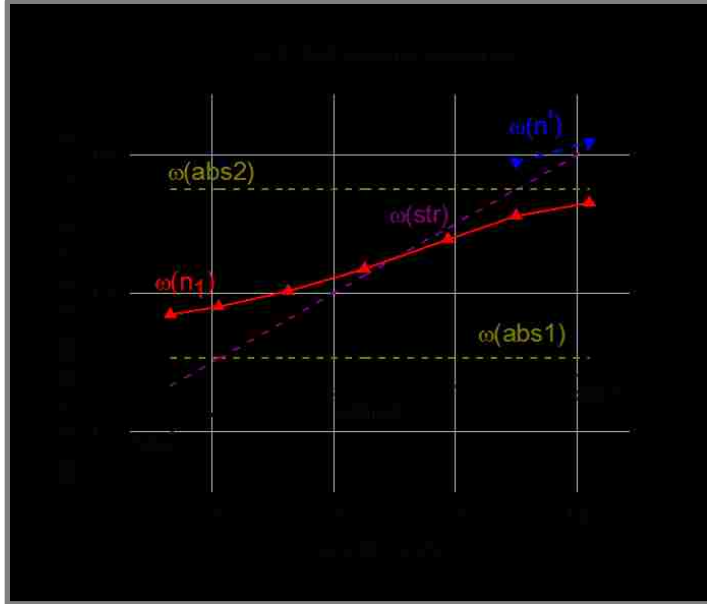


Fig. 2.15 Result of RCWA numerical modelling for the designed anti-crossing behaviour experimental demonstration.

We observe 3 resonance branches. Low and high frequency branches are limited by the bare metamaterial structural and one of the BCB absorption resonances. The middle branch is however limited by both BCB absorption resonances and actually crosses the bare metamaterial structural resonance.

Now, when we are finished with the design of the experiment we can discuss the fabrication process.

2.4.2 Fabrication of the experimental samples

A set of 7 samples were made using standard lithographical and cleanroom processing to completely cover the wavelengths of interest. We would like to give credit and acknowledge a great help from the Gregory Ten Eyck [10], who put in a lot of time and hard work in successful processing of those samples. Process of the sample production involved several steps and is described below.

It starts with deposition of the Al film on the top of BaF₂ substrate using E-Beam evaporator, than BCB material was deposited by spin-on technique and then capped by the Al layer as it is demonstrated in the Figure 2.16 on the left. Hard oxide (SiO₂) mask was deposited using PECVD method on top of the last Al layer, followed by the layer of Photoresist (PR).

Standard optical lithography process using MJB-3 stepper tool was used to define pattern in the PR layer. Final structure with the defined pattenr is shown in the Figure 2.16 on the right.

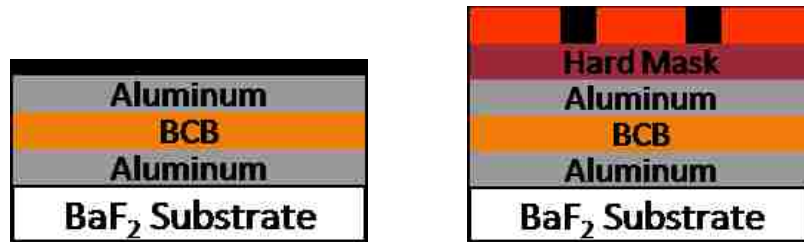


Fig. 2.16 3 layer deposition on the substrate to create base for the fishnet metamaterial (left); hard oxide (SiO₂) mask and PR layer with defined structure atop bulk base (right).

Defined in the PR layer pattern was transferred in the hard mask. Than Cl₂ based ICP-RIE aluminum etch was performed to the top metal followed by CF₄/O₂ RIE BCB etch and another Cl₂ based etch for bottom metal layer were used to transfer our designed pattern through all 3 layer at it shown in the Figure 2.17 on the left. Final step in production of our fishnet metamaterial structure was a removal of a hard mask, shown in the Figure. 2.17 on the right.

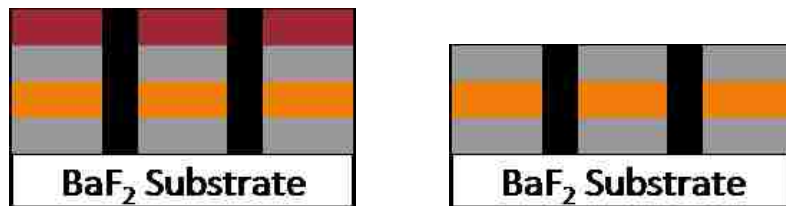


Fig. 2.17 Fishnet pattern defined in the hard mask and transferred in the 3 layered metamaterial structure using 3 consecutive gas based etches (left); Final step where the hard mask is removed and finished fishnet metamaterial structure on BaF₂ substrate is obtained (right).

Pattern transferring process described above, was applied to a single 2 inch BaF₂ wafer at ones, where 7 samples were lithographically defined. This way the homogeneity of the manufacturing process and uniformity of the final samples were insured.

2.4.3 Experimental results

Fourier transform infrared spectroscopy (FTIR) measurements were performed to obtain, normalized to a bare BaF₂ substrate, transmission spectra for each individual sample. The effective refractive index has not yet been extracted because only transmission spectra have been obtained. Once reflection and phase information are obtained, the behavior of effective n can be evaluated. An optical microscope image evaluation was carried along with the FTIR measurements. An important point that needs to be noted is that after the litho and cleanroom processing the final sample linewidths have deviated from it targeted values. In order to address this change we measured the experimental sample linewidths and plug them back in our DOE model and now we are comparing the results of the FTIR scan with adjusted transmission and effective refractive index responses of the fishnet metamaterial.

Figure 2.18 shows Namarski microscope images of the processed samples with the metamaterial structural resonance (MSR) at 7.4-, 8.2- and 8.6- μm .

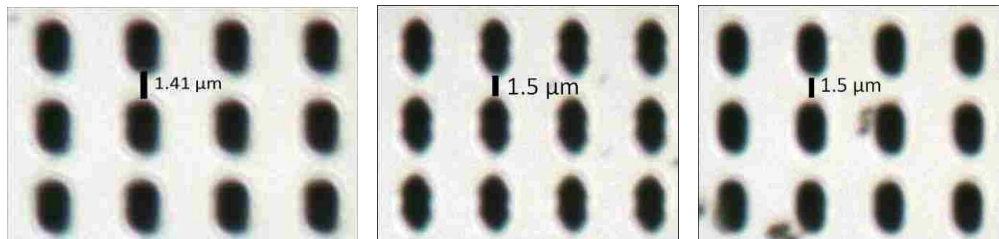
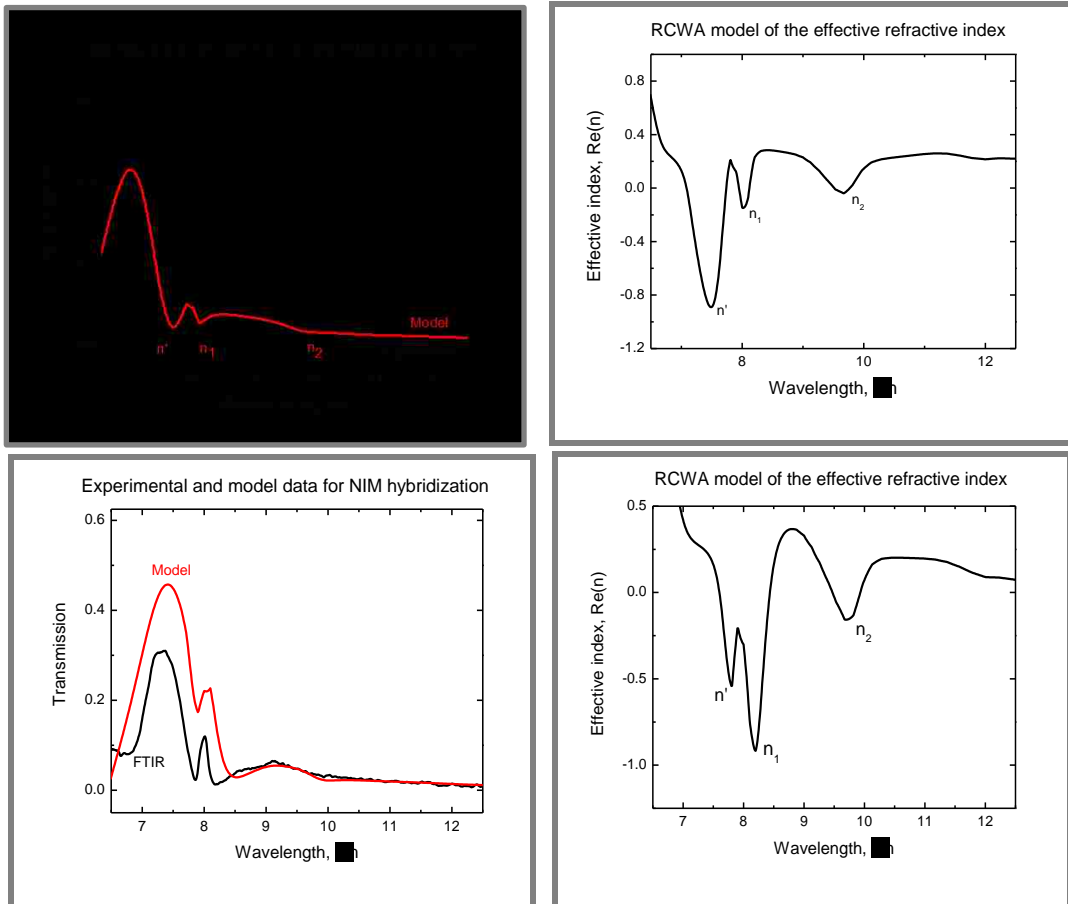


Fig.2.18 Namarski microscope images of the processed samples **Left:** MSR at 7.4 μm ; **Middle:** MSR at 8.2 μm ; **Right:** MSR at 8.8 μm .

As we see all samples show very good overall uniformity and successful pattern transfer follow by the post lithographical cleanroom process.

In the Figure 2.19 a set of overlapped experimental and model transmission curves along with corresponding RCWA modelled effective refractive index curves are demonstrated, for the samples with bare structural resonance approaching and then crossing first BCB absorption peak.



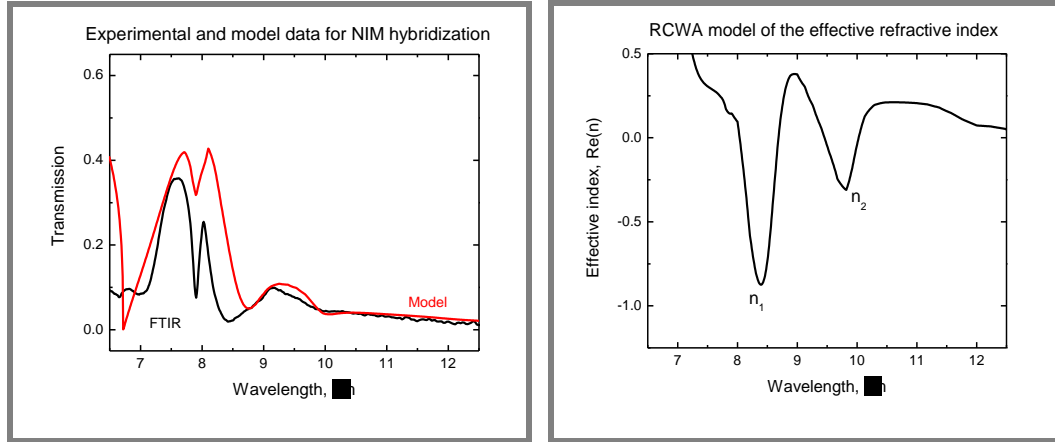


Fig. 2.19 Overlapped experimental (FTIR) and modelled transmission curves (left); RCWA model for the corresponding effective refractive index (right). Hybridized resonances n' , n_1 and n_2 are indicated on the graphs. **Top:** Metamaterial structural resonance (MSR) is at 7.4 μm (0.167 eV); **Middle:** Metamaterial structural resonance (MSR) is at 8.2 μm (0.151 eV); **Bottom:** Metamaterial structural resonance (MSR) is at 8.6 μm (0.144 eV).

Three resonance dips are distinguishable in the Figures 2.19, top and middle plots, as a bare structural metamaterial resonance is approaching (at 7.4 μm) and crossing (8.2 μm) the first BCB absorption peak (at 7.9 μm) and they are marked as n' , n_1 and n_2 on the plots. As it was predicted by our model results when the bare structural resonance moves towards the stronger, second, BCB absorption peak (at 9.5 μm) it became dominant and only 2 hybridized resonance dips are observed in the Figure 2.19 bottom plot. First BCB absorption peak now have a small effect and shows itself as an intensity dip in the transmission curve at $\sim 8.0 \mu\text{m}$. Experimental FTIR data shows a very good qualitative agreement with the RCWA model.

Next Figure 2.20 shows Namarski microscope images for the samples where bare structural resonances moves towards and then crosses the second BCB absorption peak.

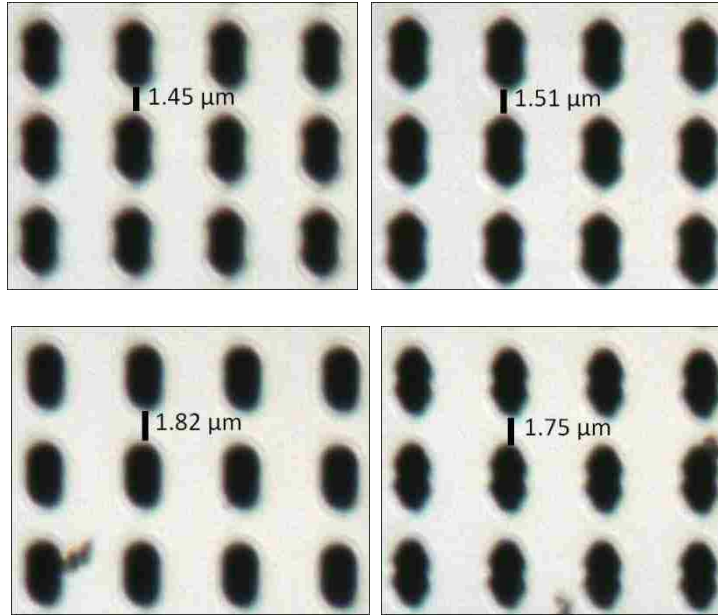


Fig. 24.20 Namarski optical microscope images for samples with:
Top row: left – MSR at 8.9 μm (0.139 eV); right – MSR at 9.4 μm (0.132 eV)
Bottom row: left – MSR at 9.9 μm (0.125 eV); right – MSR at 10.3 μm (0.12 eV).

All samples show very good uniformity and high quality of the lithography and cleanroom patter transfer processes.

Next few plots in the Figure 2.21 demonstrate hybridization effect when a bare structural metamaterial resonance moves towards the second, dominant BCB absorption peak at 9.5 μm . Since this peak is much stronger than the first one at 7.9 μm we observe only 2 hybridized resonance dips. This follows the same trend that was discovered during our initial modeling. The weaker, first BCB absorption resonance peak at 7.9 μm (0.157 eV) has a small effect, which manifests itself in the form of a dip in the transmission and effective refractive index curves at the location of the resonance.

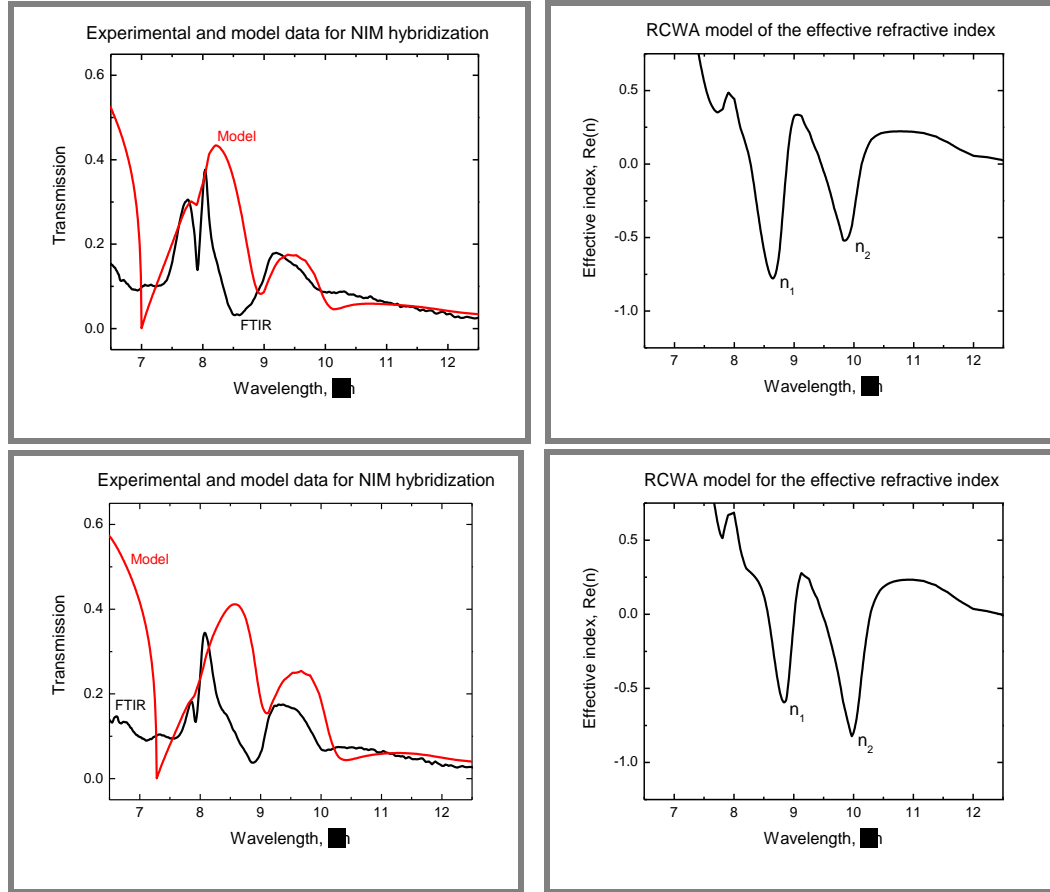


Fig. 2.21 Overlapped experimental (FTIR) and modelled transmission curves (left), and RCWA model for the corresponding effective refractive index (right). Hybridized resonances n_1 and n_2 are indicated on the graphs. **Top:** Metamaterial structural resonance (MSR) is at 8.9 μm (0.139 eV). **Bottom:** Metamaterial structural resonance (MSR) is at 9.4 μm (0.132 eV).

Figure 2.22 shows fishnet metamaterial response as bare structural resonance crosses the second BCB absorption peak.

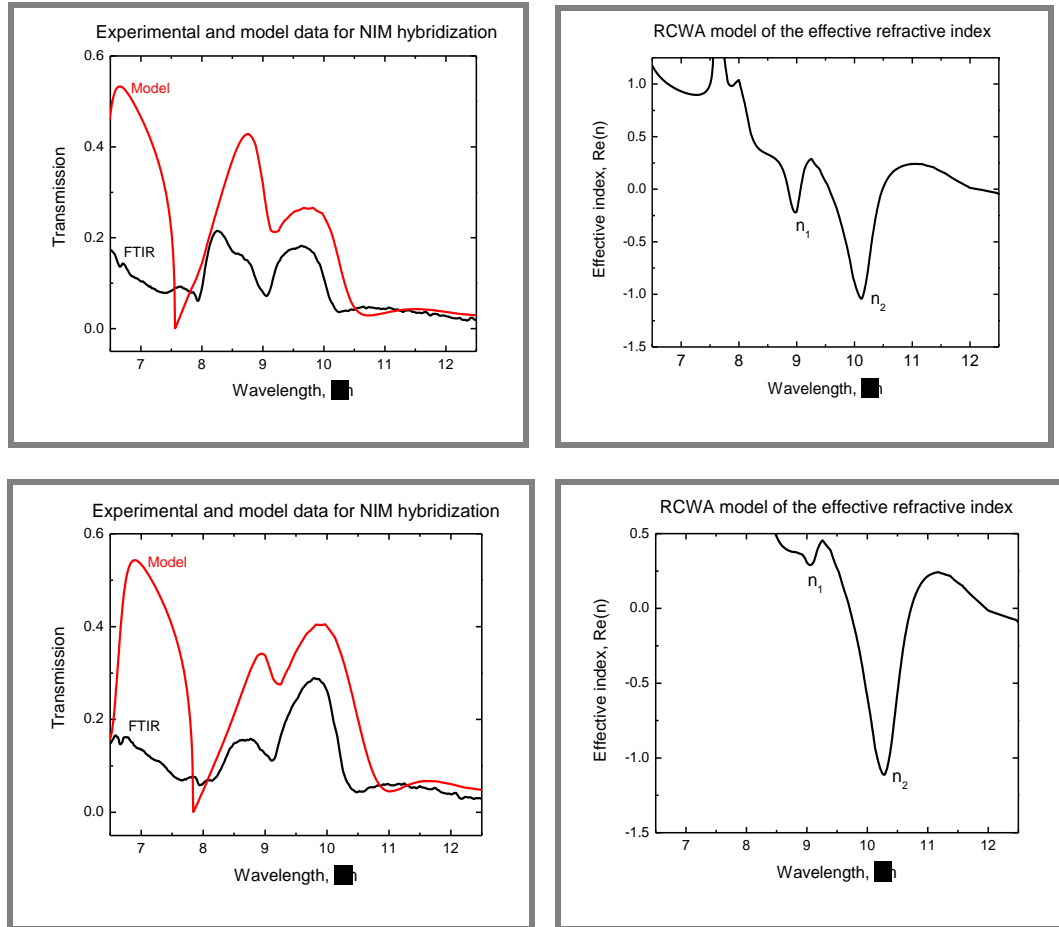


Fig. 2.22 Overlapped experimental (FTIR) and modelled transmission curves (left), and RCWA model for the corresponding effective refractive index (right). Hybridized resonances n_1 and n_2 are indicated on the graphs. **Top:** Metamaterial structural resonance (MSR) is at $9.9 \mu\text{m}$ (0.125 eV). **Bottom:** Metamaterial structural resonance (MSR) is at $10.3 \mu\text{m}$ (0.12 eV)

All represented above samples show good qualitative agreement between the model and experimentally obtained data.

Close study of the RCWA model behaviour of the effective refractive index reveals sharing of the oscillator strength, shown in the Figure 2.23, as the bare fishnet metamaterial resonance is tuned through the absorber resonances.

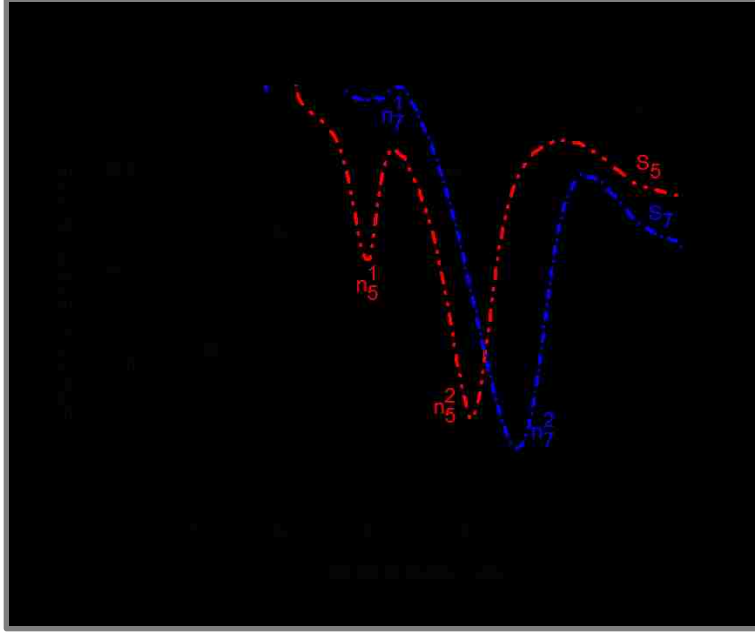


Fig. 2.23 RCWA modeled sharing of the oscillator strength in the effective refractive index as the bare fishnet metamaterial resonance is tuned through the absorber resonances. Demonstrated refractive index responses are from the samples with: (1) MSR at $7.4 \mu\text{m}$ (0.167 eV), black curve; (5) MSR at $9.4 \mu\text{m}$ (0.132 eV), red curve and (7) MSR at $10.3 \mu\text{m}$ (0.12 eV). Resonances n_*^1 and n_*^2 are sharing their strength.

Figure 2.24 combines experimental and simulated results that highlight classical anti-crossing behaviour of resonances. The experimental and numerical model data are in very good qualitative agreement.

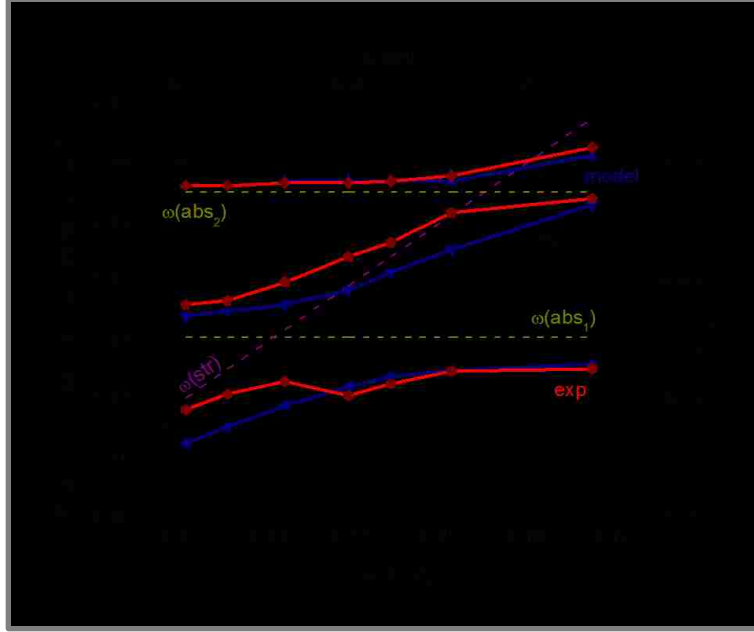


Fig. 2.24. Numerical RCWA model (blue) and experimental data (red) demonstrates the classical anti-crossing behavior of the fishnet structure with a BCB absorber, with two dipole resonances at $7.9 \mu\text{m}$ (0.157 eV) and $9.5 \mu\text{m}$ (0.13 eV) in the dielectric material. Resonant frequencies of the fishnet structure are tuned through the electric dipole resonances of the bare absorber. Hybridization and an anti-crossing behavior are clearly visible in both experimental and model data with good agreement.

We note that in the final plot first resonance point at $\sim 0.168 \text{ eV}$ in the high frequency branch occurs on the wrong side of the structural resonance curve. During our DOE this first point was located higher in frequency though above the bare structural resonance, however the adjusted model and FTIR data shows this pint below.

Currently, work for obtaining the reflectivity response from the experimental samples is being performed. This will allow estimating the losses present in the samples and possible give an idea to future improvements.

2.5 Conclusions

We have experimentally and numerically demonstrated a novel resonance hybridization effect between metamaterial and dielectric absorption resonances. A simple physical model, more detailed RCWA calculations and experimental data all clearly show

coupling between the resonances with hybridization behavior and sharing of oscillator strength. There is a good qualitative agreement between the RCWA model calculations and experimental data. This effect is of interest for sensors and other optical applications at infrared frequencies and can be potentially extended to different wavelengths.

This work was done with the collaboration with the Center for Integrated Nanotechnologies (CINT) at Sandia National Laboratories (SNL) who manufactured the experimental sample and the Center for High Technology Materials (CHTM) at University of New Mexico (UNM) who designed the sample structure and performed modeling and FTIR measurements.

2.6 References

- 1 S. Zhang, W. Fan, K. J. Malloy, S. R. J. Brueck, N. C. Panoiu and R. M. Osgood, *Opt. Express* vol.13, pp. 4922, 2005.
- 2 S. O'Brien, D. McPeake, S. A. Ramakrishna, and J. B. Pendry, Near-infrared photonic band gap and nonlinear effects in negative magnetic metamaterials, *Phys. Rev. B*, vol. 69, art. 241101, 2004.
- 3 S O'Brien and J B Pendry, Magnetic activity at infrared frequencies in structured metallic photonic crystals, *J. Phys.: Condens. Matter* **14**, 6383 (2002).
- 4 Kittel, Charles, *Quantum theory of solids*, New York : Wiley, (1987)
- 5 M. G. Moharam and T.K. Gaylord, Rigorous coupled-wave analysis of planar-grating diffraction, *J. Opt. Soc. Amer.* vol. 71, pp. 811, 1981.
- 6 B. K. Minhas, W. Fan, K. Agi, S. R. J. Brueck and K. J. Malloy, Metallic Inductive and Capacitive Grids: Theory and Experiment, *J. Opt. Soc. Amer.* vol. 19, pp. 1352, 2002.
- 7 D. R. Smith and S. Schultz, Determination of effective permittivity and permeability of metamaterials from reflection and transmission coefficients, *Phys. Rev. B*, vol. 65, art. 195111, 2002.
- 8 J. B. Pendry, A. J. Holden, D. J. Robbins, and W. J. Stewart "Magnetism from Conductors and Enhanced Nonlinear Phenomena" *IEEE Trans. on Microwave Theory and Tech.*, **47**, 2075 (1999).
- 9 Courtesy for characterization of BCB material by G. Bormann.
- 10 Ten Eyck, Gregory A, gateney@sandia.gov, Sandia National Labs.

Chapter 3 Imaging Interferometric Lithography: Demonstration of $\sim \lambda/(3NA)$ Half-Pitch Features By 244-nm, 0.9 NA Optical Test Bed

3.1 Introduction

The increasing demands of the microelectronics industry have led to steady improvement in semiconductor manufacturing technology and pattern definition (lithography) and transfer capabilities. Moore's law [1,2] is the guideline that predicts, and therefore drives, remarkable advances in manufacturing technology. The National Technology Roadmap for Semiconductors, developed by the Semiconductor Industry Association (SIA), serves as the industry standard version of Moore's Law [3].

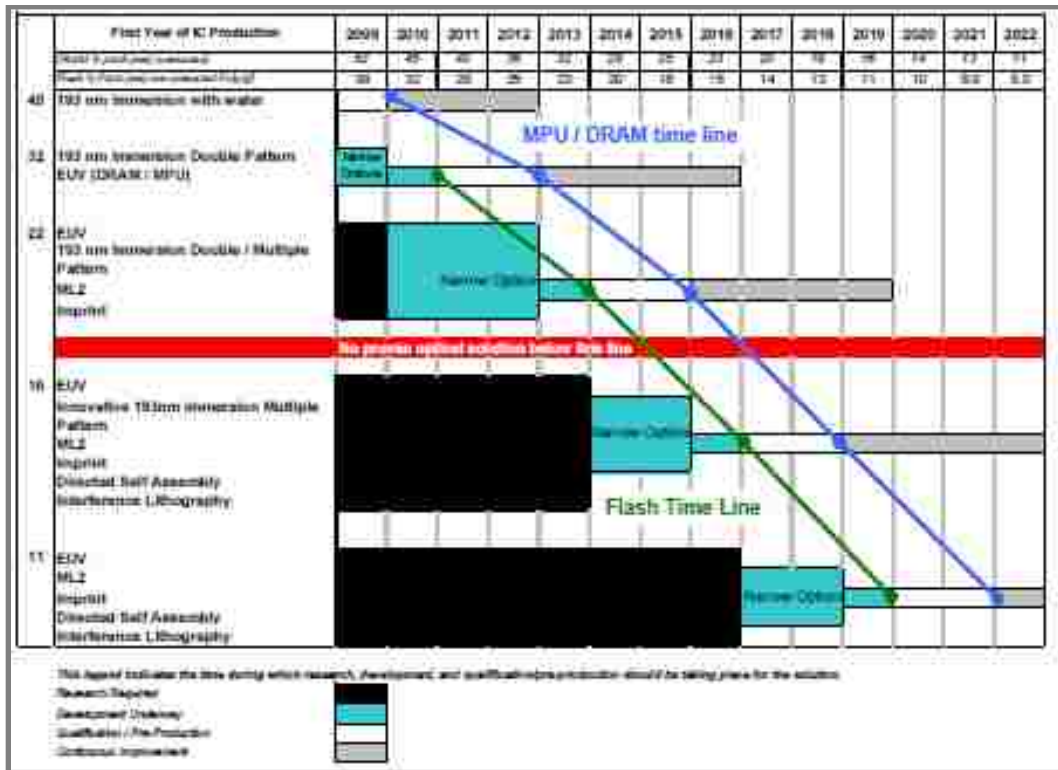


Fig. 3.1 National Technology Roadmap demonstrates lithography exposure tools potential solutions for achieving desired half-pitch nodes as of 2009.

The 2009 roadmap, shown in Figure 3.1 provides potential solutions for achieving desired half-pitch nodes in 1 year periods. The manufacturable solution for the 65-nm technology node was in mass production in year 2007 with continuous development through 2010. Current map shows that manufacturing solution for the 45-nm node was developed for the mass production by the year 2009 and currently it is in the qualification-pre production stage with continuous development through 2012. Right now the manufacturable solution for the 32-nm technology node is in the development stage using the 193 nm immersion and double patterning technology. It will be required to enter the pre-production stage by the end of 2010. Active process development for the 22-nm technology node is taking place right now and according to the map will continue until year 2014. A decision on lithographic technology for these nodes is needed in the near future to allow sufficient time for process development.

Optical lithography is expected to be the dominant approach through DRAM 22 nm half pitch, along with EUV and maskless approaches. Nanoimprint lithography possibly appears at a 22-nm half pitch. Combination of the immersion lithography and double or possible triple patterning techniques could extend optical lithography to the 11 nm half-pitch node. Y. Borodovsky has announced in 2009 at SEMICON West, that Intel[®] plans on using 193 nm immersion with pitch division as a viable option for 11 nm node patterning in 2015 [4]. Current research is actively ongoing into spatial frequency doubling (interpolation) schemes that involve dividing the pattern into two masks, with each exposure at twice the final pattern minimum half-pitch [5-7]; double patterning that involves some intermediate step between the exposures and mentioned earlier pitch division technique. It is important to understand that the approach, where multiple

exposures are combined, offers much promise but requires extremely tight overlay control. The drop in defectivity for these double-patterning and double-resist systems must exceed the drop for single-patterning systems, because the extra process steps are already a process throughput inhibitor, which is a very critical factor for the industry mass production. Alternative manufacturing solutions such as extreme ultra violet (EUV), Nanoimprint and direct self assembly are being developed to meet the requirements for the 7 nm node.

A industry approach constantly has been that death of optical lithography from emerging technologies will come within next two generations. However if we look at the history, optical lithography seems to prolong its life again and again, and still being the dominant lithographical technology capable of meeting new challenges. Significant extensions of optical lithography was achieved by using liquid immersion lithography [8] that allows an increase in the resolution of up to a factor of the liquid refractive index ($n_{H_2O} = 1.44$ at 193 nm) [9]. Combinations of the liquid immersion and double patterning techniques opened another door in the future for the optical lithography. Therefore it is very important to investigate the *ultimate resolution capabilities of optical lithography* and to investigate imaging techniques that offer practical approaches to reaching those ultimate limits. At the same time, mask costs are becoming the dominant factors in cost of ownership evaluations as a result of the demands of resolution enhancement techniques (RETs) such as optical proximity correction and phase shift masks. Currently cost of a mask set for the Intel[®] microprocessor runs as high as 1 – 2 million of dollars, and a single litho tool can cost as much as 40 millions. As always, the adoption of a new

lithography concept in manufacturing is contingent on cost of ownership issues and competition from other evolving technologies.

In order to meet demanding requirements for the lithography tools and investigate the ultimate resolution capabilities of optical lithography we propose the use of Interferometric lithography (IL), that provides a simple technique allowing access to features approaching the resolution limits of optics [10 , 11] with integration of conventional optical lithography [12, 13]. Such combination will offer an optics-based lithographic capability for at least the 45-nm half-pitch generation [14], that is roughly equivalent to the industry 32 nm microprocessor node (1:2 duty cycle) and at the same time offers a significant advantage in cost of ownership since it can be used with a much less involved mask-based RET strategies.

3.2 Nanofabrication techniques

3.2.1 Interferometric Lithography (IL)

The minimum half-pitch feature interferometric lithography can access is given by the well-known equation, $\lambda_{\text{eff}} = \lambda / (2n \sin \theta)$, where λ is the exposure wavelength, n is the refractive index of the immersion medium and the two beams propagate at angles of $\pm\theta$ with respect to the wafer surface normal. Figure 3.2 shows an example of a simple interferometric lithography setup.

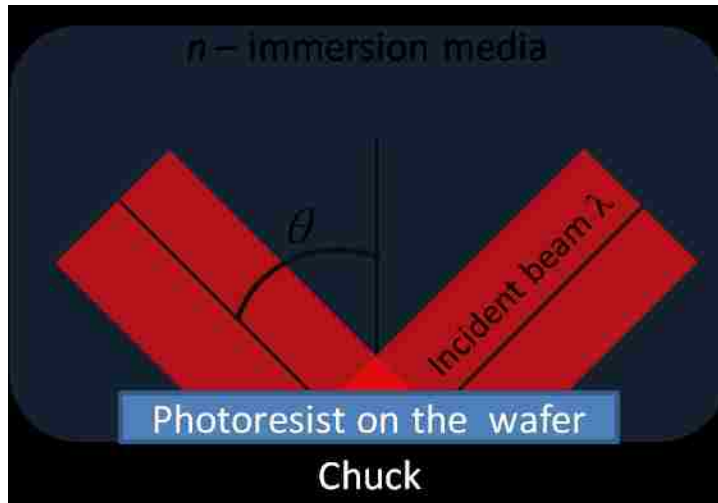


Fig. 3.2 Example of simple interferometric lithography setup, where minimum accessible half-pitch feature is $\lambda/4n \sin \theta$

Two interfering coherent optical beams of the same polarization create a sinusoidal aerial image in the photoresist (PR) layer that can be described as:

$$1 + \cos (2\pi nx/d) \quad (3.1)$$

Figure 3.3 shows graphical representation of the intensity distribution for the aerial image and corresponding frequency space distribution.

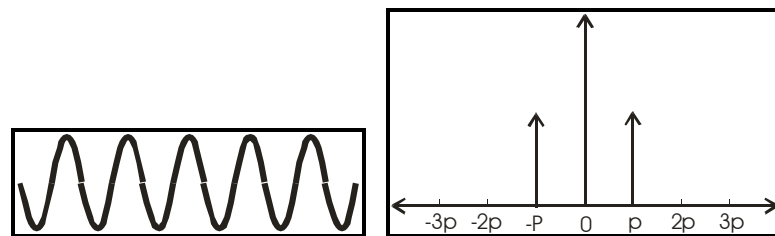


Fig. 3.3 Sinusoidal intensity distribution for the aerial image (left) and corresponding frequency space distribution (right).

Highly nonlinear chemical processes that take place in the photoresist can turn this sinusoidal aerial image in the developed pattern that can be described as:

$$\frac{n^2 a/d}{2n} \cos^2 \left(\frac{2\pi nx}{d} \right) \quad (3.2)$$

Figure 3.4 shows developed pattern and its frequency space distribution.

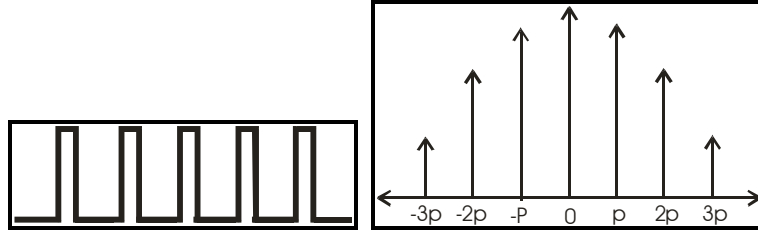


Fig. 3.4 Developed pattern profile (left) and its frequency space distribution (right).

It is important to note that this chemical nonlinear process can only reduce the linewidth and sharpen sidewall but *do not add new structures to the aerial image and a developed pattern*. So it is sole up to the optical system to provide the maximum resolution and successful aerial image transfer to the photoresist layer.

A simple Imaging Lithography (IL) setup, as shown in the Figure 3.5 can be constructed to evaluate resolution prosperities of the photoresist (PR), quality of the beam and to establish experimental procedure.

For Argon Ion frequency doubled CW laser ($\lambda = 244 \text{ nm}$), air ($n = 1.0$) as an immersion medium and an $NA = n \times (\sin\theta)$ of 0.9, the minimum accessible pitch is $\sim 122 \text{ nm}$, that corresponds to half-pitch or a Critical Dimension (CD) of 61 nm. The laser output beam is expanded and collimated prior to entering the experimental setup. The first optical element of the setup is a 50/50 ration (transmitted/reflected) beam splitter which divides incident beam in the two parts with the equal intensities. Retaining equal intensities in the two arms of the setup is important if we want to have a highest possible contrast in the final aerial image. Each arm of the beam is then reflected by the mirror. Position and angle of those mirrors determines the angle θ at which two arms of the beam is then interfere in the PR layer and produces final aerial image.

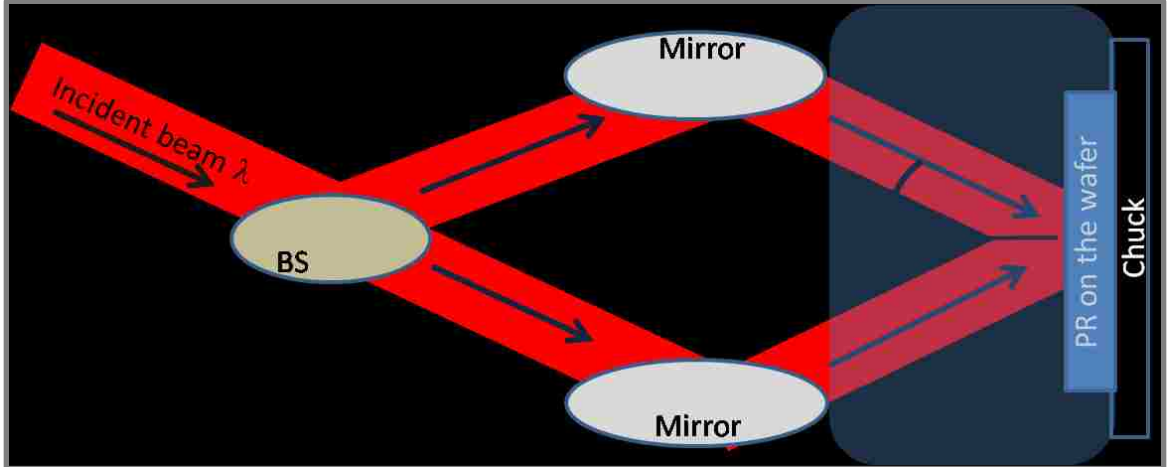


Fig. 3.5. Experimental IL setup constructed to evaluate resolution properties of the PR and establish experimental procedure.

Series of experimental samples were produced during this evaluation. Details about sample preparation, PR and sample development can be found in this chapter in subsections 3.4.1 and 3.4.2.

Positive type, UV photoresist - UV 210-0.3, manufactured by Rohm and Haas [15] was used for this experiment along with 248 nm antireflection coating (ARC) DUV-112 [16]. Once exposed sample was developed it was examined using a Scanning Electron Microscope (SEM). The following set of SEM pictures of PR pattern on the silicon wafer with different pitches 300 – and 200 - nm demonstrate the result of IL experiment.

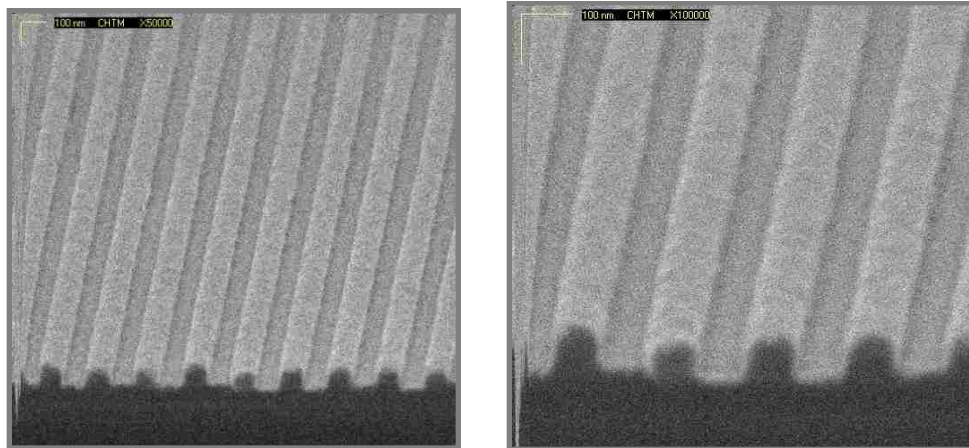


Fig. 3.6 SEM micrograph of the PR pattern on the top of the silicon wafer with Pitch of ~ 300 nm.

In this case exposure dose was selected in such a way that resulting CD is approximately half of the pitch. If we increase the exposure dose then we can shrink the resulting CD, but the pitch will stay the same as it is showing of the Figure 3.7.

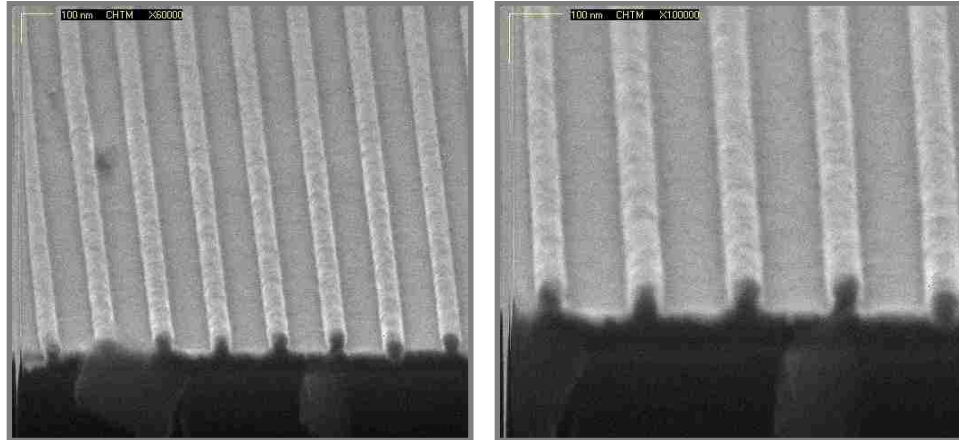


Fig. 3.7 SEM micrograph of the PR pattern on the top of the silicon wafer. Pitch ~ 300 nm, CD is $\sim 1/3$ P.

Next few figures shows SEM micrographs of the PR patterns with ~ 200 nm pitch.

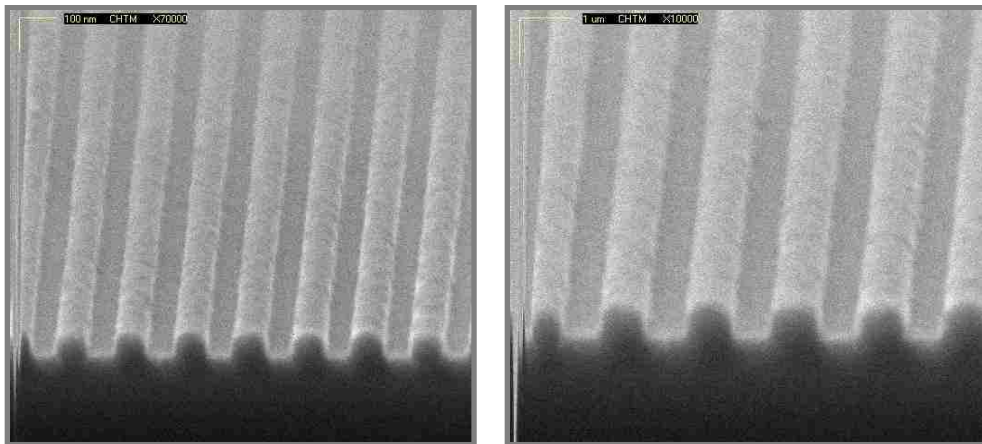


Fig. 3.8 SEM micrograph of the PR pattern on the top of the silicon wafer with Pitch of ~ 200 nm.

And as we did it in the previous case, if the exposure dose is increased, the final CD can be reduced to $\sim 1/4$ of the pitch. That is shown on the Figure 3.9.

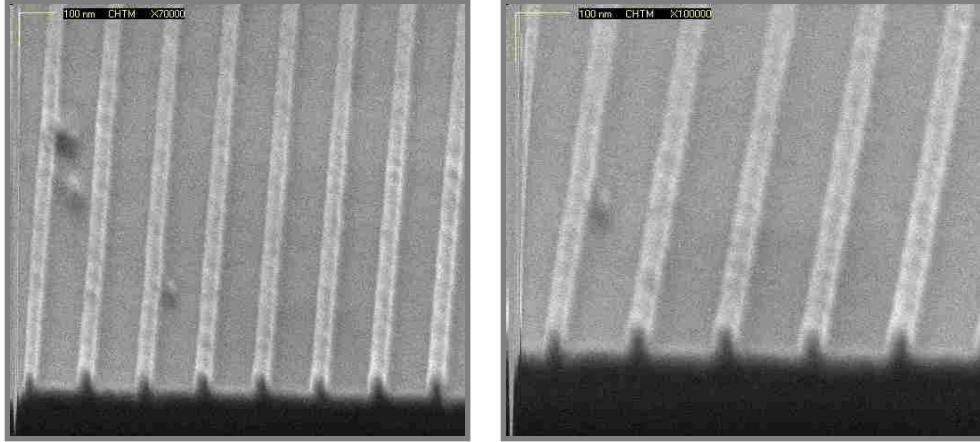


Fig. 3.9 SEM micrograph of the PR pattern on the top of the silicon wafer. Pitch ~ 200 nm, CD is $\sim 1/4$ P.

We have demonstrated a fabrication of the periodic line pattern in the PR by the means of the IL. Simple experimental setup that provides us with the control over the incident angle θ also provides us with the control over the pitch on the final pattern. Exposure dose variations as well as the variations in the post-processing can give us the tool to control CD's of the pattern. During this experiment estimation of the PR resolution limits was performed. We have demonstrated that current PR (UV-210) can successfully resolve periodic patterns with the pitch of ~ 200 nm and CD of ~ 50 nm.

However there is a difference in printing periodic and arbitrary pattern. An array of periodic patterns (lines and spaces) produces the Fourier transform of the energy distribution in the form of discrete points of light, or the diffraction orders, of the finite width. For the multiple spaces and lines diffraction patterns from adjacent spaces interfere with each other, producing narrow interference fringes. The greater the number of line/spaces the narrower the peaks. In order to successfully print this dense structure one should capture the zero order and one of the first orders within the optical system and then recombine them. On the other hand for the isolated line or space Fourier transform results in a continuous distribution of energy in the form of the sinc function. So, for the successful printing of the isolated line one should capture that whole distribution within

the optical system. Should some part of this distribution be missed that will lead to significant degradation of the printed image. Usually printing of the single isolated line is the most hardest and challenging task for the lithography. For some arbitrary pattern Fourier distribution will generally have a more complicated form where higher and low order frequencies will have side bands. Successful pattern transfer will require capture of those bands within the optical system. This can be done by combining IL with conventional optical lithography and creating Imaging Interferometric Lithography (IIL) tool.

3.2.2 IIL - Imaging interferometric lithography

3.2.2.1 Introduction, theory and previous work

Imaging Interferometric Lithography, using off-axis illumination at the limits of the pupil along with pupil-plane filters, to ensure uniform frequency-space coverage, is a relatively new imaging concept that provides an approach to accessing the fundamental linear system resolution limits of optics [12]. IIL eases many of the constraints that limit the capabilities of conventional optical lithography and offers a path to extend the ultimate linear systems of optics to dense (pattern dependent) CDs of $\sim \lambda/3NA$ ($NA=n \sin\theta$ for immersion) for arbitrary patterns. Significant benefits of IIL, especially for high- NA optics, include the ability to optimize the polarization for the highest spatial frequencies, and to vary relative intensities and contrast of the multiple images separately in the x - and y -directions for 2D mask patterns.

IIL was first introduced [11,17] as a technique to cover the extremes of frequency space by tilting the illumination as far as possible off-axis. For the low NA 's ($NA \sim$

0.3÷0.6) in order to cover the extremes of frequency space, zero order was send around the lens and reintroduce on the image side. For the high NA lenses ($NA = 0.9$) this was no longer necessary and the zero and high frequency orders were passed through the lens. We can interpret off-axis illumination scheme in some general mathematical terms.

The field distribution after the mask can be written using summations, following Goodman and Mack [18, 19], one for each direction (x, y) perpendicular to the propagation direction (z) :

$$U_y(x, y) = \left[\sum_{f_x} \sum_{f_y} A(f_x, f_y) e^{i2\pi f_x x} e^{i2\pi f_y y} \right] \quad (3.3)$$

Where $A(f_x, f_y)$ are the Fourier coefficients of the mask. Introducing a y-off-axis illumination, for example, we will shift the frequencies of the y – direction by $f_{off} = f_{y,off} = \sin(\varphi_y) / \lambda$. So that we have:

$$U_y(x, y) = \left[\sum_{f_x} \sum_{f_y} A(f_x, f_y) e^{i2\pi f_x x} e^{i2\pi(f_y - f_{off})y} \right] \quad (3.4)$$

Transmission trough an optical system will introduce the pupil function P that acts as a transfer function of the field:

$$T_c(f_x, f_y) = P(f_x, f_y) = \begin{cases} 1, & f < f_{opt} \\ 0, & f \geq f_{opt} \end{cases} \quad f = \sqrt{f_x^2 + f_y^2} \quad (3.5)$$

Where $f_{opt} = NA/\lambda$. The frequencies are shifted by the off-axis illumination, so we have:

$$U_y(x, y) = \left[\sum_{f_x} \sum_{f_y} T_c(f_x, f_y - f_{off}) A(f_x, f_y) e^{i2\pi f_x x} e^{i2\pi(f_y - f_{off})y} \right] \quad (3.6)$$

Separating out the zero order term will give us:

$$\begin{aligned}
U_y(x, y) = & A_{00}e^{-i2\pi f_{off}} \\
& + \left[\sum_{f_x \neq 0} \sum_{f_y \neq 0} T_c(f_x, f_y - f_{off}) A(f_x, f_y) e^{i2\pi f_x x} e^{i2\pi(f_y - f_{off})y} \right] \quad (3.7)
\end{aligned}$$

After the field has passed the optical system the square law response for the intensity will produce the following image:

$$\begin{aligned}
I_y(x, y) \sim & |U_y(x, y)|^2 = \\
& A_{00} \sum_{f_x \neq 0} \sum_{f_y \neq 0} A(f_x, f_y) T_c(f_x, f_y - \\
& f_{off}) e^{i2\pi f_x x} e^{i2\pi(f_y - f_{off})y} + A_{00}^* \sum_{f_x \neq 0} \sum_{f_y \neq 0} A^*(f_x, f_y) T_c(f_x, f_y - \\
& f_{off}) e^{-i2\pi f_x x} e^{-i2\pi(f_y - f_{off})y} + |A_{00}|^2 + \\
& \sum_{f_x \neq 0} \sum_{f_y \neq 0} [\sum_{f'_x \neq 0} \sum_{f'_y \neq 0} A(f_x, f_y) T_c(f_x, f_y - \\
& f_{off}) A^*(f'_x, f'_y) T_c(f'_x, f'_y - f_{off}) e^{i2\pi(f_x - f'_x)x} e^{i2\pi(f_y - f'_y)y}] \quad (3.8)
\end{aligned}$$

We recognize that the first term in this equation is proportional to the Fourier series of the original object (eqn. 3.3) restricted by the amplitude transfer function. This is an important result, since it tells us that the zero frequency term A_{00} can recover the original distribution. This fact is the central for IIL. The second term is the complex conjugate of the first and makes sure that we have with the first one the real quantity as needed for an intensity distribution. The square law response “recovers” these terms. The first two terms are also referred to as a linear terms. The third term is the intensity if the zero order and adds a constant base line to the result. Finally the “cross-correlation” of quadratic terms adds low spatial frequency information.

Graphically off-axis illumination scheme can be visualized as it is shown on the Figure 3.10.

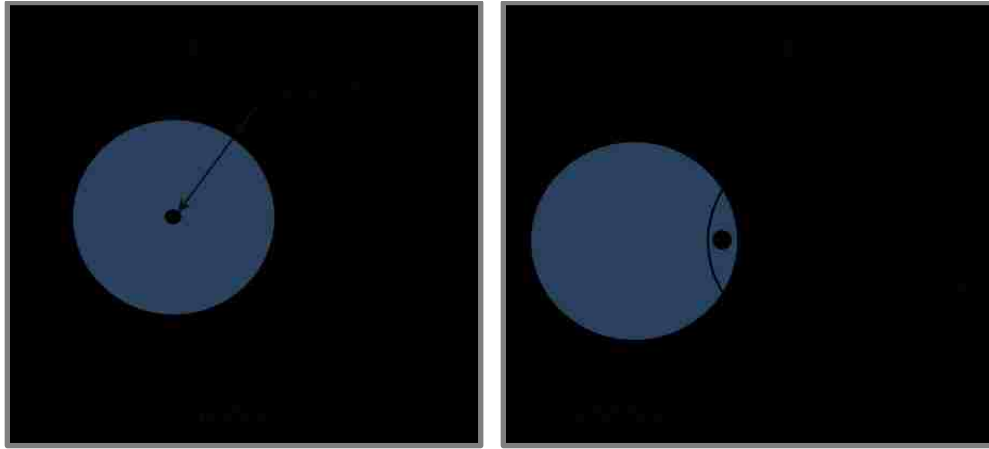


Fig. 3.10 On-axis illumination scheme (left) and off-axis illumination scheme were zero order is retained in the optical system (right). With the off-axis illumination frequency space coverage can be practically doubled.

The first experiments showed a successful result for a 2- μm CD using coherent source of $\lambda=364$ nm and $NA=0.04$ equivalent to a Rayleigh k_1 of 0.22 [20]. Here Rayleigh resolution criteria is $CD \sim k_1 \lambda / NA$. It states that the printed CD is lineary proportional to the wavelength and inversely proportional to the NA . Defined in this way the factor k_1 becomes a measure for the combined quality of the lithographic process including optical as well as photoresist process conditions.

Since we mention that for the first experimental demonstration a coherent source of illumination was used it is logical to give brief introduction to coherent and incoherent illumination schemes generally used in the lithography.

One of the pioneers of the coherent imaging theory was Abbe [21].For the coherent illumination case, we look at the field amplitudes. The convolution between the object field distribution and the point spread function will give us the field distribution in the image plane. For this case we can write

$$U_i(u, v) = \int \int_{-\infty}^{\infty} h(u - \xi, v - \eta) U_g(\xi, \eta) d\xi d\eta \quad (3.9)$$

where U_i is the image plane distribution and the U_g is the object field distribution. The impulse response of amplitude point spread function, h , is the Fraunhofer diffraction pattern of the exit pupil given by the pupil function $P(x, y)$ that is 1 inside the pupil and 0 outside.

$$h(u, v) = \frac{A}{\lambda z_i} \int \int_{-\infty}^{+\infty} P(x, y) \exp \left\{ -j \frac{2\pi}{\lambda z_i} (ux + vy) \right\} dx dy \quad (3.10)$$

A is a constant amplitude; z_i is the distance from the exit pupil to the image plane. A coherent optical system, that has no geometrical aberrations and is translation invariant can be described in this way and is called diffraction limited. Because of the convolution theorem we have:

$$U_i = h \otimes U \Leftrightarrow F\{U_i\} = F\{h\}F\{U_g\} \quad (3.11)$$

For the transfer function $H_{coh}(f_x, f_y)$, defined as the Fourier transformation of the impulse response $h(u, v)$ we get the pupil function:

$$F\{h(u, v)\} = H_{coh}(f_x, f_y) = P(\lambda z_i f_x, \lambda z_i f_y) \quad (3.12)$$

This important result tells us that in the coherent case, we have the pupil function as the amplitude transfer function (AFT), which means that there is a hard frequency cut-off due to the aperture of the optical system. The aperture of the optical system of the diffraction plane can be constricted simply as the geometrical projection of the spherical entrance pupil into a plane. Thus, one can express the spatial frequency in terms of the angle of diffraction $f_x = nx'/\lambda z = n \sin \theta_x / \lambda$. The cut off frequency can be generalized for the on-axis illumination as:

$$f_{coh,max} = \frac{NA}{\lambda} \equiv f_{opt} \quad (3.13)$$

This can be represented graphically as it shown of the Figure 3.11.

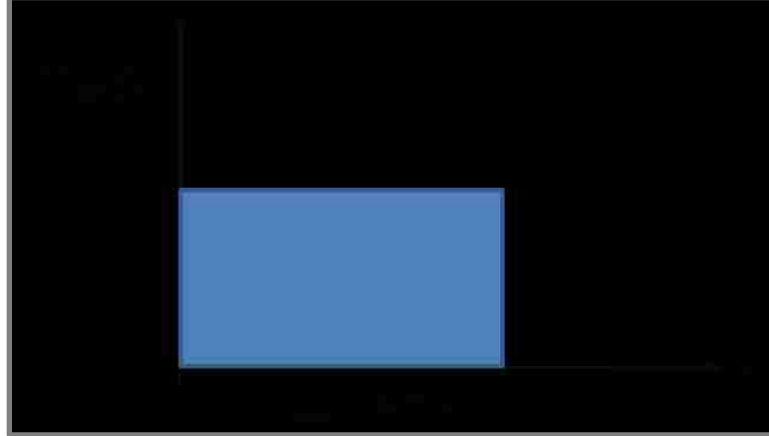


Fig. 3.11 This is an amplitude transfer function (ATF) for coherent illumination. The x-axis represents spatial frequency of the field distribution.

As the size of the illumination source becomes larger relative to the size of the pupil, the illumination is said to be spatially incoherent. For this case we can use Hopkins [22] approach for the partially coherent case and simplify the integration over the source, where Transmission Cross Coefficient (TCC) becomes:

$$\begin{aligned} TCC(f_x, f_x^{\sim}) &\propto \int_{-\infty}^{\infty} P(f_x + f'_x) P^*(f_x^{\sim} - f'_x) df'_x \\ &= \int_{-\infty}^{\infty} P(f'_x) P^*(f_x^{\sim} - f_x + f'_x) df'_x \end{aligned} \quad (3.14)$$

As the final form of this Eqn.3.14 indicates, the TCC will only be a function of the difference in the spatial frequencies $f_x^{\sim} - f_x$. Thus:

$$TCC(f_x^{\sim} - f_x) \propto P(f_x) \otimes P^*(f_x) \quad (3.15)$$

where the proportionality is made into an equality through proper normalization. For the incoherent case the TCC is called the optical transfer function (OTF) . The magnitude of

the OTF is called the modulation transfer function (MTF). For an ideal circular pupil, this convolution can be easily carried out [19] giving:

$$MTF(f) = \frac{2}{\pi} \left[\cos^{-1} \left(\frac{f}{2f_{opt}} \right) - \frac{f}{2f_{opt}} \sqrt{1 - \left(\frac{f}{2f_{opt}} \right)^2} \right] \quad (3.16)$$

where f_{opt} is described by the Eqn. 3.13. This MTF falls off from 1 at zero frequency to 0 at a twice the coherent cutoff frequency, which is given in more general form by:

$$f_{incoh,max} = \frac{2NA}{\lambda} \quad (3.17)$$

In the graphical form MTF function is shown on Figure 3.12.

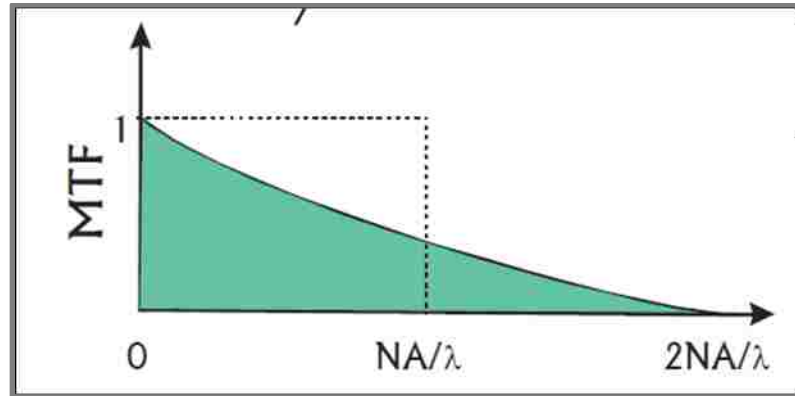


Fig. 3.12 Modulation transfer function (MTF) for the incoherent illumination scheme. The x-axis represents spatial frequency in the image distribution.

Even if the incoherent cutoff frequency (intensities) is higher than it's coherent amplitude counterpart, the coherent ATF is a constant function, while the MTF for the incoherent case rolls off at the higher frequencies. In other words for the IL technique, where we use off-axis illumination to cover the higher frequencies having a constant MTF is more important because the contrast, the ratio of amplitudes between different frequency components, is reduced in the incoherent case compared to the coherent. In all

worked that was performed earlier and demonstrated here we have used a coherent source of the illumination in our experimental setups.

Now, coming back to development of the imaging lithography, the next step towards higher NA s and smaller features was made using $\lambda = 364$ nm and $NA = 0.356$ (before $NA = 0.04$). A CD of 250 nm was demonstrated, which is equivalent to a $k_1 \sim 0.25$ [23].

Here we demonstrate [13,24] a significant step in the development of the IIL technique by using high 0.9 NA μCat^{TM} *Cheetah*TM lens by Corning Tropel [25] and a illumination source with the operation wavelength of 244 – nm. Because of a such high NA lens, for the off-axis illumination we retained a zero-order within the optical system, where in the case of low NA lenses it was send around and was reintroduces on the image side. As an arbitrary printing pattern for demonstration of the ultimate resolution limits of the IIL we use a mask with Manhattan geometry pattern; it is shown on Figure 3.13.

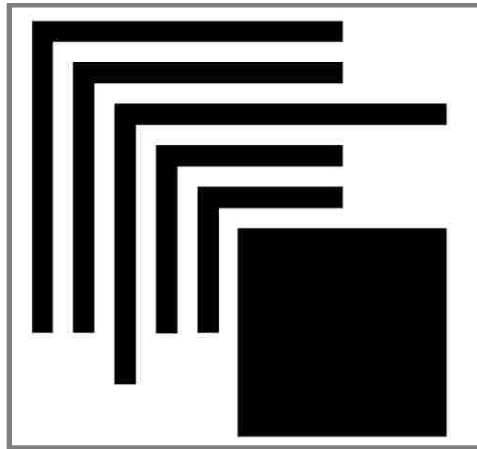


Fig. 3.13 Manhattan geometry mask pattern used to evaluate resolution limits of the IIL technique.

This pattern reflects many of the challenges that modern lithographic industry is facing. It has a combination of dense patterns in the orthogonal directions (x, y), corner connections and a small isolated features as well as a combination of small and large features (single

line and large square block) in one pattern. In the lithography it is common to have a Cartesian coordinate orientation (also known as Manhattan geometry) for the mask patterns.

IIL is similar to quadrupole off-axis illumination with a small partial coherence for each off-axis illumination beam, and with quadrupole oriented along the principal (x , y) axes of a Manhattan geometry pattern to maximize the extent of the spatial frequency capture (as in dipole illumination, but with only a single mask). The x - and y -axis spatial frequencies are covered with separate off-axis illumination exposures. Figure 3.14 shown multiple exposure scheme, with some frequency redundancy, that is present due to overlapping of separate off-axis (x and y) exposures.

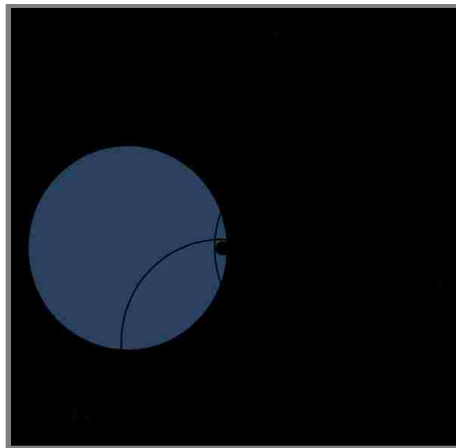


Fig. 3.254 Multiple exposure scheme where some frequency redundancy is present due to overlapping of the x -, y - off-axis exposure areas.

In order to avoid this frequency coverage redundancy we introduce a Pupil Plane Filters (PPF).

3.2.2.2 Pupil Plane Filters (PPF)

We can write the spectrum of the intensity of the IIL image as:

$$I(f_x, f_y) [\delta(f_x, f_y) + B_x(f_x, f_y) + C_x(f_x, f_y) + B_y(f_x, f_y) + C_y(f_x, f_y) + \delta(f_x, f_y)] \quad (3.18)$$

Where:

- The first term is x -off-axis exposure
- Second term is y -off-axis exposure
- Linear (imaging) terms of the off-axis exposure are: $B_x(f_x, f_y)$ and $B_y(f_x, f_y)$
- Quadratic (nonlinear non-imaging) terms of off-axis exposure are: $C_x(f_x, f_y)$ and $C_y(f_x, f_y)$
- The δ -functions correspond to the zero-order (transmitted) beams through the mask.

Using PPF to avoid multiple counting of the frequency space by separating these various exposures (in time or in polarization or both) eliminates many nonlinear terms in the imaging and results in a high quality image extending out to the frequency space limits of the imaging system [12, 26]. Combination of the PPF applied for the x - and y – off-axis exposure is shown of the Figure 3.15.

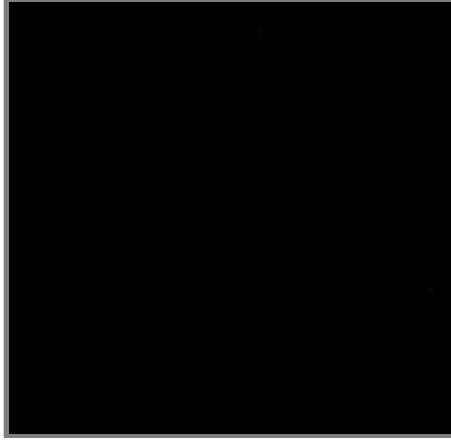


Fig. 3.15 PPF configuration for the combined x- and y- off-axis exposures. Using PPF eliminates redundancy in the frequency space coverage.

Now we look closely to a single off-axis exposure. There are high nonlinear cross terms in the intensity distribution of the IIL image, the “dark filed” terms. We have interference between zero order and a high frequency order that will produce edges of the image. We have interference between the zero order and a low frequency order that will fill in the edges of the image. And finally we have a cross talk between the low and high frequencies. This cross talk does not give us any useful information, but degrades the quality of the finale image. In order to avoid that cross talk we modify our existing PPF to work as a low pass filter. Only zero order and high frequency order are coming through. Since no low order frequencies are present in the image during two off-axis exposure we need to retain them trough a separate, third, exposure, where only zero order and low frequency orders are present. However, our, high NA , lens transfer function has a central obscuration, due to design specifics of the lens (lens is a catadioptric), and we are forces to reintroduce low frequency exposure at a small offset from the normal incidence. For that purpose a separate PPF was constructed. New, modified set of PPF is shown in Figure 3.16.

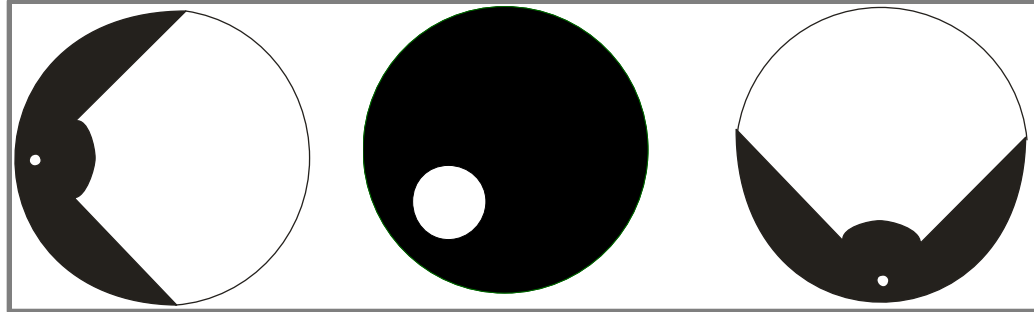


Fig. 3.16 Pupil plane filters (PPF) used in the PROLITH™ simulations and during the experiment. Left and right filter were used for the high-frequency off-axis exposures, filter in the center were used for the low-frequency exposure.

The filter for the high x -spatial frequencies includes a small hole at the edge of the pupil that transmits the zero-order beam. In the experiment, the filter is put in place and the off-axis tilt is adjusted to ensure that the zero-order beam is cleanly transmitted through the 0.5 mm hole ($\sigma = 0.003$). A very small size and the largest possible offset within the pupil are required in order to maximize the spatial frequency content of the image. With an air medium between the lens and the wafer, the highest spatial frequency available with 244-nm exposure tool with a numerical aperture of 0.9 corresponds to a half-pitch of 68-nm. Allowing for $\sim 10\%$ sub bands above this central frequency, this suggests that ~ 75 -nm half-pitch patterns should be accessible.

Now we have all necessary parts to begin constructing our IIL experimental setup. But before we start a complex job of arranging optical system and performing exposure processes we can do quicker evaluation of resolution capabilities of our future lithographic system using software tool called PROLITH™.

3.2.2.3 PROLITH modeling

PROLITH is commercial lithographic software tool that allows modeling and simulation of many different aspects of the lithography process such as different

illuminations schemes, various NAs , post exposure processing and development. It is also provides easy and unrestricted access to the Fourier plane, since for the imaging system this access can be problematic, where different schemes of pupil plane filters can be tried. As a result PROLITH can generate aerial images, contrast images and photoresist (PR) layer images. Different PR profiles with real chemical properties are embedded in the software.

We start our modeling process by creating a Manhattan geometry mask. Since PROLITH uses one-to-one optical scheme, our designed mask should have the same dimensions as a final image we want to model. As it was discussed before, we should be able to resolve patterns with the CD of ~ 75 – nm. But this is a maximum resolution for this system and it can be a challenging to reach that limit on the first attempt. So we will start with bigger CD of ~ 85 – nm. That will give us an idea about the processing flow and possible constrains. Figure 3.17 shows a typical PROLITH generated Manhattan geometry type mask with CD ~ 85 - nm.

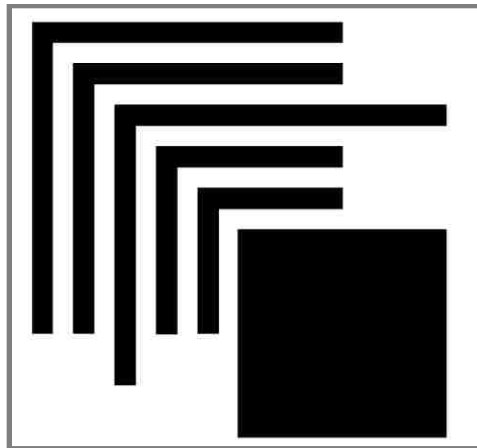


Fig. 3.17 PROLITH generated Manhattan mask.

Then PROLITH can generate a Fourier transform of the mask at the pupil plane as it shown on the Figure. 3.18.

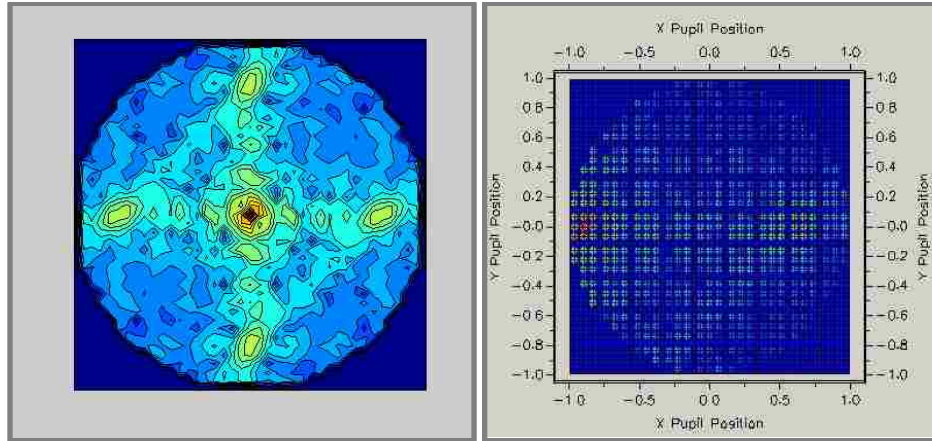


Fig. 3.18 Prolith generated Fourier transform of the Manhattan geometry mask at the pupil plane of the imaging system, on axis illumination (left). X-off-axis illumination is applied (right).

Because we utilize 3 separate exposure scheme: x -, y - off-axis exposures and one low frequency exposure, we have to create a 3 pass system in the Prolith. In each pass an appropriate off-axis illumination scheme with its own PPF is applied. Because every pass is independent from each other it allow us a precise and independent control over the polarization in each pass. Figure 3.19-3.21 shows individual PPF and the Prolith replica in the pupil of the imaging system.

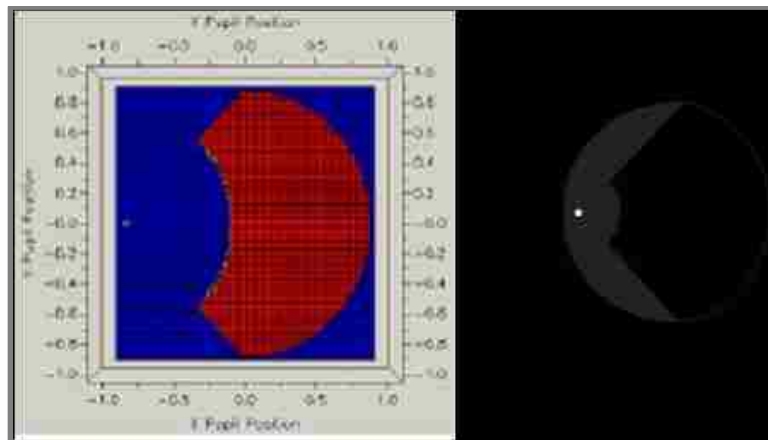


Fig. 3.19 PPF and its Prolith replica at the pupil plane of the imaging system for the x -off-axis illumination. Frequency range in the x and y directions are $-0.9 \div 0.9 NA$.

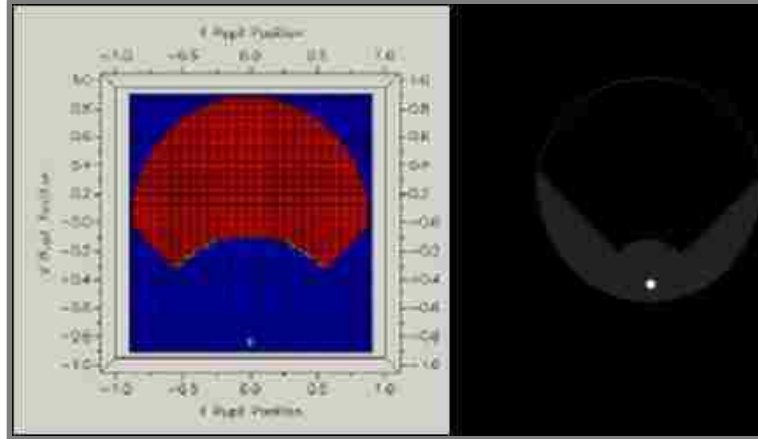


Fig. 3.20 PPF and its PROLITH replica at the pupil plane of the imaging system for the y -off-axis illumination. Frequency range in the x and y directions are $-0.9 \div 0.9 NA$.

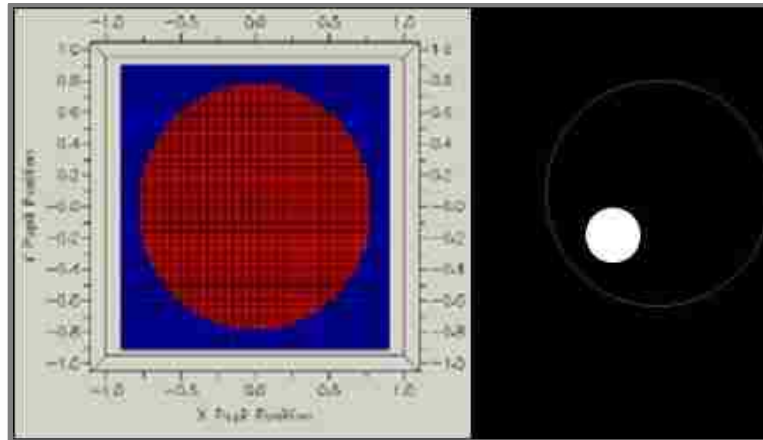


Fig. 3.21 PPF and its PROLITH replica at the pupil plane of the imaging system for the low frequency illumination. Actual frequency range of the opening in the x and y directions are $-0.3 \div 0.3 NA$. PROLITH model is not scaled!

Next step is to generate an aerial image. Figure 3.22 shows an aerial image for the 85 – nm CD Manhattan pattern, where different colors represent different intensities.

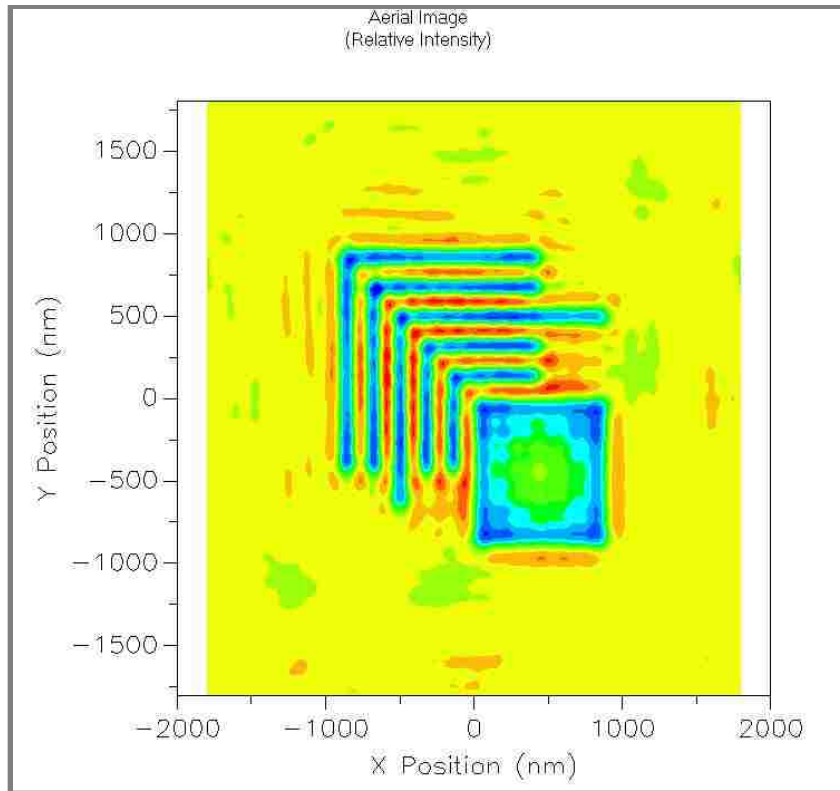


Fig. 3.22 Aerial image of the Manhattan pattern with CD ~ 85 nm generated by the PROLITH after applying 3 exposure ILL scheme. Different color represents different relative intensity.

Well resolved features of dense pattern, isolated lines and big box are well defined on the generated aerial image. This image is then transferred in the PR layer. We will talk about sample preparation in the separate section where all the details on the PR layers will be addressed. On the Figure 3.23 PROLITH generated, final, developed PR pattern (left) along with its crosscut (right) is shown.

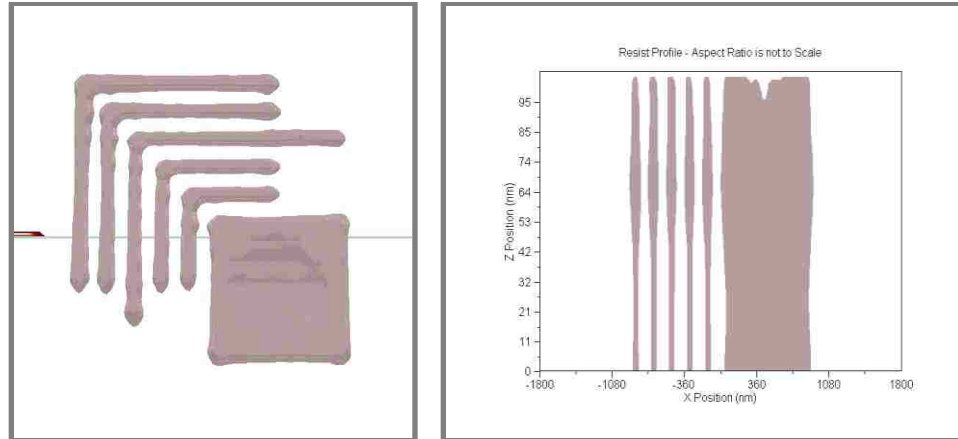


Fig. 3.23 PROLITH generated final, developed, PR transferred Manhattan image with CD ~ 86 nm on the left. Its crosscut profile along x-axis on the right. Crosscut profile is not scaled.

In order to evaluate the line profile of the final image a separate crosscut along the z direction can be taken. That crosscut is demonstrated on the Figure 3.24

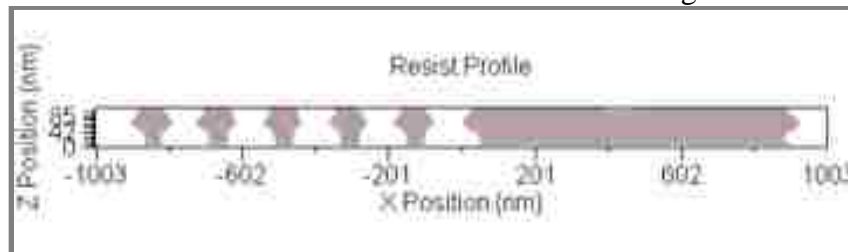


Fig. 3.24 PROLITH generated resist profile crosscut along the z direction. Well resolved individual lines are visible.

As an example of what kind of information PROLITH can give on the line profiles and film stack, we are showing a case where developed PR line profile has a shape of the standing wave. That means that the anti-reflection coating (ARC) layer underneath the PR layer was not properly optimized for the smallest reflection. That issue can be address by varying the thickness of the ARC layer and eliminating the standing wave profile. Other than that, we have a very good, well resolved and defined Manhattan pattern transferred in the PR with the CD of ~ 86 - nm. Similar process was repeated for the smaller CDs in order to evaluate the ultimate resolution limit of the optical IIL system for the arbitrary pattern. Figure 3.25 shows modeling results for the CDs of 80 -, 75 – and 70 – nm.

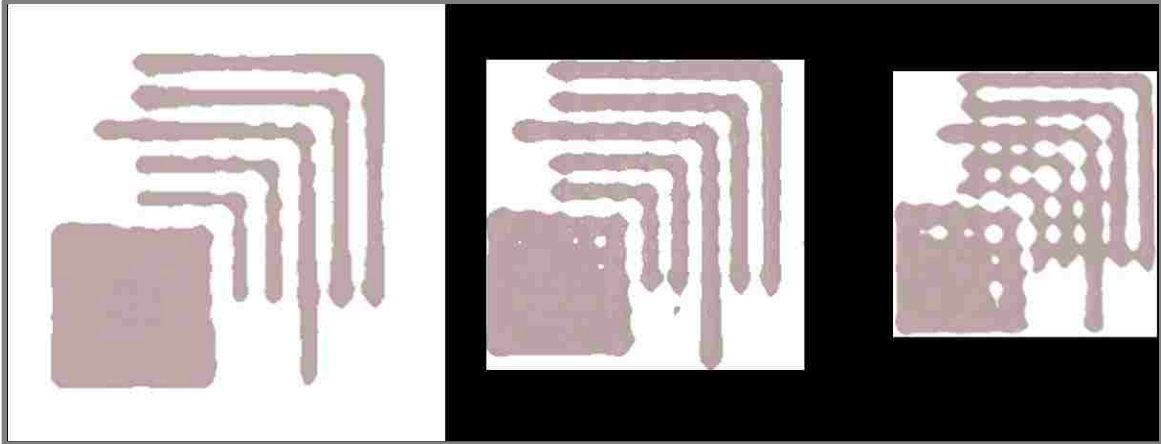


Fig. 3.25 PROLITH generated PR patterns of the Manhattan structure with CDs of 80 – nm (left), 75 – nm (center) and 70 – nm (right). Resolution of the system breaks at ~ 70 – nm CD. Those results were achieved without use of any resolution enhancement techniques (RET).

We see that at CD of 75 – nm we have good resolved dense and isolated lines but there is some image degradation, in the form of various size holes, inside the big box. The detentions of this box is 10xCD, meaning that we are trying to cover a very high frequency range during our IIL exposure. In the modern industry world the highest distribution of sizes on one layer is ~ 3:1, which makes a smaller frequency range than in our case. Keeping this in mind we can say that we successfully resolved an arbitrary pattern structure with CD ~ 75 nm. However, at 70 nm we no longer resolving dense line array and the box. Both of them have significant pattern degradation: cross-linking of lines, holes inside the box. Because of that we are concluding that the resolution of our optical system breaks at ~ 75 nm CD for the arbitrary pattern geometry. It is important to note that this result was achieved without use of any Resolution Enhancement Techniques (RET). So if we take a minimum of 75 – nm half-pitch node for the 244 nm dry 0.9NA system and directly scale it to the 193 nm immersion (NA of 1.35, commercially available lens) system that will leads to $75 \times (193/244) \times (0.9/1.35) \sim 40$ nm half-pitch node without use of any RETs.

3.3 Experimental setup

A 0.5-W, continuous wave, intracavity doubled, Ar-Ion laser at $\lambda = 244$ nm was used as the illumination source for the IIL experiment. A key element of the experimental setup is the 0.9 NA μ CatTM CheetahTM lens [25]. Properties of this lens are listed in the Table 3.1.

Table 3.1 Specifications for the 0.9 NA Cheetah lens.

Trade name	Cheetah 244
NA	0.9
Field μ m	100
Wavelength (nm)	244
Pupil Diameter (mm)	3.6
Tube length	Infinity - custom tube lens
Working distance (mm)	1.1
Telecentric (degrees)	0.1 - object side
Transmission (%)	75 - normal
Optical Material	Excimer SiO ₂
Obscuration (%)	15 - linear
Cemented Surfaces	None
Internal Foci	None
Diameter (mm)	72 - maximum
Length (mm)	72 - maximum
Mass (g)	1200

The imaging pupil plane inside the lens is inaccessible. Therefore, a set of transform lenses is used to relay the pupil plane to an accessible position for the insertion of pupil plane filters, where the physical size of the NA circle is ~ 18 mm. Proposed 22x reduction optical system for relaying the pupil plane is shown on the Figure 3.26.

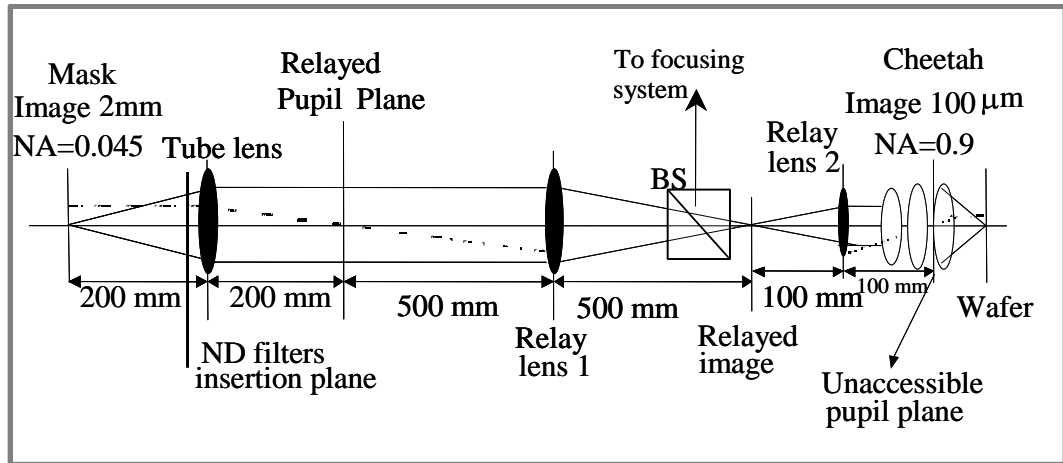


Fig. 3.26 Schematic layout of the 22x reduction telecentric imaging geometry showing imaging and illumination rays and relative positions of lenses and relayed planes.

The lens is catadioptric with a central obscuration of 15% of the NA. Specifically, this means that coherent illumination at normal incidence is not possible because the lens blocks the zero-order beam. Thus, an off-axis strategy must be adopted for the low-frequency portions of the image as well as for the high frequencies in the IIL spectral decomposition. The optical system track was simulated with standard, commercially available, ray-tracing software (ZEMAX). The full $100 \times 100 \mu\text{m}^2$ field-of-view at the wafer plane has a wave front flatness of 0.82 waves. Result of the ray-tracing wave front calculation can be seen on the Figure 3.27.

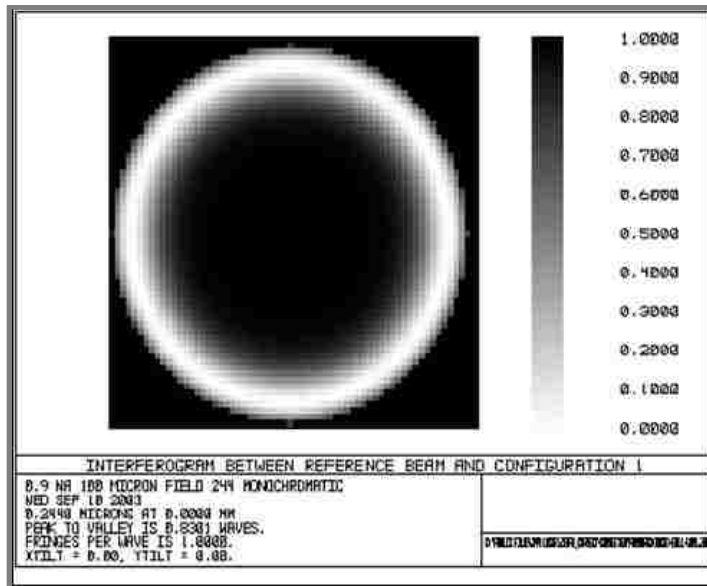


Fig. 3.27 ZEMAX calculation for the full $100 \times 100 \mu\text{m}^2$ field of view for the *Cheetah* lens showing wave front flatness of 0.82 waves.

There are several additional elements in the setup that are associated with image focus. The depth of focus for the high-frequency ILL exposures is only ~ 200 nm, requiring precise z -positioning of the wafer; since only a single level is printed; there is no x - y positioning requirement. Wafer flatness is not an issue for the small lens field-of-view, but its tip and tilt are. For the z positioning and tip, tilt controls wafer chuck was equipped with 3-axis piezo-motorized stage. For visual feedback of the image focus we built an optical system associated with the beam splitter cube in the primary optical path that provides a real-time view of the image – i.e. magnifies the reflection of the mask image from the photoresist surface back through the *Cheetah* and projects the image onto a CCD camera. Since the optical system onto the camera can accommodate an out-of-focus image, it is necessary to simultaneously image the reflected pattern as well as artifacts on the photoresist surface.

A schematic layout of the experimental setup is shown in Figure 3.28

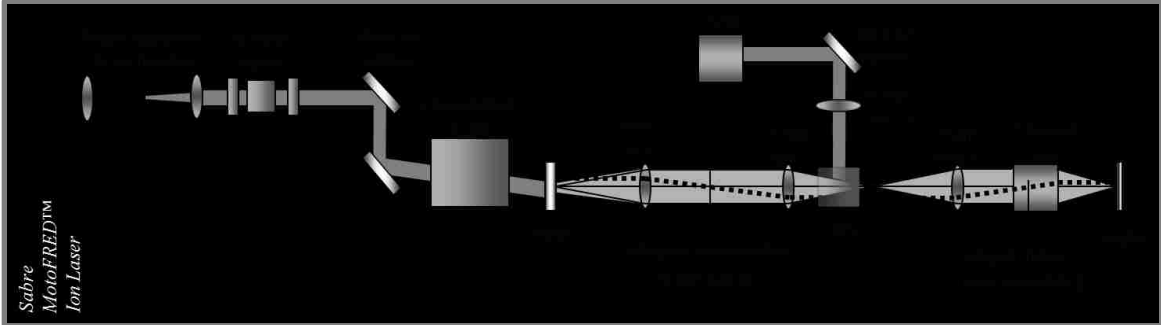


Fig. 3.28 Schematic layout of the experimental IIL tool with 244-nm laser source, 0.9NA *Cheetah* objective lens, and a real-time focusing system.

As we mentioned above, we use a 224 – nm laser source for the illumination of the mask. The output beam, exiting the laser, is only few millimeter in diameter and needs to be conditioned before it can be used for our experiment. A set of lenses was used to expand and collimate the beam, and to remove astigmatism arising from the optical pass through the berifringet frequency doubling crystal inside the laser cavity. Due to the need to independently vary the intensity of each individual exposure in our scheme and the fact that it is more convenient to have, a separated from the laser source, control over the power we have implemented the control optics path. In this control optics path a combination of a first half-wave plate and a polarized beam splitter cube were used to control the beam intensity. By the rotation of the half-wave plate we can select how much of the incident beam intensity will be transmitted in to the system and how much will be dumped. We can attenuate passing beam within 10 ÷100% range. A second half-wave plate is used to control the polarization of the beams for the various IIL exposures. It is important to retain the proper polarization of the beam during individual exposure. Especially this becomes critical when we are working the 193 nm system and trying to resolve small half-pitch sizes. As a printed size becomes smaller a TE polarized beam retains its intensity response in the PR, while the TM polarized beam loses its response

dramatically. Figure 3.29 shows intensity response, in the PR for various half-pitch sizes, for the TE and TM polarization for the 193 nm wavelength.

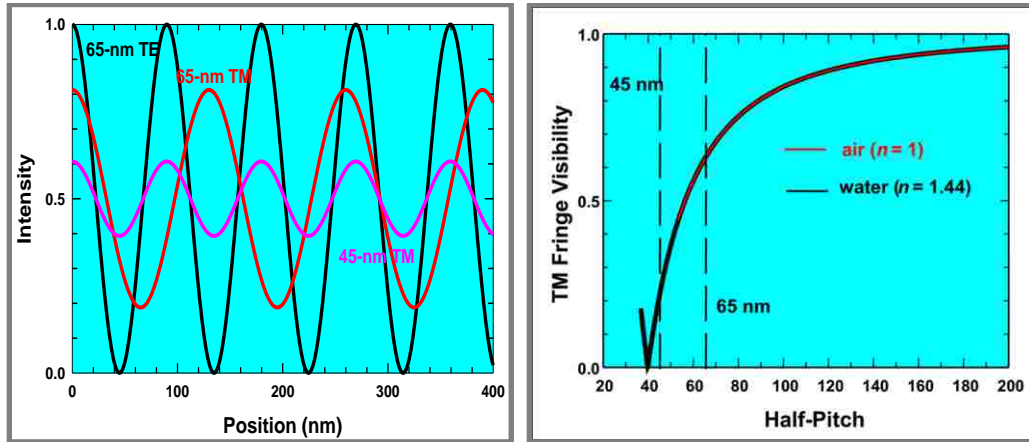


Fig. 3.29 193 nm wavelength TE and TM polarized beam intensity response variation in the PR for different printed half-pitches.

A pair of steering mirrors levels the beam and sends it in the illumination block.

This portion of the experimental setup was designed specifically to address the challenge of having separate of-axis illuminations for the x -, y - and zero order exposures. Also for the each exposure an appropriate PPF has to be used and carefully aligned within the imaging system. On the other hand the of-axis illumination angle for each exposure should be accordingly adjusted for different printed CDs. The following illumination scheme, show on the Figure 3.30, was designed and applied.

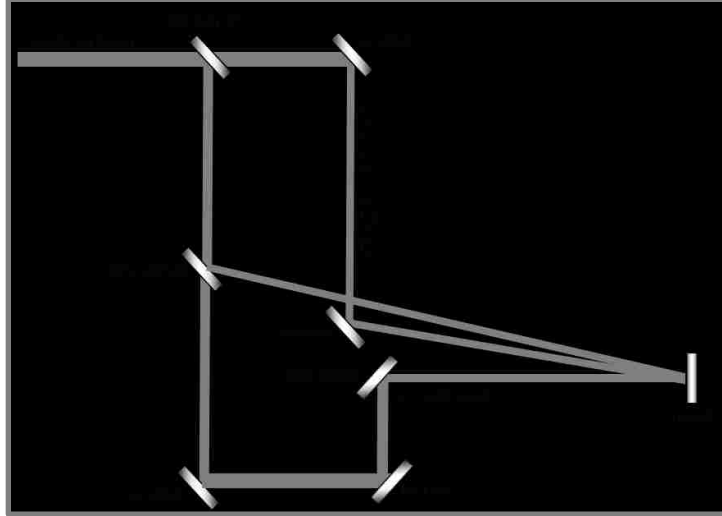


Fig. 3.30 Illumination setup designed to accommodate 3 off-axis independent exposures. Each off-axis beam has its own intensity and angle control, independent from one another. All beams are aligned with appropriate PPF inserted at the relayed pupil plane.

Incident beam is divided by the 65/35 beamsplitter (BS). Transmitted portion of the beam is then used for the low-order off-axis illumination arm. Reflected part of the beam is divided by the second 50/50 BS. This BS is used as a mirror and reflected part of the beam is the x -off-axis arm. Finally the transmitted beam is steered using set of mirrors to the periscope which rotates the polarization of the beam and sends it to the mask as the y -off-axis illumination.

The mask patterns are Manhattan structure patterns [dense/isolated nested ells with a large box (10 CD) to present a range of spatial frequencies]. The binary chrome-on-glass mask does not incorporate any optical proximity correction (OPC) or phase shift mask (PSM) features. As a result of the 22x reduction, the mask fabrication was relatively straightforward and posed no special issues.

3.4 Experimental Protocol

3.4.1 Sample preparation

We use single side polished Si wafer. Before the wafer can be used its need to be cleaned in the piranha bath. Piranha is a strong acid that is generated freshly before every cleaning and is a mixture from $\text{H}_2\text{O}_2:\text{H}_2\text{SO}_4$ in the ratio of about 1:4. Then the wafer is deoxidized in hydrofluoric acid (buffered), which makes it also hydrophobic. Final step is to dry the wafer on the hotplate. All of the preparations are done in the Class 1000 cleanroom environment which insures that no contamination of the wafer surface is present. Now we have clean wafer ready to spin on the antireflection coating (ARC) and photoresist layer (PR).

3.4.2 Photoresist/ARC Stack

Because of the relatively small depth-of-focus (~ 200 nm) and the small CDs, the ARC and PR thickness have to be very carefully optimized. We us bottom ARC UV 112 from Brewer Science [16]. Optimal thickness for the ARC can be obtained from supplied data sheet where graph of reflectivity dependence from thickness for different types of substrates is provided, as it shown in the Figure 3.31.

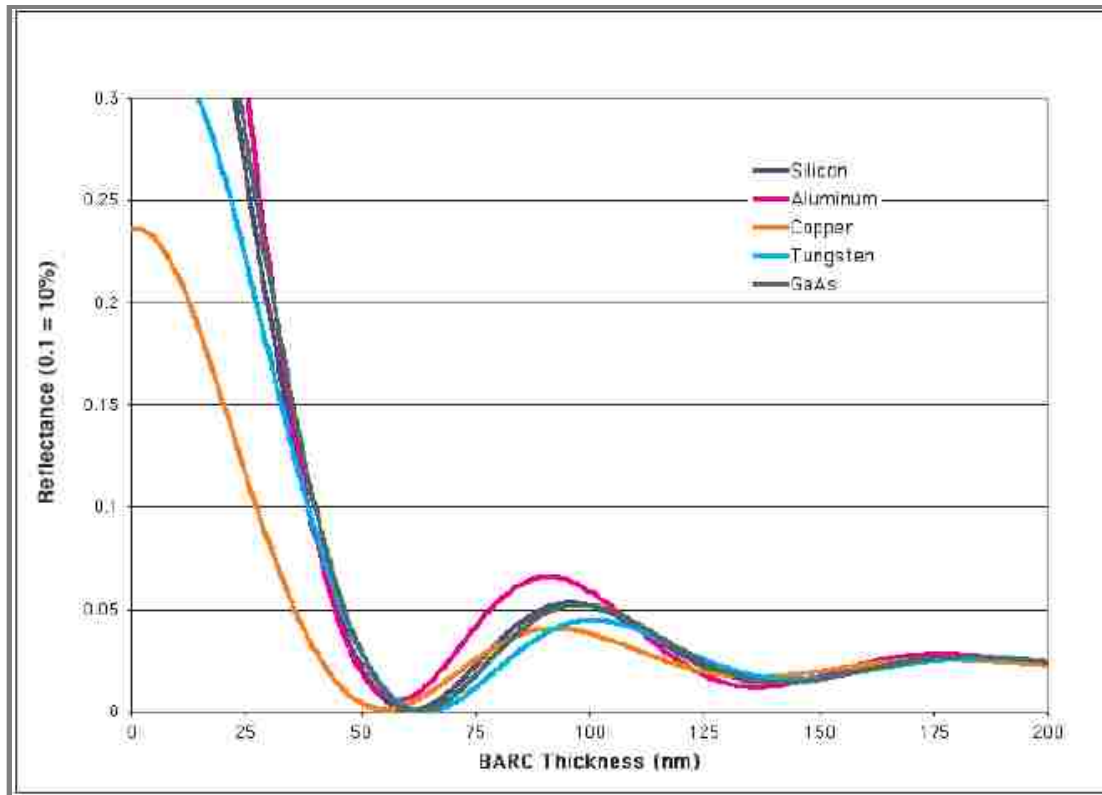


Fig. 3.31 Reflectivity curve vs. ARC thickness for different substrates for the DUV 112 ARC provided by the Brewer Science data sheet. First reflectivity min at ~ 65 nm, second min is at ~ 145 nm.

First minimum of the reflectivity curve is observed at ~ 65 nm. However this graph does not take in the account fact that angles at which exposure beams enters the PR layer will be different depending on the CD and pitch sizes of the pattern that is being printed. So final tuning of the ARC thickness can be done using PROLITH software or some other program that can account for different angles of the incident beam. Once the desired thickness is established then the ARC layer can be spin on the wafer. Spin speed determines the final thickness of the layer and can be estimated using following graph in the Figure 3.32.

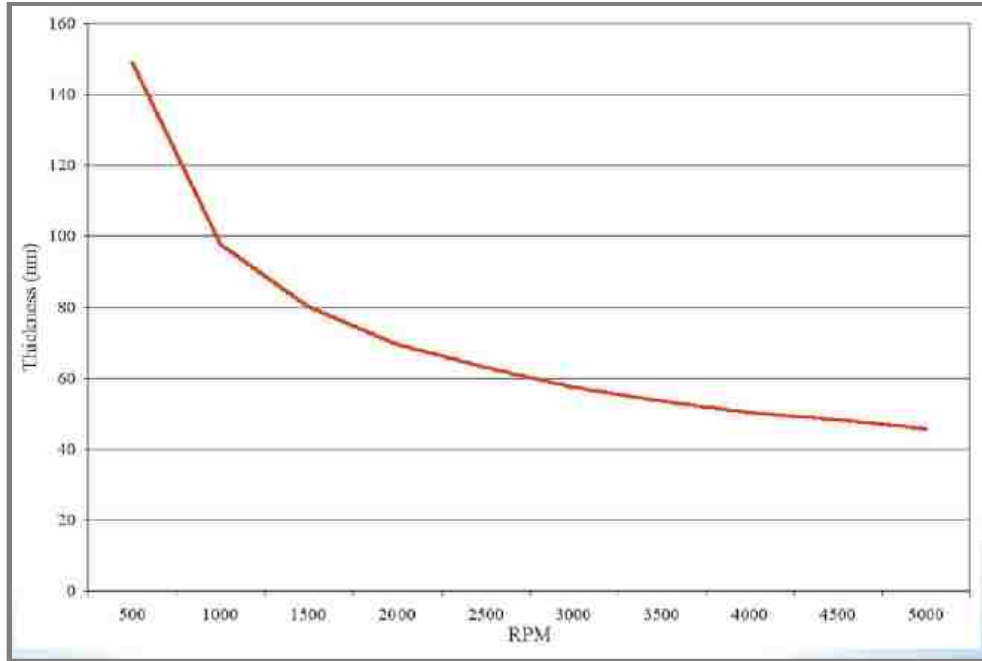


Fig. 3.32 Spin speed curve for the DUV 112 ARC.

High temperature bake at 205⁰ C for 1 min. is required after spinning. After wafer is cooled the UV 210-0.3 photoresist is spined on. PR was from Rohm and Haas [15] corporation. Thickness of this PR from the bottle can be determined using spin speed curve shown in the Figure. 3.33.

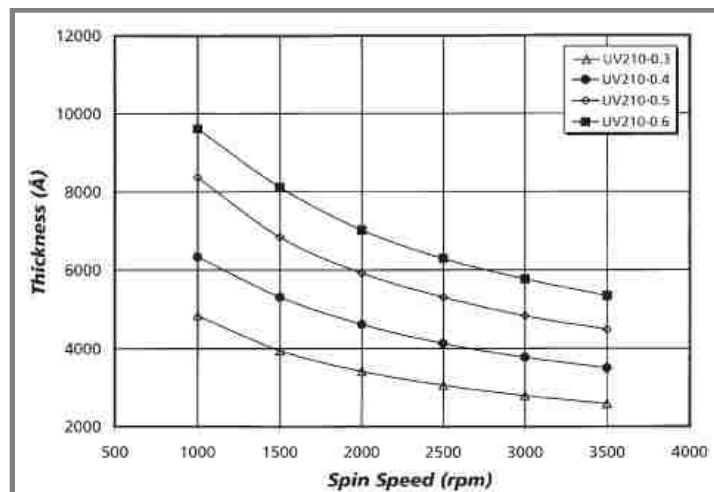


Fig. 3.33 Spin speed curve for the Rohm and Haas UV 210-0.3 PR.

Because of a small depth of focus of ~ 200 nm of our imaging system, we decide to have a PR layer thickness of only ~ 100 – 120 nm. Looking at the Figure 3.33 one can see that

in order to reach this thickness of PR we need spin speed of over 4500 RPMs. That is not very practical. To obtain desired thickness original PR was diluted using Solvent 11 in the proportion of: 2 parts of PR to 1 part of Solvent. This will change the spin speed curve. New spin speeds were obtained by coating several samples at different speeds, flash exposing half of the sample, developing and then estimating the final thickness of the PR layer under the scanning electron microscope (SEM). At the time, when this work was done, we did not have an access to the UV ellipsometer, which would be more accurate and proper way of measuring PR layer thickness. A spin speed of ~ 2700 RPM for the diluted PR will give us a target thickness of ~ 110-120 nm. Again, after spinning a hard bake at 130°C for 1 min is required. Please note that the DUV photoresist, for the 244 nm wavelength, belong to a group of so called “chemically amplified” deep UV photoresist. The main idea is that during exposure photoacid generators (PAG’s) of the resist react to the exposure light and decompose forming an acid species, which diffuses and catalyzes a deprotection reaction during the post exposure bake (PEB) rendering the insoluble resist soluble in a developer [27]. Typically this DUV PR is more sensitive to the UV light, than a regular UV photoresist developed for the 365 nm wavelength, and the required exposure energy is on the order of 30 mJ/cm². Having a relatively high power source will result in the exposure time of few seconds.

Both ARC and PR coatings, spin bake, PEB and development are done using state of the art, professional grade spinners and hot plates, see Figure 3.34 – 3.35.



Fig. 3.34 Brewer Science hot plate.



Fig. 3.35 Brewer Science spinners.

3.4.3 Exposures

The exposure process starts with insertion of the x -direction pupil plane filter and setting the focal position using a reduced intensity beam and the real-time focusing system. *At this point the mask and wafer are fixed relative to each other, no further adjustment of the positions is allowed.* After the insertion of the ND filter in the beam path the first exposure is carried out, the pupil plane filter for the y -direction is inserted and the second exposure is carried out. Then the low frequency pupil plane filter is used and the third exposure is made. A post exposure bake at 130°C for 1-min on a vacuum chucked hot plate, followed by a 45 sec CD-26 puddle develop completes the processing.

3.5 Fabrication of periodical and arbitrary structures

3.5.1 Fabrication of the periodic grating in the PR

In order to get a better understanding of the real resolution capabilities of the experimental setup and to evaluate the experimental process we started with fabrication of the periodic grating in the PR using different set of masks.

Using grating mask does not require implementation of the PPF and takes only one off-axis illumination beam. We have a set of 3 masks that produces final images with pitches of 180 – (CD – 90 nm), 170 – (CD – 85 nm), 160 – (CD - 80) and 150 – (CD – 75 nm) nm. Next several figures show scanning electron micrographs (SEMs) of the developed PR patterns.

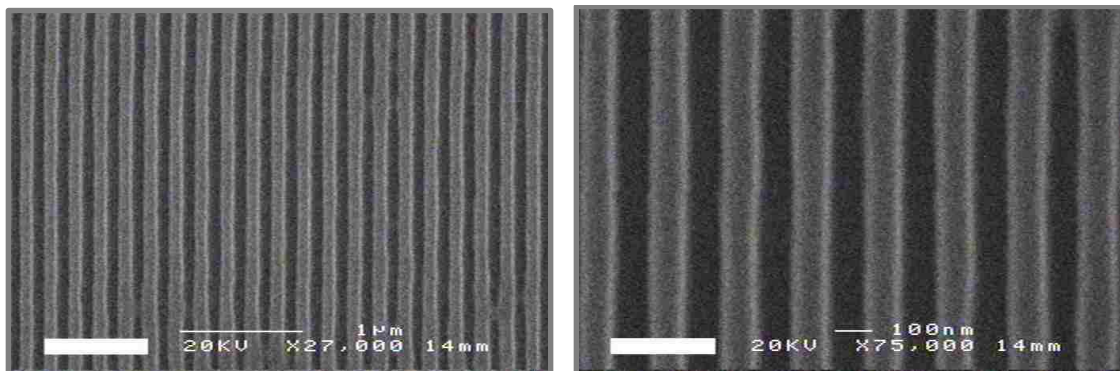


Fig. 3.36 SEM picture of the developed PR pattern with pitch of 180 – nm, and CD of 90 nm.

We see that lines are well defined. Duty cycle is close to 50/50.

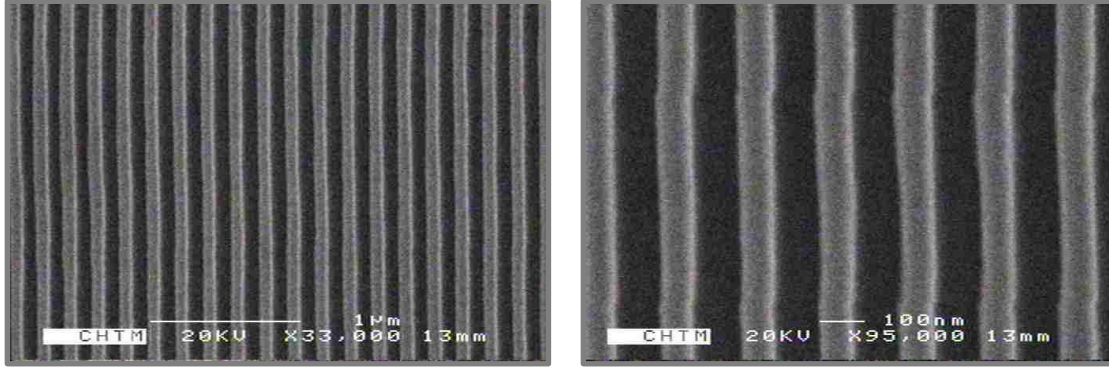


Fig. 3.37 SEM picture of the developed PR pattern with pitch of 170 – nm, and CD of 85 nm.

Some wobbling of the lines is visible on the Figure 3.37 on the right. This wobbling is due strictly to some charging of the sample in the SEM setup, and the some issues with the image capture software. Large scale image shows that the PR lines are continuous and does not have any shifts or brakes.

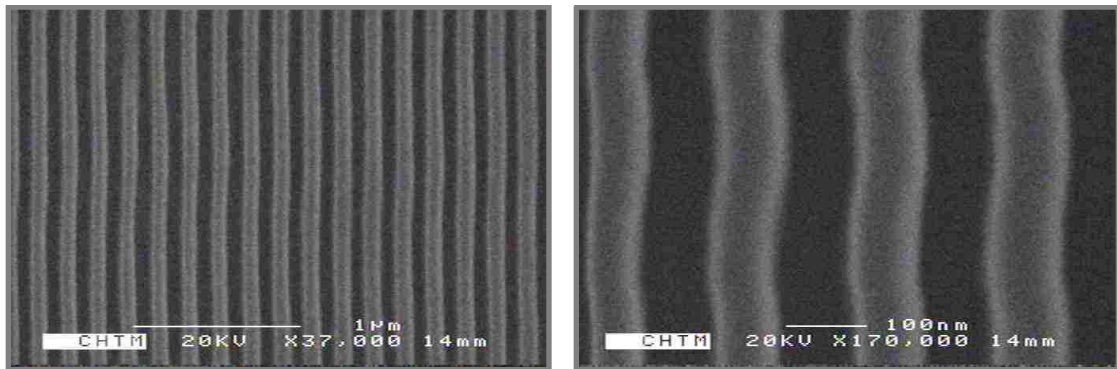


Fig. 3.38 SEM picture of the developed PR pattern with pitch of 160 – nm, and CD of 80 nm.

And again we see very good resolved lines, with duty cycle around 50/50. At this point we are able to print 80 nm CD line at 160 nm pitch. Wobble in the lines are an artifact of the image capture software.

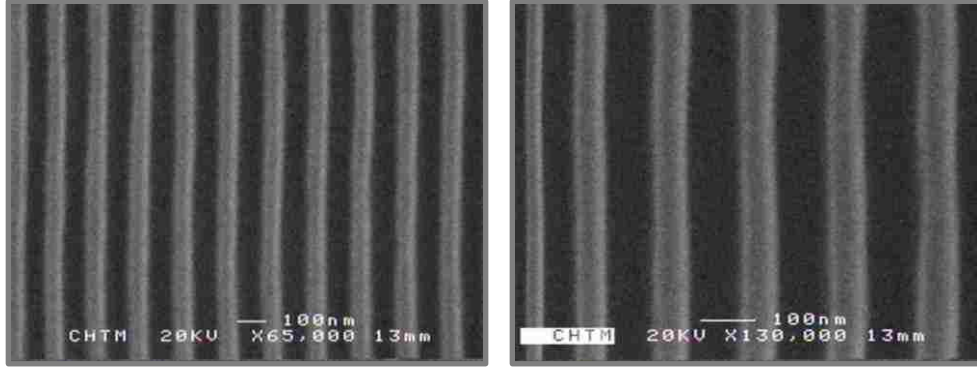


Fig. 3.39 SEM picture of the developed PR pattern with pitch of 150 – nm, and CD of ~ 70 nm.

This is an important result because we have demonstrated the IIL resolution of a periodic pattern at 150 nm pitch (75 nm half-pitch node), with the duty cycle of 50/50. However due to some overexposing we see that in this case CD is smaller, and on the order of ~ 70 nm. That again prove the fact that we are limited by how close things can be together, pitch, but not how small we can print them, CD. If we would apply higher exposure dose final line width could be even smaller. But even at this pitch we see very good defined lines.

Now we will try to push resolution of our IIL setup even further and will see if we can print 140 nm pitch with 70 nm CD.

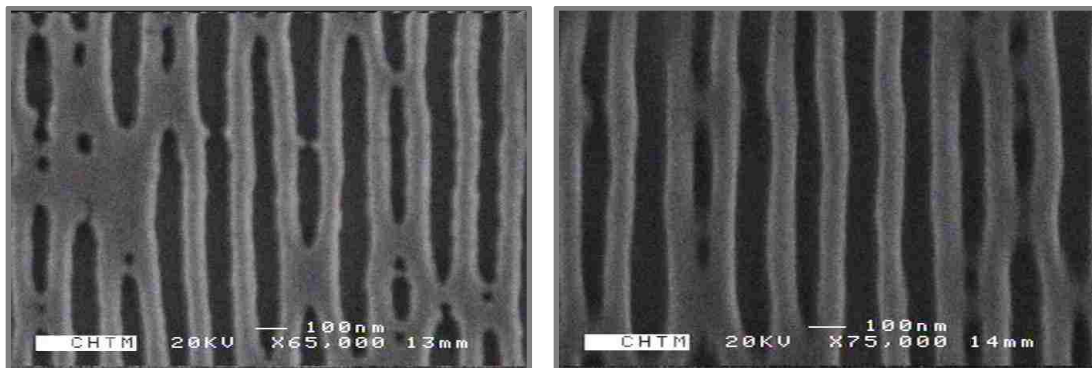


Fig. 3.40 SEM picture of the developed PR pattern with pitch of 140 – nm, and CD of ~ 70 nm.

We see that lines are no longer resolved: they are cross connected at the top, some of them are bend or wobbled. We can see possibly two reasons for this: one is that the high

frequency order is approaching the edge of the *Cheetah* lens, were the transfer functions starts to fall off and second one is that the PR starts to lose its capability to resolve such small pitch. So we consider that we have successfully resolved a 150 nm pitch with 72 nm half-pitch (hp) node, which is equivalent to the resolution limit of $\sim \lambda/(3.6NA)$.

Our earlier PROLITH modeling predicted that we should be able to print Manhattan type arbitrary structure with the CD of ~ 75 nm. Here we resolved 75 nm CD grating with the pitch of 150 nm, however, one needs to keep in mind that for the PROLITH modeling we assumed “perfect” environment, meaning we have perfect lenses with no aberration, lenses are exactly aligned on the optical path and the PR has no contamination. That translates in the fact that PROLITH predicted resolution limits are achievable but that task is not trivial.

3.5.2 Fabrication of the arbitrary Manhattan structure in the PR

We will start our process of exploring the resolution limit of the IIL system for the arbitrary Manhattan type structure by working our way from bigger sizes down to small ones.

We begin by printing a 113 nm CD pattern. For this size we need to use 3-exposure IIL scheme with implementation of the PPF. A SEM picture of the Manhattan pattern with 113 nm CD, corresponds to the Rayleigh k_1 of 0.42, printed using 244 nm wavelength with 0.9 NA lens is shown in Figure 3.41.

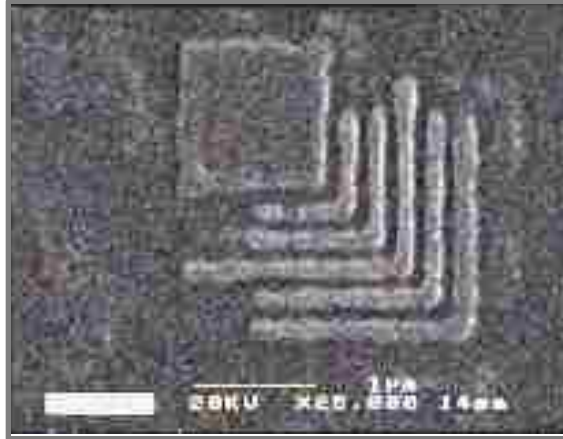


Fig. 3.41 SEM of developed PR for 3-exposure ILL for a CD of 113-nm ($k_1 = 0.42$) at a 244-nm wavelength and 0.9 NA . Isolated lines and the square edge of the box are well defined; dense lines are cleared.

Image transfer in the photoresist was successful. The image has a well-defined isolated lines as well as dense lines that are resolved and clear, and the line/space ratio is close to 50/50. Big box is resolved as well, but there is some distortion that present in the image suggesting existence of some astigmatism. This result was achieved with a simple binary mask without use of any mask based RETs such as optical proximity correction (OPC) or phase shift mask (PSM). If we scale this result to the 193 nm source and immersion 1.35 NA lens that will lead directly to the ~ 59 nm node.

Next step is to decrease the size down to the 100 nm CD which corresponds to the Rayleigh k_1 of 0.37.



Fig. 3.42 SEM of developed PR for 3-exposure IIL for a CD of 100-nm ($k_1 = 0.37$) at a 244-nm wavelength and 0.9 NA . Isolated lines and the square edge of the box are well defined; dense lines are cleared.

We successfully transferred the image in the photoresist. Image has a well-defined isolated large box, isolated lines as well as dense lines are well defined and clear. In this image it is visible that the line/space ratio has deviated from 50/50. This can be corrected by adjusting the exposure dose accordingly. Again, this result was achieved without use of any mask based RETs and without the use of intensity modulation in the pupil plane. Scaling this result to the 193 nm UV source and immersion lens at 1.35 NA will lead us directly to the 52 nm node CD.

Figure 3.43 shows the SEM of the developed PR pattern for the 3-exposure IIL for the 244-nm wavelength with 0.9 NA lens at the CD of 90-nm which corresponds to a Rayleigh k_1 of 0.33. We have transferred the image in the PR with good resolution of the dense and isolated lines. Large isolated box is defined as well. However the line/space ratio is not optimal. This result was achieved without use of any mask based RETs such as OPC or the phase shift. Scaling this to 193 nm source and immersion lens of 1.35 NA will produce ~ 47 nm CD node. Though presented image has a potential for improvement.

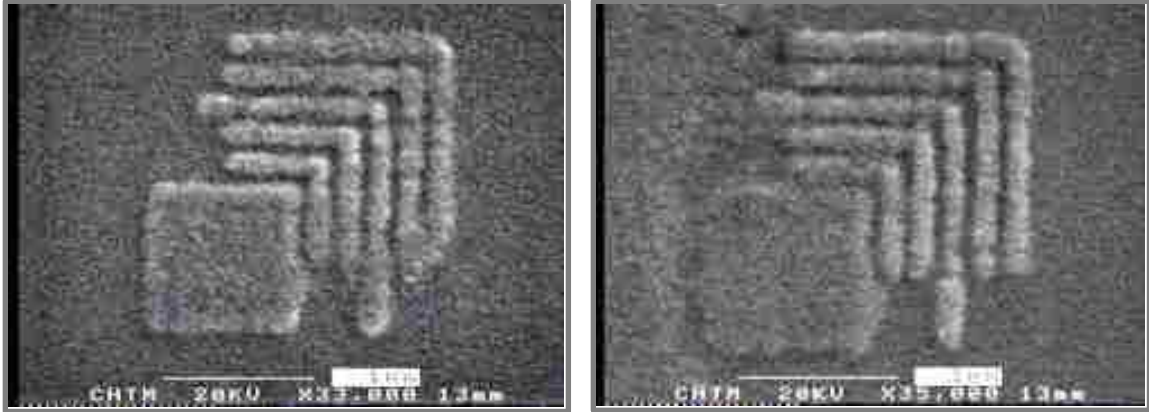


Fig. 3.43 SEMs of developed PR patterns for 3-exposure IIL for a CD of 90-nm ($k_1 = 0.33$) at a 244-nm wavelength and 0.9 NA . Large box is well defined. Ratio of the lines/spaces has deviated for the optimum. Isolated and dense lines are well defined. Both pattern were made with the same exposure dose level

Again it is clear that the line/space ratio is not longer 1/1. We have lines that are “fatter” than the spaces. Also there is some scumming present on the top of some lines. But because that happens in different places of the image (compare one from the left with the one on the right) we can consider that it is due to the lack of the contrast in the photoresist and the PR by itself having some difficulty in resolving such small features.

In order to address decreasing contrast of the aerial image that is transferred in the PR layer we have realized that the control of the intensity of the reference beam (zero order) with respect to the linear terms (high frequency orders) of the off-axis exposure can dramatically improve the image contrast. Interfering zero and a high frequency orders can be considered as a zero path length interferometer. So in order to achieve a higher possible contrast for the final image, intensities of the beams in the two arms of the interferometer need to be as close to equal as possible. We know from the diffraction phenomena that intensity of the zero order is the highest one: $(0)^2 > (1)^2 + (2)^2 + (3)^2 + \dots$, where 0, 1, 2 ... are the diffraction orders. PROLITH simulations result, shown in the Figure 3.44, demonstrates change in the contrast of the aerial image with respect to the change of the reference beam intensity.

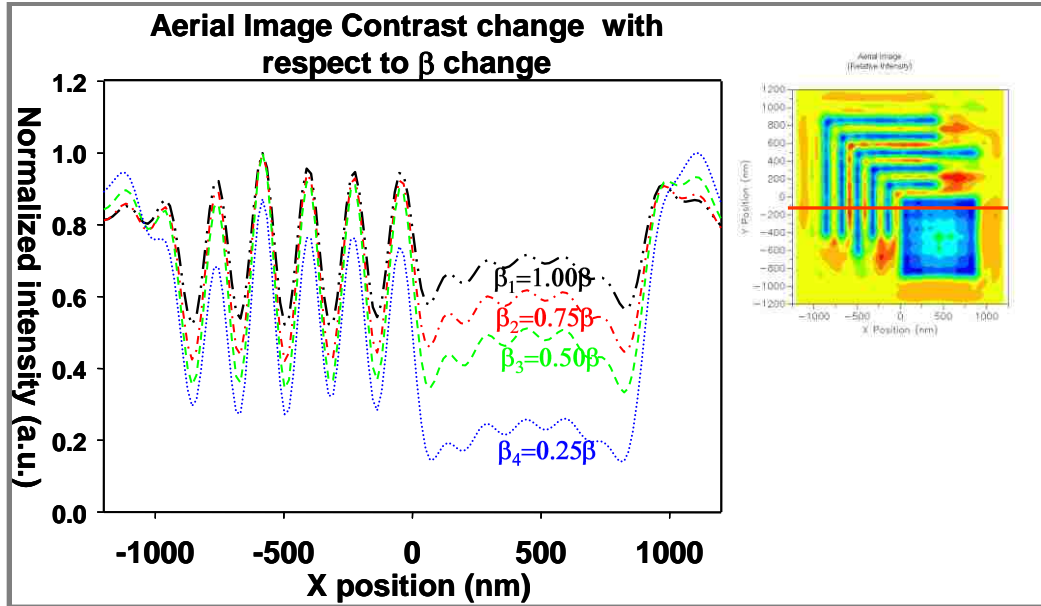


Fig. 3.44 Summary of the simulation results – aerial image contrast change with respect to a variation of the zero-order intensity. The aerial image contrast intensity crosscuts were taken along the red line of the aerial image shown on the right.

The aerial image contrast intensity crosscuts measurements were taken along the red line shown on the aerial image on the right-hand side of Figure 3.44. Here β_l is the modified intensity and β is the original intensity of the zero-order beam. When the intensity of the zero-order beam is reduced by 50% (β_3), the image contrast dramatically increases in comparison to the initial value of the zero-order beam intensity(β_l). This is a very important improvement that can be used to increase the contrast and overall quality of the final PR image.

Figure 3.45 demonstrates an implementation of the neutral density (ND) filter in the zero-order arm in order to control its intensity independent of the diffracted, information, beams.

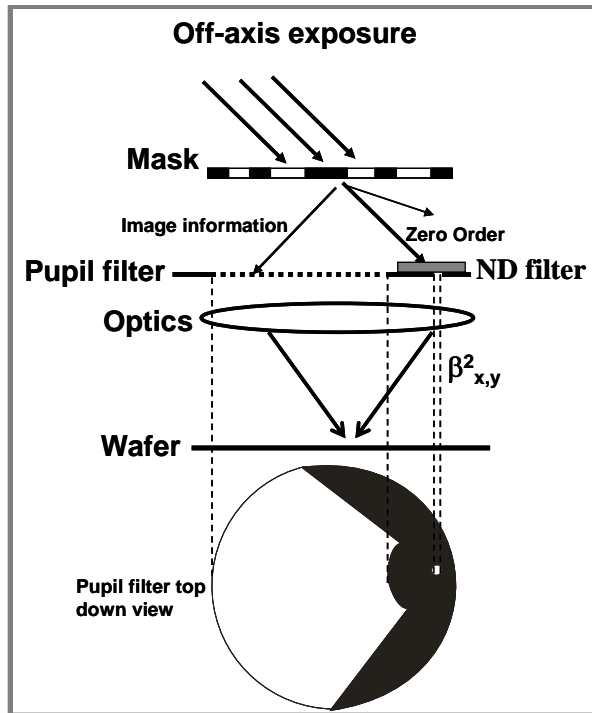


Fig. 3.45. Scheme of the implemented ND filter in the zero-order arm to control its intensity independent of the diffraction, information beams. Such control provides better contrast in the aerial image.

The suggested scheme of using PPF in the IIL experiment provides us with the robust tool to avoid redundancy in the frequency coverage, eliminate cross talk between the low and high order frequencies that will degrade the quality of the final image, and at last gives the independent control over the intensity of the zero-order beam, though increasing the contrast and fidelity of the final aerial image of the system.

In order to avoid generating optical aberrations in the beam path the ND filters, that controls the intensity of the zero order beam, were placed as indicated in Figure 3.26 at a plane where the high and low frequency beams are both well separated and collimated. This position allows the insertion of the ND filter in the low frequency (zero-order) beam without interfering with the high order beams.

Now we can use that “extra knob”, and repeat previous exposure for the CD of 90 nm.

Figure 3.46 shows a SEM of the developed PR patterns for the 3-exposure IIL for the 244

nm wavelength with 0.9 NA lens at the CD of 90-nm made with the ND attenuation of the zero-order beam. Zero order was attenuated by the factor of 2 in compared to its initial value. Here in Figure 3.46 a) has less exposure dose than b).

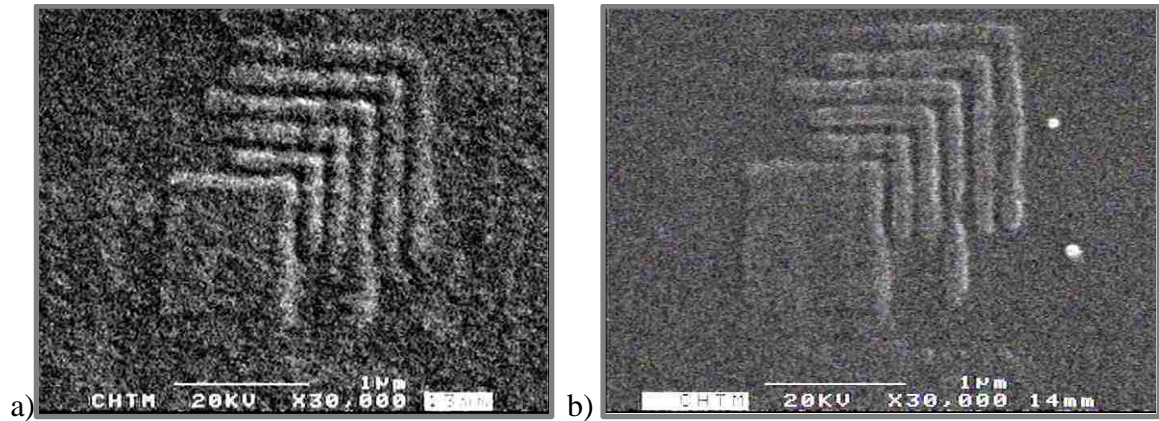


Fig. 3.46 SEMs of the PR pattern for the 3-exposure IIL for the 244 nm wavelength with 0.9 NA at the CD of 90 nm ($k_1 = 0.33$) with ND attenuation of the zero order beam by the factor of 2 in compare to its initial value. Exposure dose for pattern a) is less that for the pattern b)

As the exposure dose is increased the contrast of the image becomes better and the overall quality of the image becomes more acceptable. We can see some artifacts that are still present in the image but they are related strictly to the photoresist capability of resolving such small feature not to the optical system transfer capabilities. Next set of the SEMs pictures shows the patterns that were achieved under the same conditions as the previous set but with different exposure levels. This set is shown in the Figure 3.47.

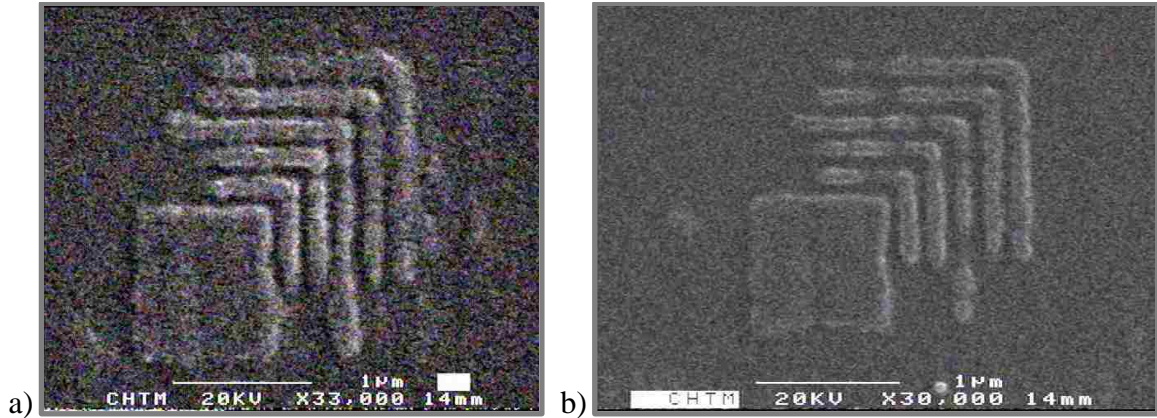


Fig. 3.47 SEMs of the PR pattern for the 3-exposure IIL for the 244 nm wavelength with 0.9 NA at the CD of 90 nm ($k_1 = 0.33$) with ND attenuation of the zero order beam in the high-frequency exposures. Exposure dose for pattern a) is less that for the pattern b).

The pattern on Fig.3.46 b) has the highest contrast of the image and the line/space ratio close to 1/1. Defects, in the form of the broken lines that are present on the transferred image are due to the photoresist issue of: undercutting, not sticking to well to the ARC layer and being pushed to and beyond it rated resolution limit. This PR is rated to have line/space resolution of 130 nm, which is significantly larger than the printed one. PROLITH simulation for this structure with ~ 90 nm CD does not shown any defects. The optical system has not shown problems in transferring image from the mask to the photoresist layer.

Comparing the pattern shown in the last two sets we can draw the conclusion that the use of the ND attenuation of the zero order beam in the high-frequency exposures has a positive impact on the achieving high contrast, robust and higher quality images. As predicted in the simulations, using ND attenuation improves the image contrast and helps bring line/space ratio close to the optimal 1/1 ration. However at the time we have not considered an impact on the phase change associated with the addition of the ND filter in the beam path. Investigation of this effect should be addressed in the future work.

As a demonstration of additional capacities of the optical system with implemented principals of IIL we show the SEM's of the developed PR pattern for 3-exposure IIL for the 244-nm wavelength with 0.9 NA lens at CD ~86-nm ($k_1 = 0.32$) on the Figure 3.48. This result was achieved without use of the ND attenuation.

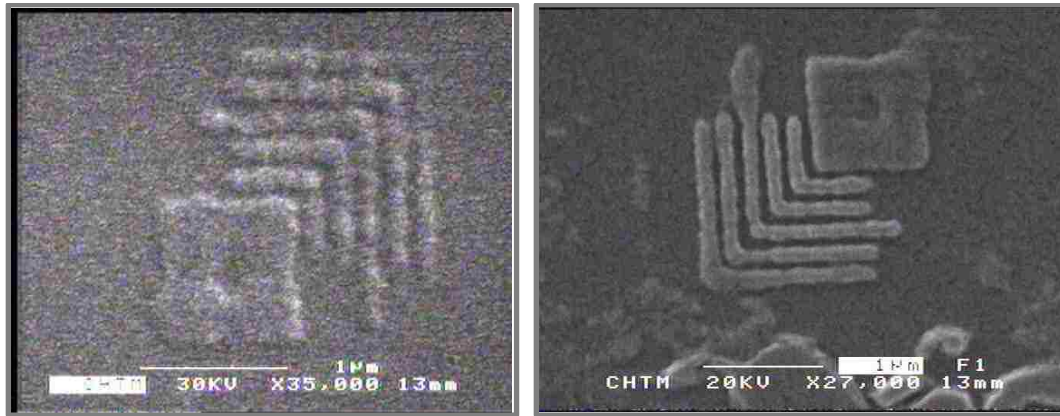


Fig. 3.48 SEM of developed PR for 3-exposure IIL for a CD of ~86-nm ($k_1 = 0.32$) at a 244-nm wavelength and 0.9 NA. Isolated lines and the square edge of the box are well defined, dense lines are cleared; defects of line fattening are due to exposure and photoresist issues not to the imaging system.

This result was achieved using the 1.9- μm CD chrome-on-glass mask (22 x reduction) without using any mask based RETs and indicates that we have demonstrated $\sim \lambda/3NA$ ultimate resolution of the optical system. Resulting image has well-defined line extensions (isolated lines); the dense lines are clear and well separated which indicates that the imaging system is performing well.

The hole in the middle of the square and the broadening of the isolated lines on the second pattern as well as the thinning of the outer line on the first pattern are due as much to exposure balancing and photoresist issues as to IIL imaging. By printing a box with dimensions of 10xCD, we are trying to cover a very wide frequency range. Looking closely to the aerial image of the 86 nm CD Manhattan pattern modeled in the PROLITH, we can see that there is a high intensity spot in the middle of the large box. This spot, highlighted in the black circle, is seen in the Figure 3.49.

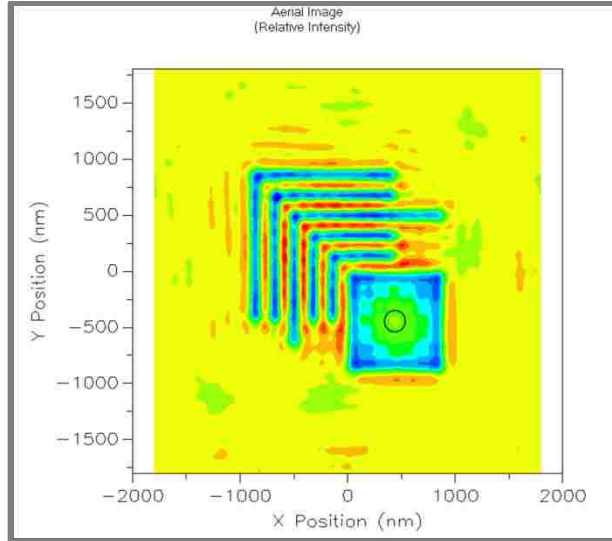


Fig. 3.49 PROLITH modeling of the 85 nm CD Manhattan patter demonstrating high intensity spot, highlighted in the black circle, in the middle of the large box. Intensity of the spot is comparable with intensity of the image in-between isolated lines.

Intensity of this middle of the box spot is comparable to the intensity that presents in-between the isolated lines. If we should decrease the size of the box to 5xCD we, decrease the spatial frequency range and illuminate the intensity spot in the middle of the box at it shown in the Figure 3.50.

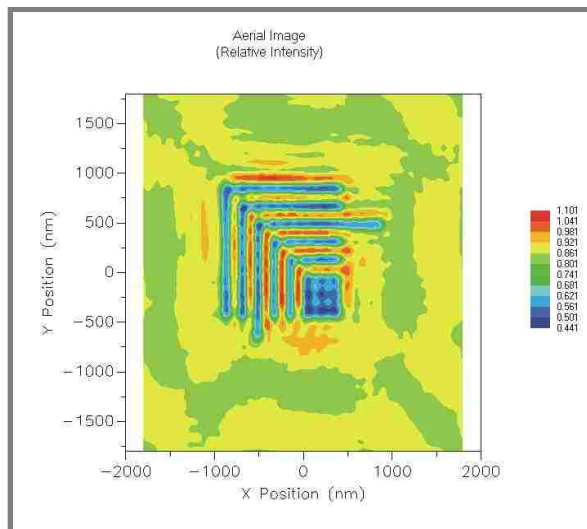


Fig. 3.50 PROLITH modeling of the 85 nm CD Manhattan patter with the box size of 5xCD, demonstrating no high intensity spot in the middle of the large box. Some exposure increase is required to fully clear the lines. But the intensities inside the box and the isolated line are compatible.

It is important to note that scaling this result to a 193-nm UV source along with an immersion 1.35 NA system will give us a direct access to the ~ 42 -nm half-pitch CD without the need for any mask based RETs. *The essential point is that robust imaging for a 42-nm half-pitch is available using IIL technique without any additional mask-based RETs.* That is roughly equivalent to the 32 nm industry microprocessor node (duty cycle 1:2). The implication is that IIL will allow minimization of the use of mask-based RETs, thereby dramatically reducing mask cost.

3.5 Conclusions

The 244-nm IIL test bed setup has demonstrated a capability of printing patterns with a CD compatible with industrial needs. We have achieved ~ 86 -nm half-pitch features ($\sim \lambda/3NA$) at a 244-nm wavelength with 0.9 NA without any additional mask-based RETs (PSM or OPC). We showed that the use of attenuation of the zero order beam in the high-frequency exposures give us an “extra knob” that plays a critical role in achieving robust, high quality image transfer into the photoresist. The enhanced image contrast allows reaching the desired 1/1 line/space ratio that was difficult to achieve at low k_1 without this added optimization

The important conclusion is that IIL can minimize the use of mask-based RETs, thereby reducing mask cost and improving cost of ownership (COO) for the 42-nm lithography node. This conclusion is supported by a recent simulation analysis [14] modeling the printing of similar pattern at the 45-nm half-pitch node using immersion ($NA\sim 1.3$) and a 193-nm source without the use of any mask-based RETs. Comparing the simulation results and the present PR patterns shows that IIL is capable of printing small patterns. The defects on the photoresist pattern are likely associated with photoresist and

exposure issues, rather than with the resolution. Image contrast is one of the largest issues facing lithography especially while printing at the resolution limit of the system introducing the ND filter attenuation scheme played a critical role in obtaining high contrast and high quality images. Control over the polarization was not critical at these dimensions but it will be increasingly important as the CDs are scaled further with the immersion techniques [28].

The size of the printed pattern can be scaled using the simple relation $CD \propto \lambda / NA$. In the present experiment we have achieved ~86-nm with a 244-nm source and a 0.9-NA lens. Switching to a 193-nm source and a 1.35 NA (for H₂O immersion) will lead directly to 59-nm half-pitch (hp) from 113-nm, 52-nm hp from 100-nm and ~42-nm hp from 86-nm – again without the need for any mask-based RETs such as PSM or OPC. Simulation predicts that the resolution of the present system possible can be extended to ~75-nm. This would scale to a ~ 39-nm half-pitch for the 193-nm immersion system.

As the future work we plan to optimize the exposure parameters for the 3-exposure ILL, continue experiments with the illumination scheme using ND attenuation of the zero order beams in the high frequency exposures and evaluate the resolution limit of the optical system. Attempt to print different patterns on the current setup such as via holes [28] is highly desirable. Additionally, apodization of the pupil plane filters can be used to further improve image quality, yet another “knob” [29]. Scaling to the 45-nm half-pitch node will require use of 193-nm source and an immersion exposure medium in order to achieve 1.15/1.3 NA systems. With this extended test bed, polarization and hyper-NA effects will be investigated.

3.6 References

- 1 G. E. Moore, *Electronics* **38**, 114-117 (1965).
- 2 G.E. Moore, *IEDM Technical Digest*, Washington, D.C., 11-13 (1975).
- 3 The National Technology Roadmap for Semiconductors, Published on the ITRS website, 2005 edition. (<http://public.itrs.net>)
- 4 *Lithography 2009: Overview of Opportunities*, by Yan Borodovsky, Intel senior fellow, Technology and Manufacturing Group, and director, Advanced Lithography, Intel Corporation, SEMICON West (2009).
- 5 S. H. Zaidi and S. R. J. Brueck, *Proc. SPIE* **3676**, 371 (1999).
- 6 S. R. J. Brueck, *There are No Fundamental Limits to Optical Lithography*, International Trends in Applied Optics, International Commission on Optics, pp. 85-110, SPIE Press (2002).
- 7 Bishcop, *J. Vac. Sci. Technol.* (2005).
- 8 B. J. Lin, *J. Microlith., Microfab. and Microsys.* **1**, 7 (2002).
- 9 J. H. Burnett and S. Kaplan, *Proc. SPIE* **5040**, 1742 (2003).
- 10 S. H. Zaidi and S. R. J. Brueck, *Jour. Vac. Sci. Technol.* **B11**, 658-666 (1993)
- 11 A. K. Raub and S. R. J. Brueck, *Proc. SPIE* **5040**, 667-678 (2003).
- 12 X. Chen and S. R. J. Brueck, *J. Vac. Sci. Technol.* **B16**, 3392-3397 (1998).
- 13 A. Frauenglass, S. Smolev, A. Biswas, S.R.J. Brueck, *Jour. Vac. Sci. Technol.* **22**, 3465-3469 (2004).
- 14 A. Biswas and S. R. J. Brueck, *J. Microlith., Microfab., and Microsys.* **3**, 35 (2004).
- 15 <http://www.rohmhaas.com/wcm/index.page>
- 16 <http://www.brewerscience.com/>

-
- 17 S. R. J. Brueck and X. Chen, *J. Vac. Sci. Technol.* **B17**, 908-921 (1999).
- 18 Goodman, J.W., "Introduction to Fourier Optics", McGraw-Hill, New-York, NY, (1968).
- 19 Mack C., "Fundamental Principles of Optical Lithography: The Science of Microfabrication", Wiley, England, (2007).
- 20 X. Chen and S. R. J. Brueck, *Opt. Lett.* **24**, 124-126 (1999).
- 21 E. Abbe, Beitrage zur Theorie des Mikroskops und der mikroskopischen Wahrnehmung, *Archiv fur mikroskopische Anatomie*, Vol. 9, p. 413-468, (1873).
- 22 H.H Hopkins, "The concept of partial coherence in optics", *Pross. of the Royal Society of London*, Series A, **208**, pp. 263-277, (1951).
- 23 C. Schwarz, PhD thesis, University of New Mexico, 2003.
- 24 S. Smolev, A. Biswas, A. Frauenglass, S. Brueck, "244-nm imaging interferometric lithography test bed", *Procc. SPIE* **6154**, (2006).
- 25 http://www.corning.se/semiconductoroptics/netnews/Spring_2002/CT_product.asp
- 26 X. Chen and S. R. J. Brueck, *J. Vac. Sci. Technol.* **B 17**, 921-929 (1999).
- 27 <http://polymers.msel.nist.gov/highlights/direct.html>
- 28 A. Biswas, A. Raub, S.R.J. Brueck, Y. A. Borodovsky, G.A. Allen , "Simulation of dense contact hole ($k_1=0.35$) arrays with 193-nm immersion lithography", **Procc. SPIE** 6154, (2006).
- 29 T. M. Tridhavee, B. Santhanam and S. R. J. Brueck, *Proc. SPIE* **5377**, 1544–1554 (2004).

Chapter 4 Gradient index optical lens ($\sim 1.55 \mu\text{m}$) using inhomogeneous metamaterials

4.1 Introduction

As we discussed earlier in the Chapter 1 since the first reports on negative index metamaterials (NIMs) [1,2], new classes of structures were developed to extend NIMs in the near-infrared (NIR) [3], and visible regions [4], where simple scaling of the structures used for radio frequencies (RF) is difficult. The research community is now turning towards the quest for the direct applications achievable with use of metamaterials. In the Chapter 2 of this dissertation we looked at phenomena of resonance hybridization in the NIM with the presence of absorber dipole in the dielectric material. This is a new effect in the field of metamaterials and is of interest from the fundamental and potentially application point of view.

A more practical application for NIM's that we are proposing is a gradient negative index optical lens for the telecom ($\sim 1.55 \mu\text{m}$) wavelengths created by the means of inhomogeneous metamaterials structures. Recently, Driscoll *et al* showed microwave focusing using a negative index gradient lens [5]. They used a Split Ring Resonator (SRR) based structure to obtain negative μ and stripes of metal wires in order to get negative ϵ . For the experiment a flat disk of thickness $d = 2$ mm and diameter $r = 300$ mm was created. Figure 4.1 shows graphical representation of his experimental NIM lens. This lens was designed to work at a wavelength of $\lambda = 29$ mm (10.3 GHz), making the ratio of the sample size to the wavelength r/λ equal to ~ 10 . Having such a small ratio

can lead to significant amount of diffraction at the edge of the sample thereby degrading the overall quality of the lens.

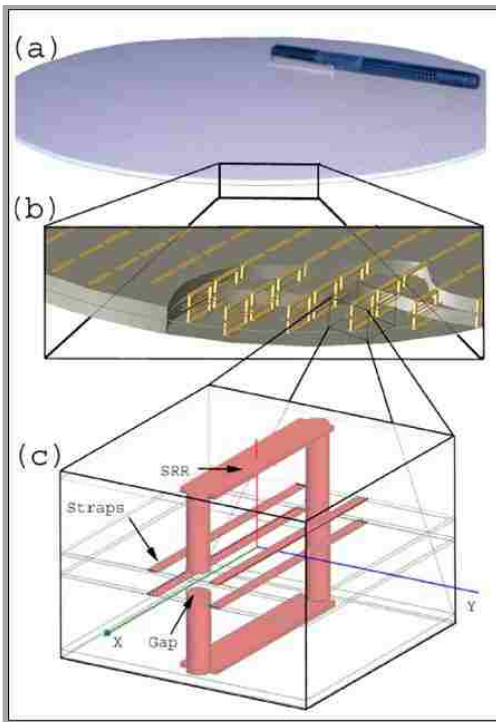


Fig. 4.1 Schematic representation of the flat disk negative index metamaterial lens for the microwave wavelengths created by Driscoll *et al.*

Gradient in negative index was ranged from $n_1 = -2.67$ at the edge of the lens disc to $n_2 = -0.97$ at the center of the lens. No information about single layer lens performance was provided in the publication but using existing information one could estimate that such lens will have focal length of 3.3 m and act as $f/11$ lens. However Driscoll showed that stacking multiple lens discs on the top of one another can be used to significantly decrease the f number. This improvement was approximately linearly proportional to the number of stacks. Fig. 4.2 shows RMS electric field amplitude for both modeling and experiment along the optical axis of GRIN lenses constructed of 4 – and 8- layers.

To the best knowledge of author, there have been no other reports of theoretical or experimental work in this direction, so we will compare our results demonstrated in this Chapter with the results reported by Driscoll.

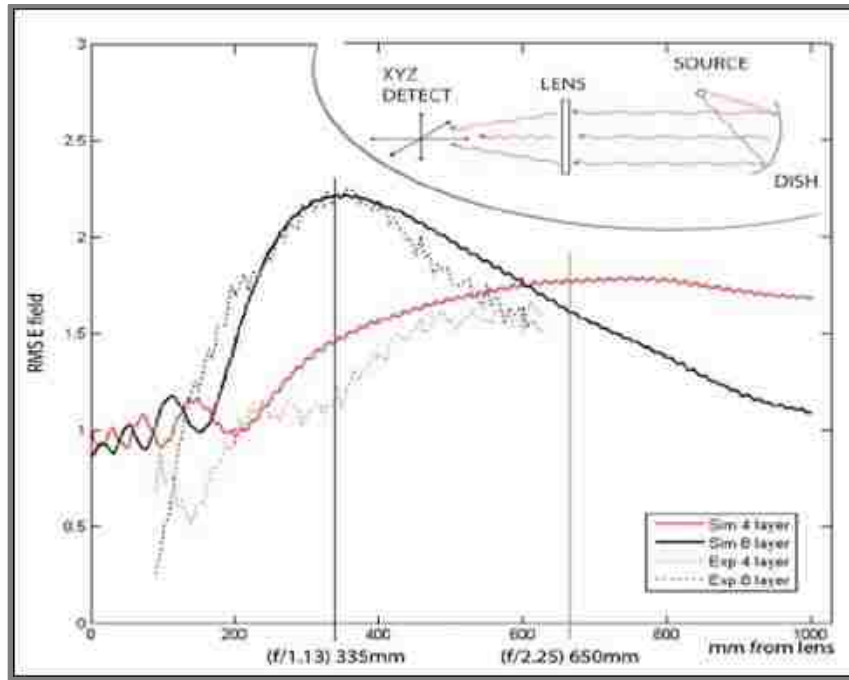


Fig. 4.2 RMS electric field amplitude for both modeling and experiment along the optical axis of grin lenses constructed of 4 (red) – and 8(black) - layers.

4.2 Design of proposed structure

Fishnet structures [6] have proven to be an excellent base for creating negative index metamaterials performing in the wide range of wavelengths from long wave infrared (LWIR) to the visible.

In 2005 Zhang *et al.* performed a theoretical parametric investigation of the fishnet structure [7]. Figure 4.3 shows top down and side views of the fishnet structure with indicated physical parameters. The variations in the optical properties were studied by the means of an RCWA simulation as the parameters were changed. A three layered

Au/Dielectric/Au structure was chosen as a base with the thicknesses of the layer to be 30/60/30 nm respectively. The index of the dielectric material between two gold films was taken to be 1.5. The pitches $a_x = a_y$ of the 2D structure with the resonance wavelength of $\sim 2 \mu\text{m}$, were fixed at 801 nm . Linewidth of the gratings d_x and d_y was systematically varied in the simulation to study the magnetic and electric response of the structure.

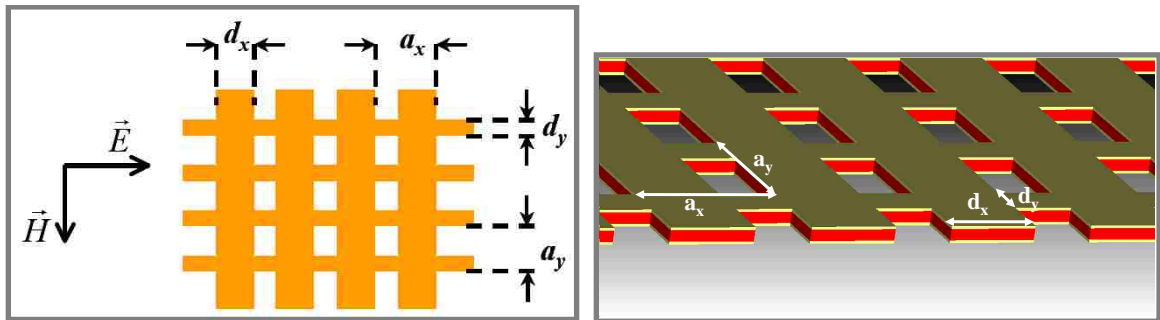


Fig. 4.3 Top down and a 3d side view of the fishnet based negative index metamaterial structure. geometrical parameters and direction of the E and B fields are indicated.

Negative index of refraction in the fishnet structure comes from two parts: the negative permittivity (ϵ) resulting from an array of thin metal wires parallel to the direction of electric field and the negative permeability (μ) resulting from a pair of finite-width metal stripes separated by a dielectric layer along the direction of the incident magnetic field. Figure 4.4 shows variations in the transmission (left) and effective refractive index (right) response of the fishnet structure as the result of the linewidth change.

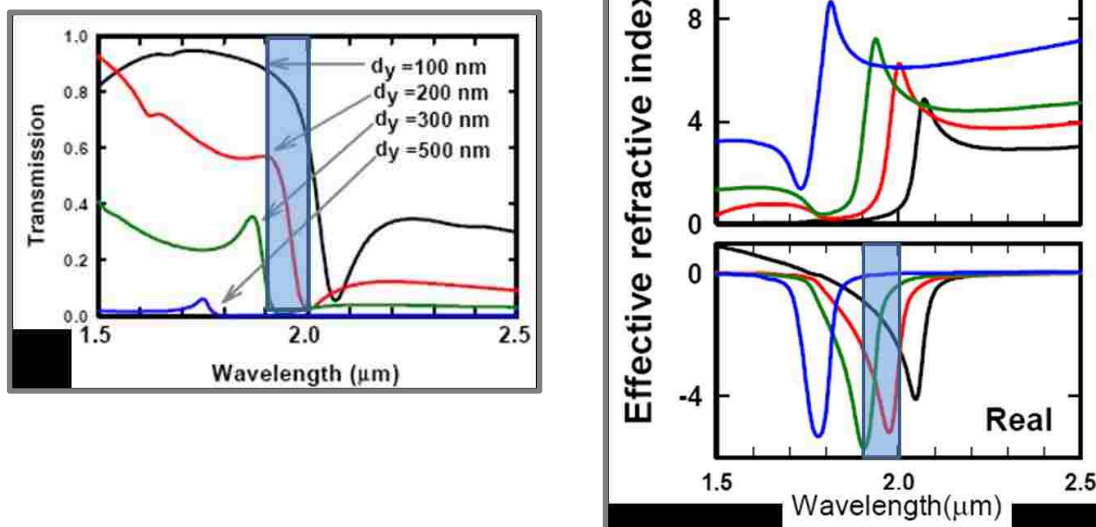


Fig. 4.4 Transmission (left) and effective refractive index response (right) of the fishnet structure to the changes of the d_y linewidth, while $d_x = 500$ nm and pitch a_x and a_y fixed at 801 nm.

It is clear that by changing the linewidth d_y of the metal wire we can control transmission and effective refractive index. With an increase of d_y , the resonance shifts to shorter wavelength, indicating an interaction between the electric and magnetic structures. The transmission decreases (reflection increases) as d_y becomes larger, due to metal polarizer effects. When d_y is small, the resonance is characterized by dip in the transmission, for increasing d_y a peak is clearly formed. Another degree of control is provided by manipulating linewidth d_x of the metal wire along B field.

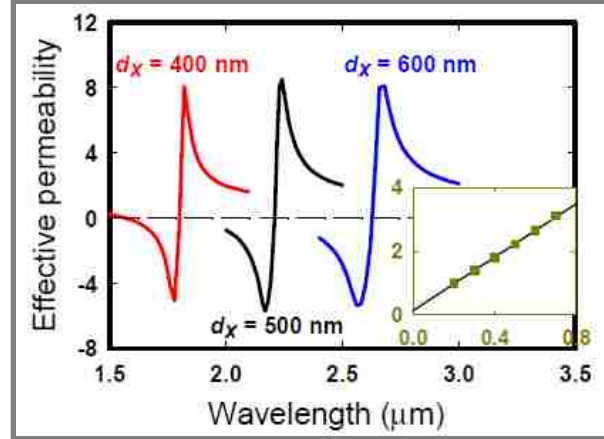


Fig. 4.5 Effective permeability of the fishnet for different Au linewidths. The inset shows the wavelength of the resonance peak versus the Au linewidth d_x in μm .

As shown in Figure 4.5, the resonance wavelength increases with the linewidth of Au gratings. This trend can be qualitatively explained by tracking the resonance of an equivalent L-C circuit; a wider grating corresponds to larger inductance and capacitance, which in turn leads to a larger resonance wavelength. Inset of Figure 4.5 shows that the resonance wavelength is linearly dependent on the Au linewidth d_x .

Studying this results give us an idea that having all those degrees of control we can independently vary ϵ and μ values at a fixed wavelength of the incident light by simply manipulating the widths of the metal wires along E and B fields, thereby shifting the resonance frequency of the NIM structure and changing the value of the effective refractive index $n = \sqrt{\mu\epsilon}$ while keeping small variations in the impedance $\eta = (\mu/\epsilon)^{1/2}$ and hence in the transmission. Here we force pitches a_x and a_y to be equal, however it will be of interest to consider the case where they are not equal. Studying of this case should be addressed in the future work. Having this set of “knobs” let us tune the physical size of the NIMs structure though create the gradient in the refractive index. Figure 4.6 shows RCWA calculated transmission and effective refractive index of the fishnet structure.

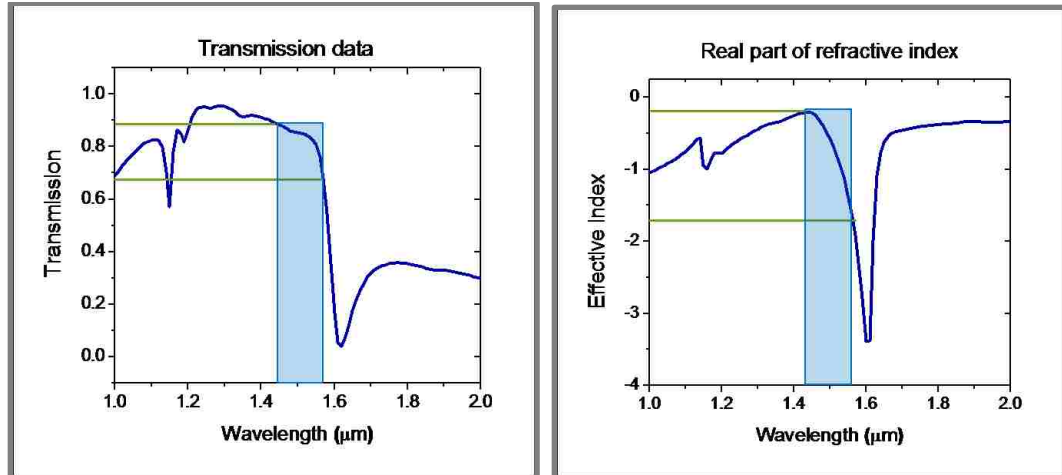


Fig. 4.6 RCWA calculated transmission and effective refractive index of the fishnet structure. highlighted regions shows available negative index gradient while retaining < 10% change in the transmission.

Highlighted region shows available gradient in the negative refractive index and corresponding change in the transmission response.

Also we can expand our range of controlled variables by manipulating the metal and the dielectric thicknesses in the fishnet structure.

In his work, Zhang used a fishnet structure with rectangular holes. We will use the same structure configuration since in 2007 Ku *et al* made an experimental comparison of NIM fishnets with circular, elliptical and rectangular openings [8]. Figure 4.7 shows transmission responses for structures with: a) circular, b) elliptical and c) rectangular holes. It is clear that assemblies b) and c) have a higher transmission which comes from better impedance matching between NIM structure and the incident media.

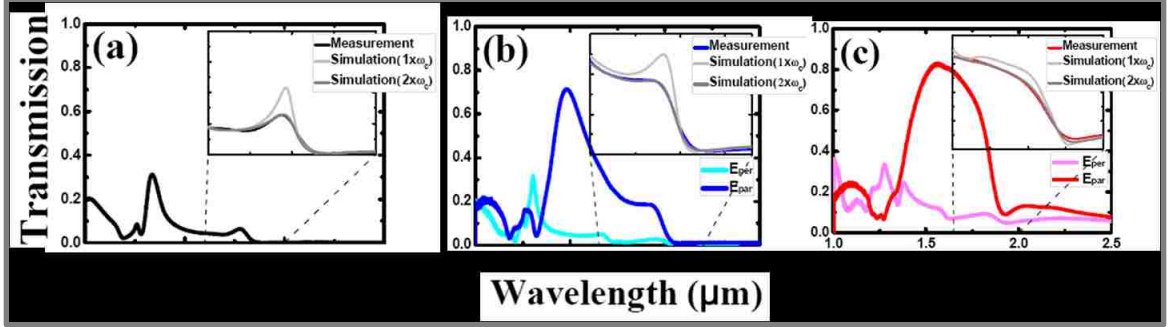


Fig. 4.7 Transmission response for the fishnet NIM structure with: a) circular, b) elliptical and c) rectangular holes. Better impedance matching between NIM structure and incident media results in higher transmission as it seen of the figure c).

That is particularly important since precise control and high transmission are required in order to utilize full available range of negative index of refraction.

Taking in the account all that was described above our proposed structure for the gradient negative index lens became a fishnet based metamaterial with the rectangular holes. For the practical implementation we chose a resonance wavelength to be at optical, telecom regime with $\lambda \sim 1.55 \mu\text{m}$. Au will be used as a metal in this structure and an appropriate chose of dielectric and all other parameters will be determined by a complex parametric study reported in the next section.

4.3 Parametric study and numerical modeling

4.3.1 RCWA numerical simulation

Rigorous coupled-wave analysis (RCWA) [9], [10], a commonly used algorithm to calculate the transmission and reflection of periodic structures, was used for the simulations. After the complex coefficients of transmission and reflection are obtained by RCWA, the effective refractive index, impedance, the figure of merit ($\text{FOM} = -\text{Re}(n)/\text{Im}(n)$), effective permittivity (permeability) can be extracted following known methods [11]. For all of the calculations, the incident light is normal to the surface and both the

incident and outgoing media are air. After the initial parametric analysis is done and the best structure for creation of the negative gradient index metamaterial lens is chosen addition set of simulations, where substrate layer was added, were performed. Multiple diffraction orders (12) are kept in both directions sufficient to converge very well for all simulated structures. The geometrical parameters of the structure are chosen in such way that NIM will have a resonant wavelength around 1.55 μm . Dielectric layer between the gold films is a parametric variable chosen to be a Sapphire, later different dielectric materials were evaluated (silicon nitride, α -silicon). The line-width and the pitch of the 2D grating in the theoretical simulation were systematically varied to study combined magnetic and electric response of the structure. The present calculations are for a single three-layer structure on the glass substrate and the dimension of the metamaterial is just the physical thickness of the three layers. A simple Drude model for the metal permittivity was used, which is a good approximation to experiment values in the near-IR. The permittivity is given as $\epsilon_{Au} = 1 - \omega_p^2 / [\omega(\omega + i\gamma\omega_c)]$, where ω_p (plasma frequency) = 1.37×10^{16} Hz and ω_c (bulk scattering frequency) = 4.1×10^{13} Hz [12]. And γ is a parameter to account for additional scattering in the thin, multi-domain films as well as for any random sample inhomogeneity.

4.3.2 Parametric study and simulation results

We are going to perform a parametric study on a three – layered Au/Dielectric/Au fishnet structure. All of the explored parameters are listed in following:

- Variation in pitch and CD sizes of the fishnet structure in orthogonal directions;
- Different dielectric materials: Sapphire, Si_3N_4 and α -Si;
- Different metal layer thickness (30-, 60- nm) for a given sample;

- Different dielectric layer thickness (60-, 120-, 180- nm) for a given sample;
- Variation in metal/dielectric/metal combined layer thickness for a given sample;

At the end of this parametric study we will be evaluating the results from each parameter in the form of maximum achievable phase shift

$$\theta_{phase} = 2\pi \frac{\Delta n L}{\lambda} \quad (4.1)$$

where Δn is a negative index gradient, L is a total thickness of the fishnet structure and λ is the resonance wavelength. We will limit variation in the transmission response of the fishnet structure across the sample to $\sim 10\%$. This will provide us with necessary base for evaluating the final results and selecting best structure for the gradient negative index metamaterial lens.

Before we start out study let us see at first what effect on the response of the fishnet structure has the change of the dielectric layer. Figure 4.8 shows transmission and effective refractive index curves calculated using RCWA for 3 different dielectrics: Sapphire ($n = 1.74$), Si_3N_4 ($n = 2.4$) and α -silicon ($n = 3.4$).

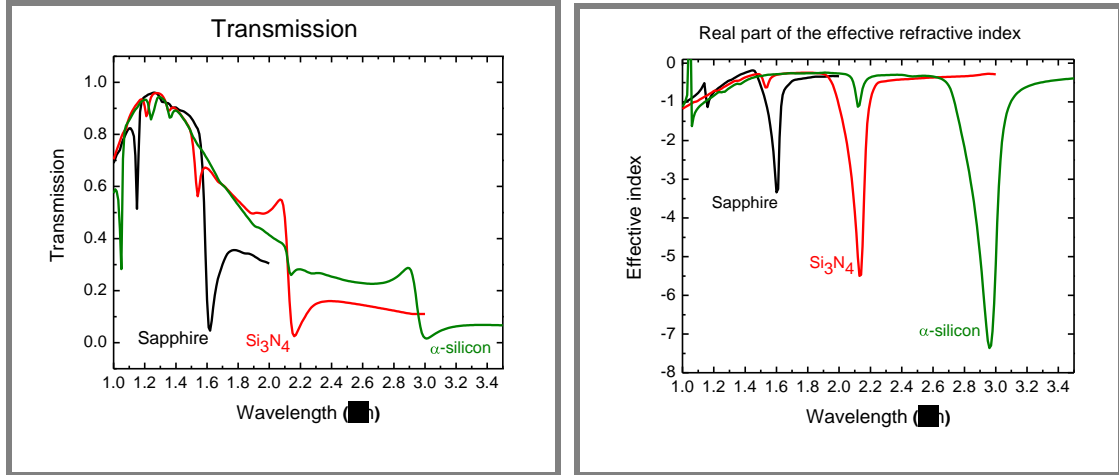


Fig. 4.8 RCWA calculated transmission (left) and effective refractive index (right) fishnet responses for different dielectric materials. Parameters of the fishnet are: layer thicknesses 30/60/30 nm; pitch 645 nm in both directions; CD;s: x – 332 nm, y – 100 nm.

Physical parameters of the fishnet structure were identical for all dielectrics and are listed in the caption to the figure. One can see that increasing the index of the dielectric material in the fishnet shifts the resonance to the longer wavelengths. Compensation mechanism of decreasing the pitch and CD should be implemented in order to bring the resonance wavelength back to $\sim 1.55 \mu\text{m}$. That means having higher dielectric index leads to having smaller linewidth and pitch of the structure.

4.3.2.1 Evaluation of different dielectrics for fixed layers thicknesses

In this section we will look at 3 different dielectrics. We will fix layer thicknesses of the fishnet structure at 30/60/30 nm, Au/dielectric/Au respectively. Our maximum transmission variation for a given sample will be restricted to $\sim 10\%$ this way limiting the maximum available gradient in the index, as it was shown in the Figure 4.6.

Starting with the sapphire ($n = 1.74$) as dielectric we will get the following achievable phase shift. Figure 4.9 shows transmission and effective refractive gradient in index as the pitch and CD of the fishnet structure is tuned.

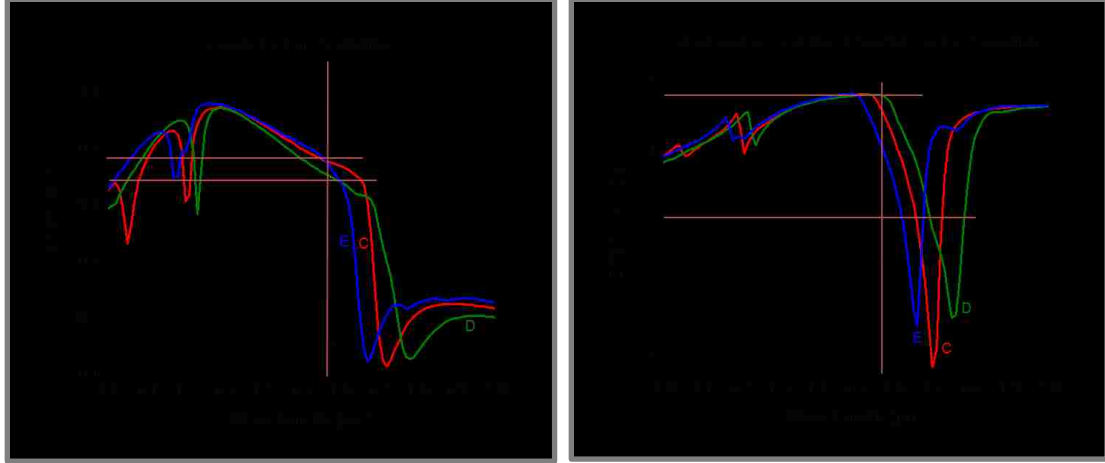


Fig. 4.9 Achievable gradient in negative refractive index (right) and corresponding transmission variation (left) for the sapphire based fishnet structure. $\lambda_{\text{resonance}} = 1.56 \mu\text{m}$; $\Delta n = 1.8$; $\Delta t = 0.1$; total thickness of the structure $L = 120 \text{ nm}$. $\Delta n L / \lambda = 0.138$

For this fishnet configuration with Sapphire as a dielectric maximum achievable phase shift from Eqn. 4.1 is equal to 0.276π . While the maximum transmission is ~ 0.75 with $\Delta T = 0.1$ across the sample. Physical parameters (pitch and CD) for each individual curve are given in the Table 4.1

Table 4.1 List of physical parameters (pitch and cd) for each individual curve for the sapphire based fishnet grin lens. Fishnet structure responses are shown on Figure 4.9.

Curve	Pitch $a_x, a_y, \text{ nm}$	CD $d_x, \text{ nm}$	CD $d_y, \text{ nm}$
B	645	322	100
C	670	348	125
D	685	355	132
E	660	338	115

If one shall compare resonance wavelength and pitch for the individual curve it become obvious that for larger pitch the resonance wavelength shifts towards longer wavelengths.

Switching dielectric material to Silicon Nitride ($n = 2.4$) gives different transmission and effective refractive index curves shown on the Figure 4.10.

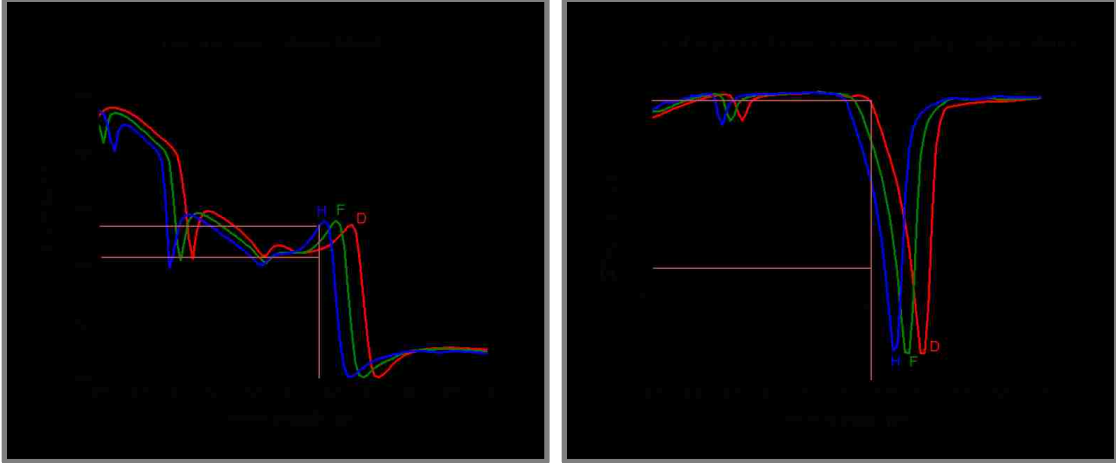


Fig. 4.10 Achievable gradient in negative refractive index (right) and corresponding transmission variation (left) for the Si_3N_4 based fishnet structure. $\lambda_{\text{resonance}} = 1.57 \mu\text{m}$; $\Delta n = 3.2$; $\Delta t = 0.1$; total thickness of the structure $L = 120 \text{ nm}$. $\Delta n L / \lambda = 0.244$

For this fishnet configuration with Silicon Nitride as a dielectric maximum achievable phase shift from Eqn. 4.1 is equal to 0.489π . While the maximum transmission is ~ 0.52 with $\sim \Delta T = 0.1$ across the sample. Physical parameters (pitch and CD) for each individual curve are given in the Table 4.2

Table 4.2 List of physical parameters (pitch and cd) for each individual curve for the Si_3N_4 based fishnet grin lens. Fishnet structure responses are shown on Figure 4.10.

Curve	Pitch a_x, a_y , nm	CD d_x , nm	CD d_y , nm
B	475	237	100
D	510	255	100
F	497	248	100
H	487	243	100

Higher index dielectric material in the fishnet structure produces large phase shift but at the expense of a lower maximum transmission.

Last dielectric material that we will check will be α -silicon ($n = 3.4$). Corresponding transmission and effective refractive index response of the fishnet structure with this material are shown on the Figure 4.11.

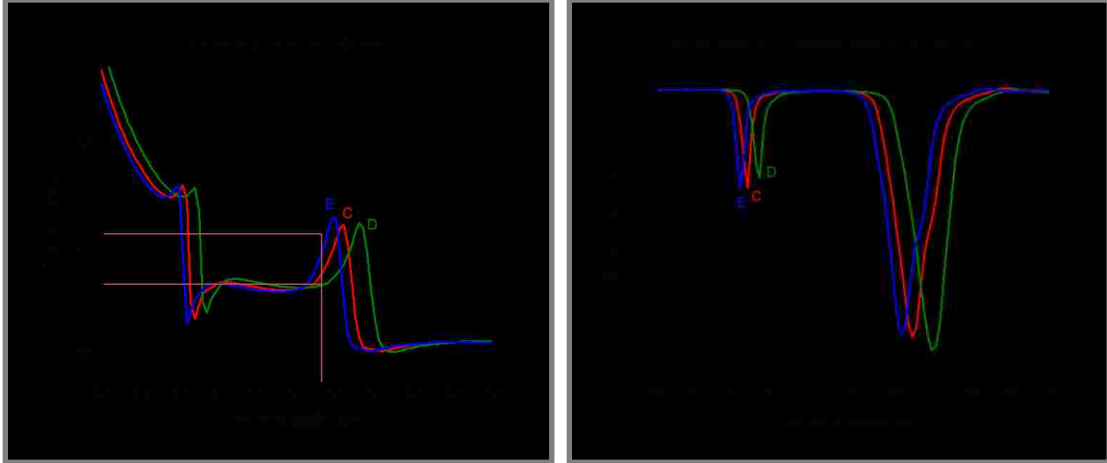


Fig. 4.11 Achievable gradient in negative refractive index (right) and corresponding transmission variation (left) for the α -silicon based fishnet structure. $\lambda_{\text{resonance}} = 1.56 \mu\text{m}$; $\Delta n = 3.2$; $\Delta t = 0.1$; total thickness of the structure $L = 120 \text{ nm}$. $\Delta n L / \lambda = 0.246$

Maximum phase shift of 0.492π is achievable in this configuration. However, the maximum transmission for the structure is only ~ 0.24 . Physical parameters (pitch and CD) for each individual curve are given in the Table 4.3

Table 4.3 List of physical parameters (pitch and cd) for each individual curve for the α -silicon based fishnet grin lens. Fishnet structure responses are shown on Figure 4.11.

Curve	Pitch a_x, a_y , nm	CD d_x , nm	CD d_y , nm
B	345	172	100
C	355	177	100
D	365	182	100
E	350	175	100

After evaluating three dielectrics we see that not only the achievable phase shift but also the maximum transmission in each case is different. Meaning that when the decision for selecting the best structure for GRIN lens is made, maximum transmission for the sample has to be taken in consideration. Table 4.4 shows results of the evaluating different dielectric materials for the fixed thickness of the fishnet structure.

Table 4.4 Results of the evaluating different dielectric materials for the fishnet structure with fixed thicknesses of metal/diel/metal (30/60/30 nm). Table shows maximum transmission and achievable phase shift for each case.

Dielectric Material		Sapphire	Si ₃ N ₄	α - silicon
Transmission, T	L	0.65	0.42	0.14
	H	0.75	0.52	0.24
Index, <i>n</i>	L	-2	-3.5	-3.6
	H	-0.2	-0.3	-0.4
Available phase shift, φ		0.276 π	0.489 π	0.492 π

The conclusion that can be drawn from this table is that Silicon Nitride is the best dielectric material to use for the creation of the negative GRIN metamaterial lens when the thicknesses of the metal/dielectric structure are fixed at 30/60/30 nm respectively. Fact that this design will work only for the fixed resonance wavelength needs to be remembered.

In the next section we will investigate what happens if the thickness of the dielectric material layer is changed.

4.3.2.2 Evaluation of different dielectric layer thickness for individual dielectric

In this section we will investigate the effect of changing the thickness of the dielectric layer for each dielectric. Thickness for both metal layers is fixed at 30 nm. Process of evaluation starts with comparing transmission and effective refractive index

responses for the structures with fixed physical parameters (pitch and CD) but with different dielectric index.

Figure 4.12 shows plots of transmission and effective n for 3 different dielectric layer thicknesses of the Sapphire: 60 -, 120-, and 180- nm.

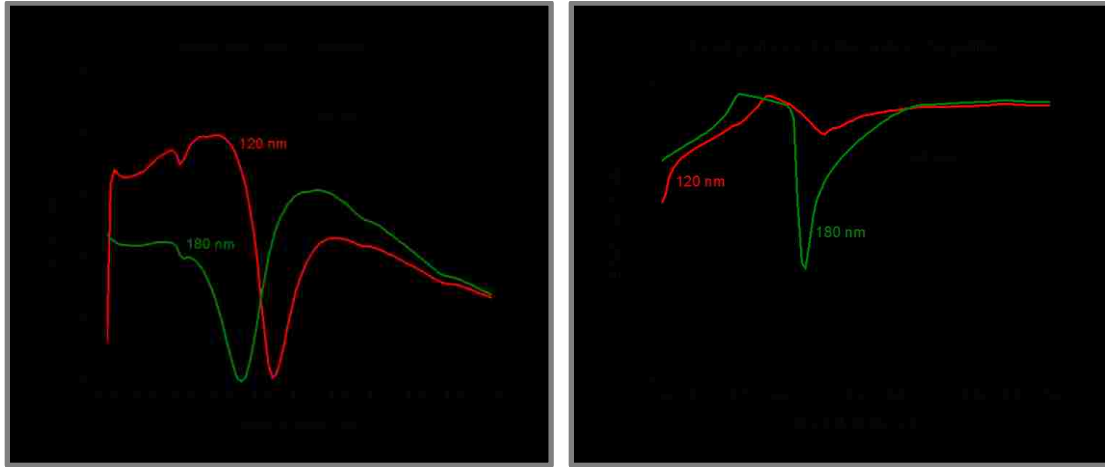


Fig. 4.12 Transmission and effective n responses of the sapphire based fishnet with 60 -, 120 -, and 180 - nm worth of dielectric.

Close study of the plots reveals that no improvement of the achievable phase shift can be reached. So no further investigations for this dielectric were performed.

Looking at Silicon Nitride based fishnet structure response, shown on the Figure 4.13; we observe much more room for the future improvements.

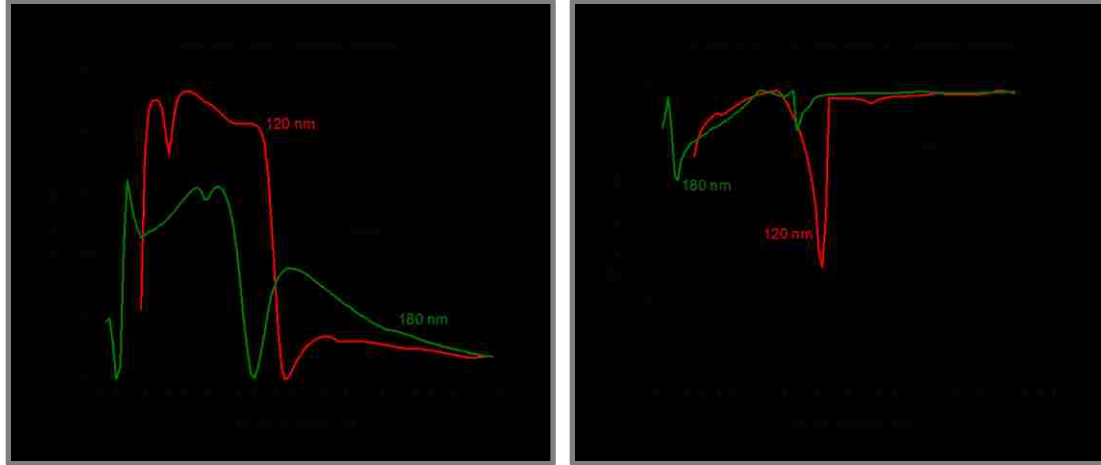


Fig. 4.13 Transmission and effective n responses of the Si_3N_4 based fishnet with 60 -, 120 -, and 180 - nm thickness of dielectric.

Increasing the thickness of the dielectric layer by the factor of 2 (from 60 nm to 120 nm) gave a significant increase in the maximum transmission (from ~ 0.54 to ~ 0.82) and at the same time decreased max negative index value (from -4.5 to -3.3). Resonant wavelength also shifted (from $\sim 1.6 \mu\text{m}$ to $\sim 1.4 \mu\text{m}$). Further increase in thickness, up to 180 nm does not give us any noticeable improvement. Next step will be to shift the resonance wavelength back to our desired value of $1.55 \mu\text{m}$. This shift can be achieved by increasing the pitch and CD sizes of the fishnet structure. Figure 4.14 shown transmission and effective refractive index response of the fishnet, where the resonance wavelength is at $1.55 \mu\text{m}$. and the thickness of the dielectric layer is 120 nm.

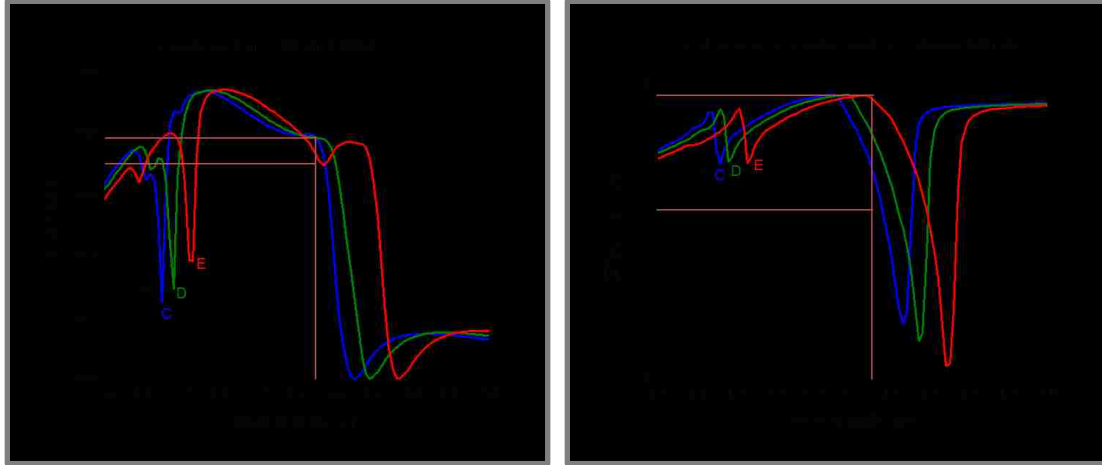


Fig. 4.14 Achievable gradient in negative refractive index (right) and corresponding transmission variation (left) for the silicon nitride based fishnet structure. $\lambda_{\text{resonance}} = 1.55 \mu\text{m}$; $\Delta n = 1.51$; $\Delta t = 0.08$; total thickness of the structure $L = 180 \text{ nm}$. $\Delta n L / \lambda = 0.175$

Maximum phase shift of 0.351π is achievable in this configuration. By increasing the thickness of the dielectric layer the maximum achievable phase shift is decreased (0.351π vs. 0.489π) in comparison to the case where the thickness was only 60 nm. But we have significantly improved the maximum transmission value for the structure (~ 0.79 vs. ~ 0.52). Physical parameters (pitch and CD) for each individual curve are given in the Table 4.5.

Table 4.5 List of physical parameters (pitch and cd) for each individual curve for the silicon nitride based fishnet grin lens. Fishnet structure responses are shown on Figure 4.14.

Curve	Pitch a_x, a_y , nm	CD d_x , nm	CD d_y , nm
B	545	272	100
C	555	277	100
D	570	285	100
E	595	297	100

Same evaluation procedure is applied to the α - silicon based fishnet structure. Figure 4.15 shows transmission and effective n responses for 3 thicknesses: 60 -, 120 -, and 180 - nm.

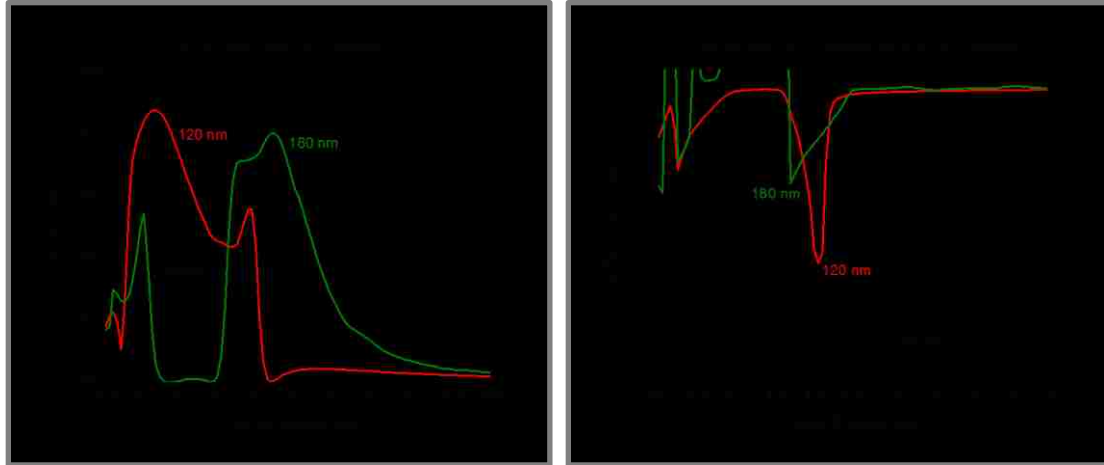


Fig. 4.15 Transmission and effective n responses of the α - silicon based fishnet with 60 -, 120 -, and 180 - nm thickness of dielectric.

We see that increased thickness shifted the resonance wavelength to the shorter region, maximum transmission value has increased from ~ 0.25 to ~ 0.55 , and the negative index value has dropped from -4.6 to ~ -3.3 . But because we have improved the maximum transmission value we will investigate this case more closely. However, increasing the dielectric layer thickness to 180 nm has not shown any advantages. Figure 4.16 shows the transmission and effective refractive index responses for the α - silicon base fishnet structure with the dielectric layer thickness of 120 nm.

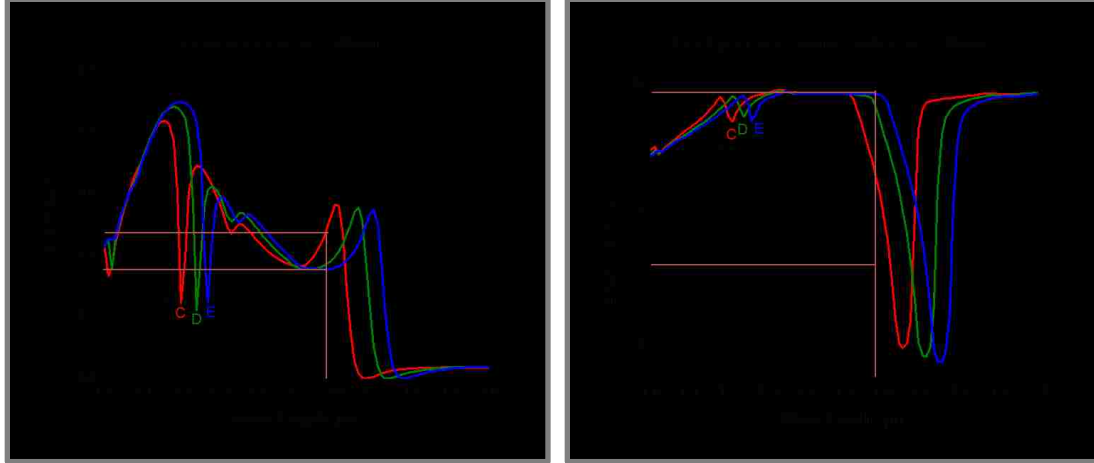


Fig. 4.16 Achievable gradient in negative refractive index (right) and corresponding transmission variation (left) for the α - silicon based fishnet structure. $\lambda_{\text{resonance}} = 1.58 \mu\text{m}$; $\Delta n = 2.6$; $\Delta t = 1.2$; total thickness of the structure $L = 180 \text{ nm}$. $\Delta n L / \lambda = 0.296$

Maximum phase shift from Eqn. 4.1, of 0.592π is achievable in this configuration. By increasing the thickness of the dielectric layer we have gained in the maximum achievable phase shift (0.492π vs. 0.592π) in comparison to the case where the thickness was only 60 nm. Also we have significantly improved the maximum transmission value for the structure (~ 0.47 vs. ~ 0.24). Physical parameters (pitch and CD) for each individual curve are given in the Table 4.6.

Table 4.6 List of physical parameters (pitch and cd) for each individual curve for the α - silicon based fishnet grin lens. Fishnet structure responses are shown on Figure 4.16.

Curve	Pitch a_x, a_y , nm	CD d_x , nm	CD d_y , nm
B	395	197	100
C	405	202	100
D	420	210	100
E	430	215	100

Now we can combine the results of this study in one table and draw a conclusion.

Table 4.7 represents the final result of this section evaluation study.

Table 4.7 Best results of the evaluating different dielectric layer thicknesses for 3 dielectrics. Table shows maximum transmission and achievable phase shift for each case.

Dielectric Material		Sapphire	Si ₃ N ₄	α - silicon
Thickness of layer, nm		120	120	120
Transmission, T	L	n/a	0.71	0.37
	H	n/a	0.79	0.47
Index, <i>n</i>	L	n/a	-1.64	-2.75
	H	n/a	-0.13	-0.15
Available phase shift, ϕ		n/a	0.489 π	0.592 π

Results of this evaluation study suggests that for the fishnet metamaterial structure with the layers thicknesses of 30/120/30 nm and Silicon Nitride as dielectric it is possible to achieve phase shift of 0.489π with 0.79 maximum transmission.

Next section will be dedicated to evaluation of fishnet structural response as total combined thickness of three layers: metal/dielectric/metal is changed.

4.3.2.3 Evaluation of different total combined thickness of 3 layers for individual dielectric

Total thicknesses of 3 layers will be changed in the following manner: at first metal layer thickness will be increased from 30 nm to 60 nm, bringing total structural thickness L to 180 nm; then dielectric layer thickness will be increased from 60 nm to 120 nm, making L to be 240 nm. We will start as usual with the Sapphire dielectric. And

as a first step transmission and effective n response of the fishnet structure will be investigated. Figure 4.17 shows transmission and effective refractive index calculated for 3 different total thicknesses: 120 -, 180 -, and 240 – nm.

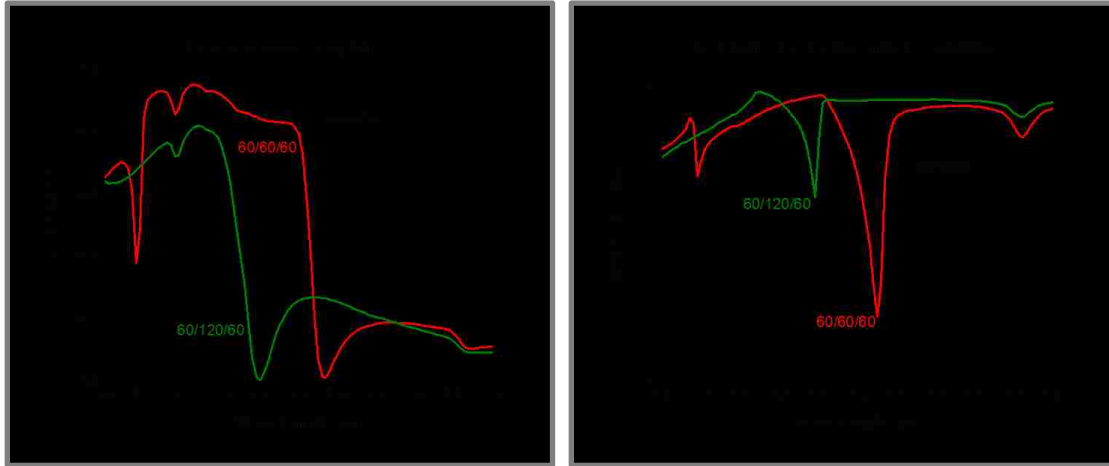


Fig. 4.17 Transmission and effective refractive index response of the fishnet structure with the sapphire dielectric material. Plots show calculated curves for 3 different total combined layer thicknesses.

From the plots shown above one can see that increase in total thickness of layer leads to some decrease in maximum values of negative effective index and transmission. However it seems to be of interest to investigate achievable phase shift for the total layer thickness of 180 nm. Figure 4.18 shows calculated transmission and effective refractive index curves for the described above fishnet structure.

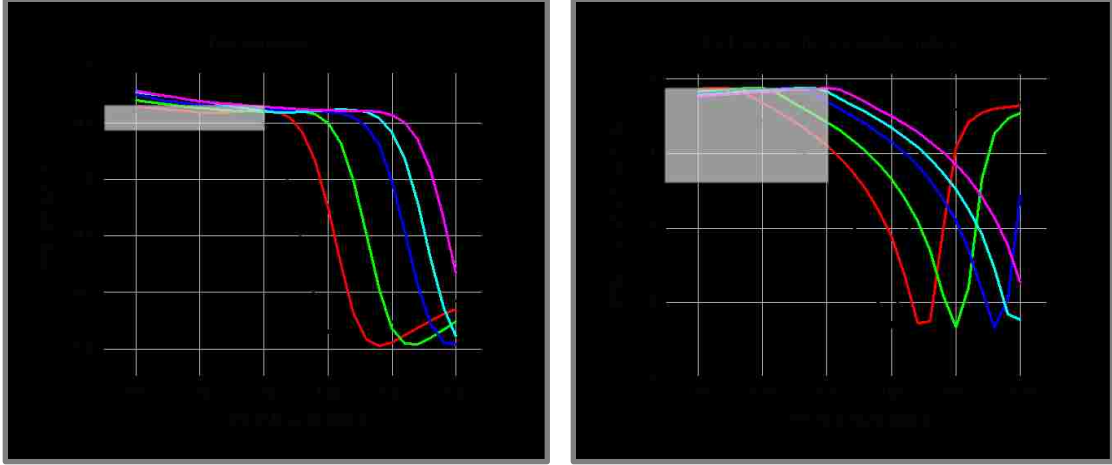


Fig. 4.18 Achievable gradient in negative refractive index (right) and corresponding transmission variation (left) for the sapphire based fishnet structure. $\lambda_{\text{resonance}} = 1.55 \mu\text{m}$; $\Delta n = 1.25$; $\Delta t = 0.06$; total thickness of the structure $L = 180 \text{ nm}$. $\Delta n L / \lambda = 0.145$

Maximum phase shift of 0.290π is achievable for this configuration with maximum transmission of ~ 0.85 . Table 4.8 lists all geometrical parameters used to generate each curve (from left to right) within calculated sets. Shaded regions on the Figure 4.18 represents amount of accessible Δn and corresponding variation in transmission across the NIM structure for the fixed $\lambda_{\text{resonant}} = 1.55 \mu\text{m}$.

Table 4.8 List of physical parameters (pitch and cd) for each individual curve for the sapphire based fishnet grin lens. Fishnet structure responses are shown on Figure 4.18.

Curve	Pitch (a_x, a_y), nm	CD d_x , nm	CD d_y , nm	n	L, nm
1	665	332	100	1.75	180
2	677	338	100	1.75	180
3	689	345	100	1.75	180
4	701	350	100	1.75	180
5	709	355	100	1.75	180
6	715	357	100	1.75	180

We have obtained a high transmission value for this sample of ~ 0.85 .

In the case of the Silicon Nitride increase in the total combined layer thicknesses produces following response of the fishnet structure that can be observed on the Figure 4.19.

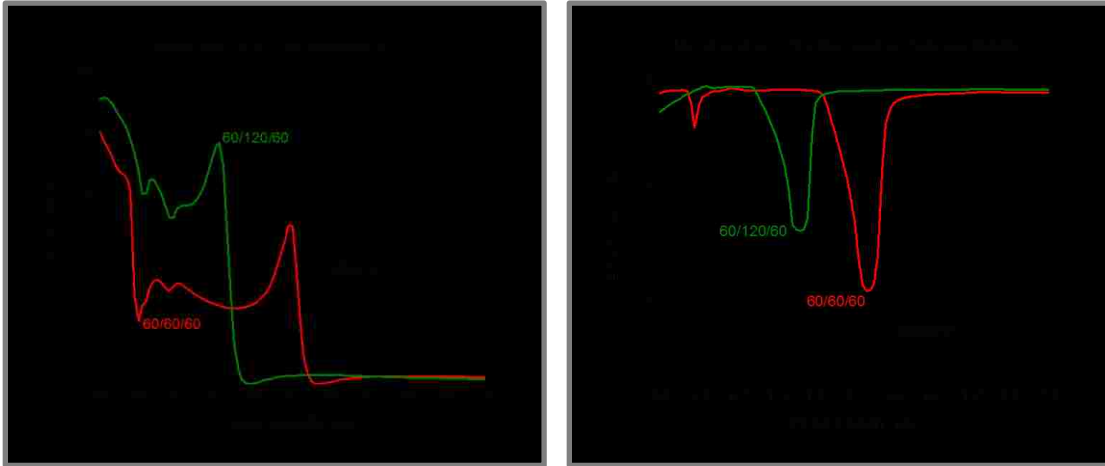


Fig. 4.19 Transmission and effective refractive index response of the fishnet structure with the Si_3N_4 dielectric material. Plots show calculated curves for 3 different total combined layer thicknesses.

For the total thickness of one functional layer (metal/dielectric/metal) of 240 nm we have observed high transmission value. So this thickness was chosen to be investigated as a base for the GRIN metamaterial lens. Figure 4.20 shows calculated transmission and effective refractive index curves, where shaded region demonstrated achievable Δn and corresponding variation in transmission ΔT .

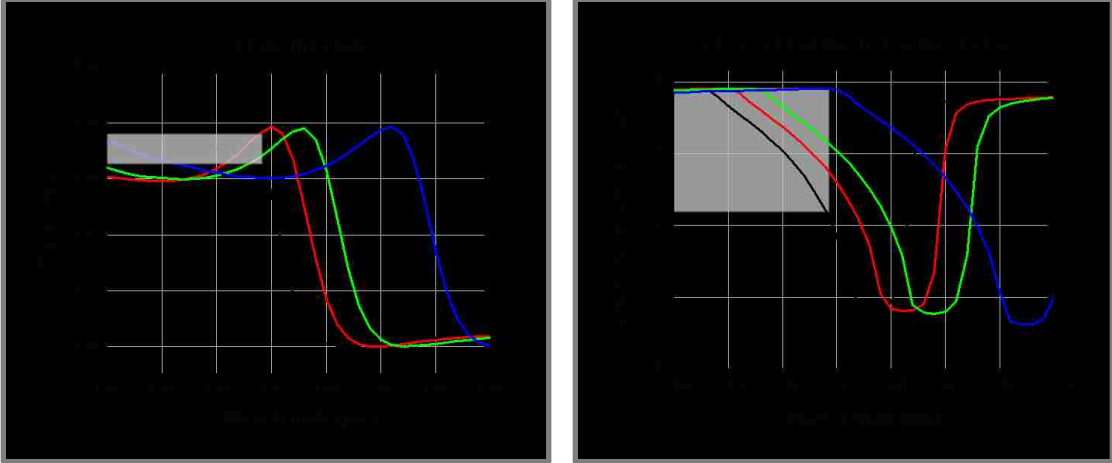


Fig. 4.20 Achievable gradient in negative refractive index (right) and corresponding transmission variation (left) for the silicon nitride based fishnet structure. $\lambda_{\text{resonance}} = 1.54 \mu\text{m}$; $\Delta n = 1.67$; $\Delta t = 0.1$; total thickness of the structure $L = 240 \text{ nm}$. $\Delta n L / \lambda = 0.260$

Maximum phase shift of 0.520π is achievable for this configuration with maximum transmission of ~ 0.76 . This is the largest phase shift and the highest transmission value observed for the fishnet GRIN metamaterial lens based on the Silicon Nitride dielectric. Table 4.9 lists all geometrical parameters used to generate each curve (from left to right) within the calculated set.

Table 4.9 List of physical parameters (pitch and cd) for each individual curve for the Si_3N_4 based fishnet grIn lens. Fishnet structure responses are shown on Figure 4.20.

Curve	Pitch (a_x, a_y), nm	CD d_x , nm	CD d_y , nm	n	L, nm
1	555	277	100	2.4	240
2	565	282	100	2.4	240
3	575	287	100	2.4	240
4	605	302	100	2.4	240

Last case in this section is the evaluation of the α - silicon based structure. Figure 4.21 shows transmission and effective refractive index variations as the total combined

layer thicknesses have been changed. For this plot physical parameters of the fishnet structures were changed in such way that the resonance wavelength will remain fixed.

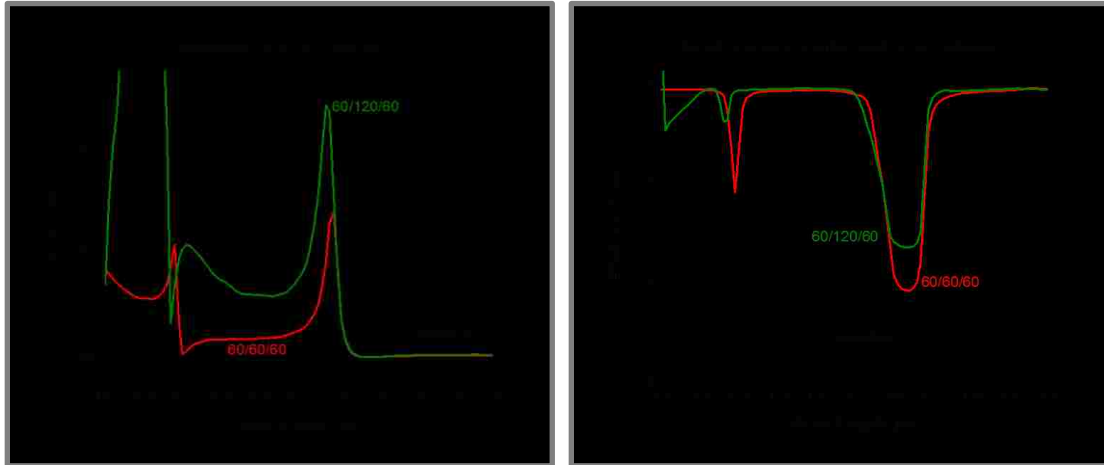


Fig. 4.21 Transmission and effective refractive index response of the fishnet structure with the α - silicon dielectric material. Plots show calculated curves for 3 different total combined layer thicknesses. Physical parameters of the fishnet structure for each curve were changed so that the resonance wavelength will remain fixed.

Curve representing response from the structure with the total layer thickness of 240 nm looks to be promising; however such a rapid change in the transmission around the resonance can be a possible cause for some complications. Figure 4.22 shows calculated transmission and effective refractive index variations for the GRIN metamaterial lens with the resonance wavelength at $\sim 1.58 \mu\text{m}$.

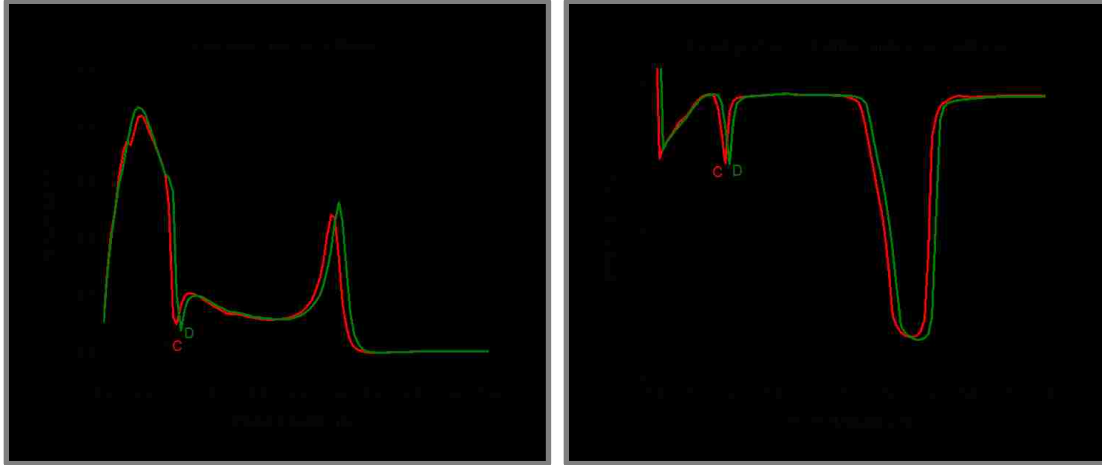


Fig. 4.22 Achievable gradient in negative refractive index (right) and corresponding transmission variation (left) for the α - silicon based fishnet structure. $\lambda_{\text{resonance}} = 1.58 \mu\text{m}$; $\Delta n = 0.8$; $\Delta t = 0.07$; total thickness of the structure $L = 240 \text{ nm}$. $\Delta n L / \lambda = 0.121$

Penalty for a rapid change in the transmission response is small achievable variation in the effective refractive index leading to a maximum phase shift from Eqn. 4.1 of 0.243π with transmission peaking at ~ 0.47 . Physical parameters used to generate presented curves can be found in the Table 4.10

Table 4.10 List of physical parameters (pitch and cd) for each individual curve for the α - silicon based fishnet grin lens. Fishnet structure responses are shown on Figure 4.22.

Curve	Pitch (a_x, a_y), nm	CD d_x , nm	CD d_y , nm	n	L, nm
B	410	205	100	3.4	240
C	415	207	100	3.4	240
D	420	210	100	3.4	240

Now we can collect results of the optimization study for this section and summers them in the Table 4.11.

Table 4.11 Best results of the evaluating different total combined layer thicknesses for 3 dielectrics. Table shows maximum transmission and achievable phase shift for each case.

Dielectric Material		Sapphire	Si ₃ N ₄	α - silicon
L (total), nm		180	240	240
Transmission, T	L	0.79	0.66	0.4
	H	0.85	0.76	0.47
Index, <i>n</i>	L	-1.37	-1.79	-2.5
	H	-0.12	-0.12	-1.7
Available phase shift, ϕ		0.290 π	0.520 π	0.243 π

Final results suggests that the Silicon Nitride based fishnet structure with the total thickness of 3 layers of 240 nm is the best structure for creating the GRIN metamaterial lens with achievable phase shift of 0.520π and maximum sample transmission of 0.76.

In the next section we will evaluate fishnet structural response as thickness of metal layer is decreased.

4.3.2.4 Evaluation of different metal layer thickness for individual dielectric

For the standard fishnet metamaterial structure starting metal layer thickness was 30 nm. We will investigate effect of decreasing the layer thickness down to 20 nm. Smaller metal thicknesses will not be considered as it would not be enough to generate

negative permeability μ , which is necessary for creating negative index response in the structure.

As before we will start our evaluation exercise with the Sapphire based dielectric material. Figure 4.23 shows transmission and effective refractive index for the fishnet with 20 nm thick metal layers.

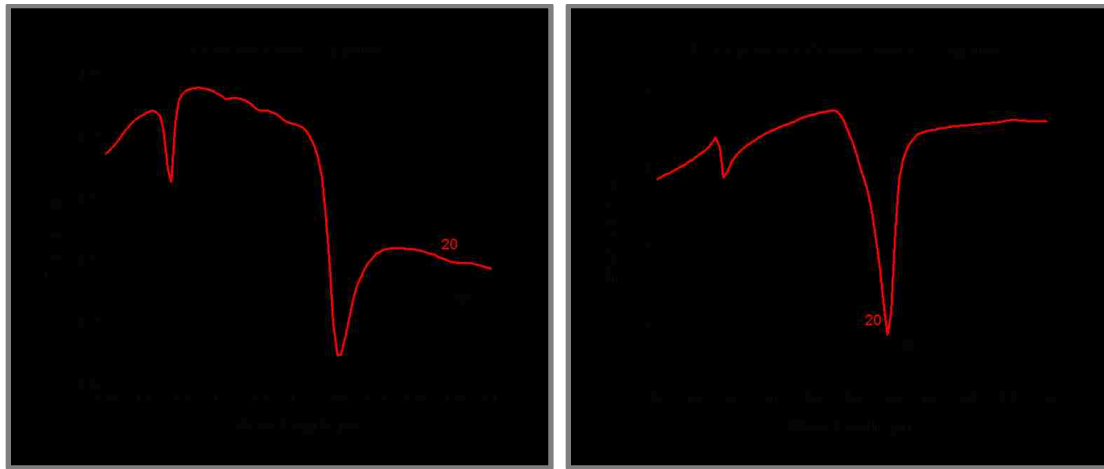


Fig. 4.23 Transmission and effective refractive index response of the fishnet structure with the sapphire dielectric material. Plots show calculated curves for 2 different metal layer thicknesses.

One can see that decreasing the metal layer thickness did not produce much change in the response of the fishnet structure, so no further investigations were performed for this case.

For the Silicon Nitride and α - silicon dielectric only plots for available Δn and corresponding ΔT will be presented. Figure 4.24 shows transmission and effective refractive index response of the fishnet structure with metal layer thickness of 20 nm and Silicon Nitride as a dielectric material. Resonance wavelength is at $\sim 1.56 \mu\text{m}$.

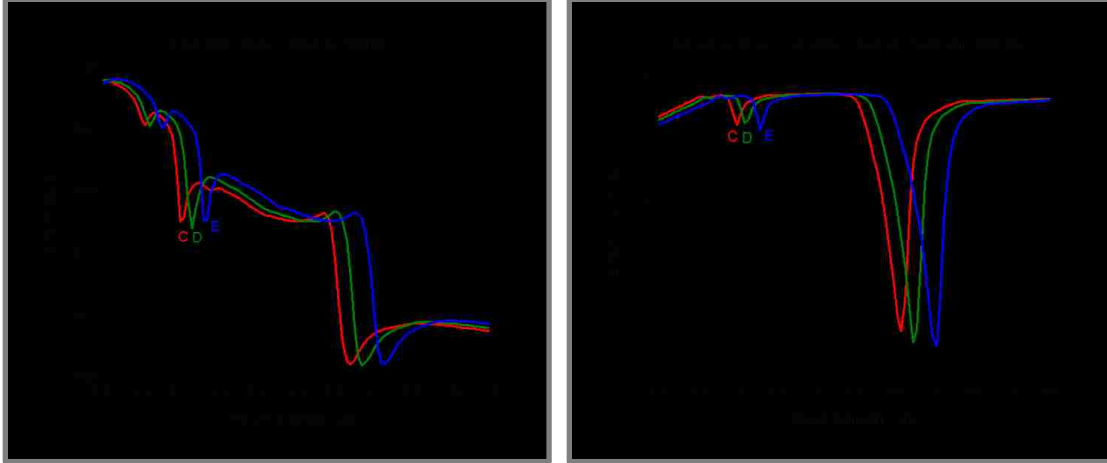


Fig. 4.24 Achievable gradient in negative refractive index (right) and corresponding transmission variation (left) for the silicon nitride based fishnet structure. $\lambda_{\text{resonance}} = 1.56 \mu\text{m}$; $\Delta n = 2.54$; $\Delta t = 0.05$; total thickness of the structure $L = 100 \text{ nm}$. $\Delta nL/\lambda = 0.163$

Maximum phase shift of 0.326π is achievable for this configuration with maximum transmission of ~ 0.52 . Table 4.12 lists all geometrical parameters used to generate this calculated set.

Table 4.12 List of physical parameters (pitch and cd) for each individual curve for the Si_3N_4 based fishnet grin lens. Fishnet structure responses are shown on Figure 4.24.

Curve	Pitch (a_x, a_y), nm	CD d_x , nm	CD d_y , nm	n	L, nm
B	450	225	100	2.4	100
C	460	230	100	2.4	100
D	470	235	100	2.4	100
E	485	242	100	2.4	100

Next figure shows α - silicon based fishnet metamaterial response for the metal layer thickness of 20 nm.

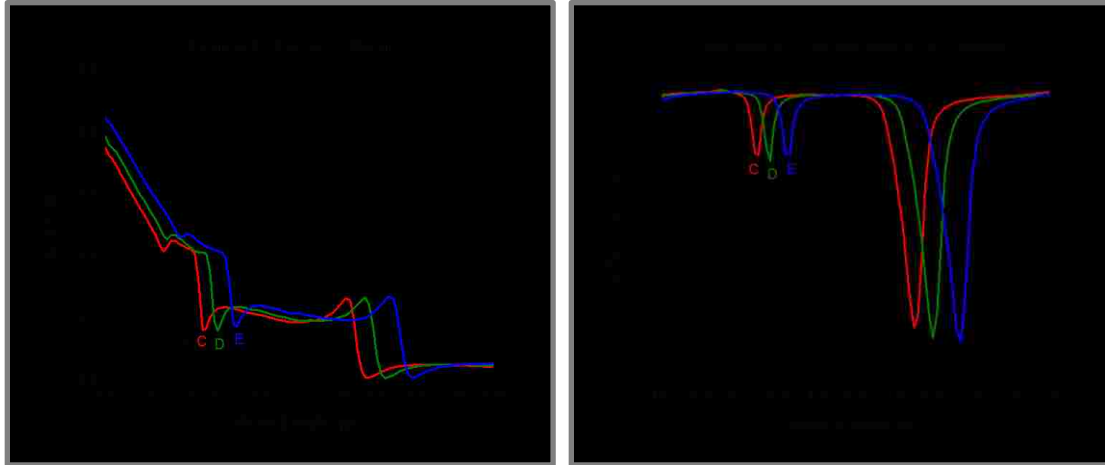


Fig. 4.25 Achievable gradient in negative refractive index (right) and corresponding transmission variation (left) for the α - silicon based fishnet structure. $\lambda_{\text{resonance}} = 1.59 \mu\text{m}$; $\Delta n = 3.66$; $\Delta t = 0.03$; total thickness of the structure $L = 100 \text{ nm}$. $\Delta n L / \lambda = \mathbf{0.230}$

In this case maximum achievable phase shift was 0.460π and the maximum transmission value was on the order of ~ 0.23 . Table 4.13 shows list of all geometrical parameters that were used to generate this set of curves.

Table 4.13 List of physical parameters (pitch and cd) for each individual curve for the α - silicon based fishnet grin lens. Fishnet structure responses are shown on Figure 4.25.

Curve	Pitch (a_x, a_y), nm	CD d_x , nm	CD d_y , nm	n	L, nm
B	325	162	100	3.4	100
C	335	167	100	3.4	100
D	345	172	100	3.4	100
E	360	180	100	3.4	100

We will finalize the result of this section parametric evaluation and present them in the Table 4. 14, where the maximum transmission value and achievable phase shift are indicated.

Table 4.14 Best results of the evaluating different metal layer thickness for 3 different dielectrics. Table shows maximum transmission and achievable phase shift for each case.

Dielectric Material		Sapphire	Si ₃ N ₄	α - silicon
L (total), nm		100	100	100
Transmission, T	L	n/a	0.46	0.2
	H	n/a	0.52	0.23
Index, <i>n</i>	L	n/a	-2.82	-3.92
	H	n/a	-0.28	-0.26
Available phase shift, φ		n/a	0.326 π	0.460 π

Comparing obtained results from this exercise to the results in previous section one can see that we did not get desired improvement in the combination of phase shift and maximum transmission from decreasing the thicknesses of the metal layers.

In the last section we will evaluate response of the fishnet structure as the thickness of the dielectric layer is decreased. This will be the last parametric study after which final conclusions can be made.

4.3.2.5 Evaluation of effect of decreasing the dielectric layer thickness for individual dielectric

In this section we will evaluate the response of the fishnet metamaterial structure as the thickness of the dielectric layer will be decreased. Original thickness of the dielectric was 60 nm and here we will check values of 40 -, and 20 – nm.

Sapphire based fishnet metamaterial structural transmission and effective refractive index responses are shown on the Figure 4.26.

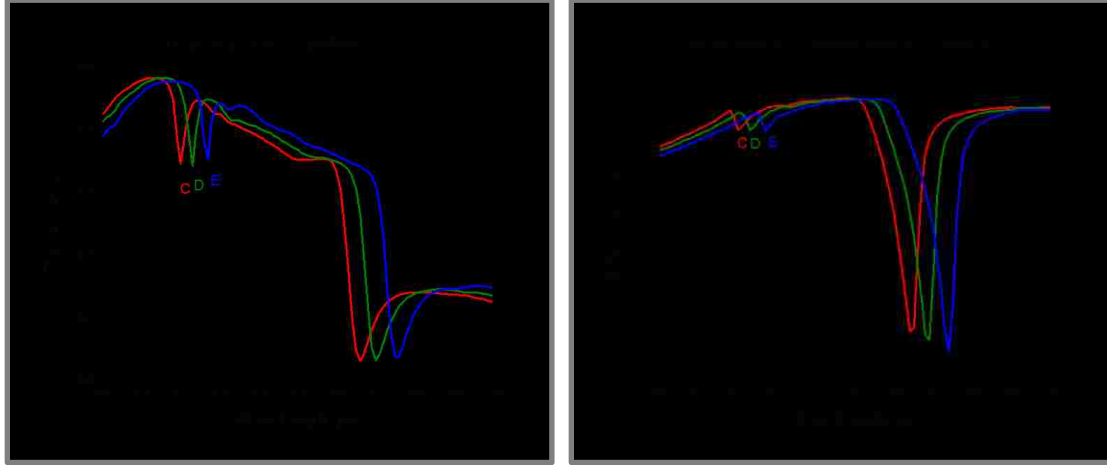


Fig. 4.26 Achievable gradient in negative refractive index (right) and corresponding transmission variation (left) for the sapphire based fishnet structure. $\lambda_{\text{resonance}} = 1.58 \mu\text{m}$; $\Delta n = 1.96$; $\Delta t = 0.8$; total thickness of the structure $L = 100 \text{ nm}$. $\Delta n L / \lambda = 0.124$

The maximum achievable phase shift of 0.248π and the maximum transmission of ~ 0.72 can be obtained for the thickness of Sapphire dielectric material of 40 nm. Table 4.15 shows list of all geometrical parameters that were used to generate this set.

Table 4.15 List of physical parameters (pitch and cd) for each individual curve for the sapphire based fishnet grin lens. Fishnet structure responses are shown on Figure 4.26.

Curve	Pitch (a_x, a_y), nm	CD d_x , nm	CD d_y , nm	n	L, nm
B	590	295	100	1.75	100
C	600	300	100	1.75	100
D	615	307	100	1.75	100
E	635	317	100	1.75	100

For the Sapphire base structure decreasing or increasing (see section 4.3.2.2) the dielectric layer thickness did not give us any noticeable improvement over the case where the dielectric layer thickness was unchanged.

When dielectric material in the fishnet structure is changed to the Silicon Nitride and the thickness of the dielectric layer is set to 40 nm transmission and effective refractive index responses has the following form shown on the Figure 4.27.

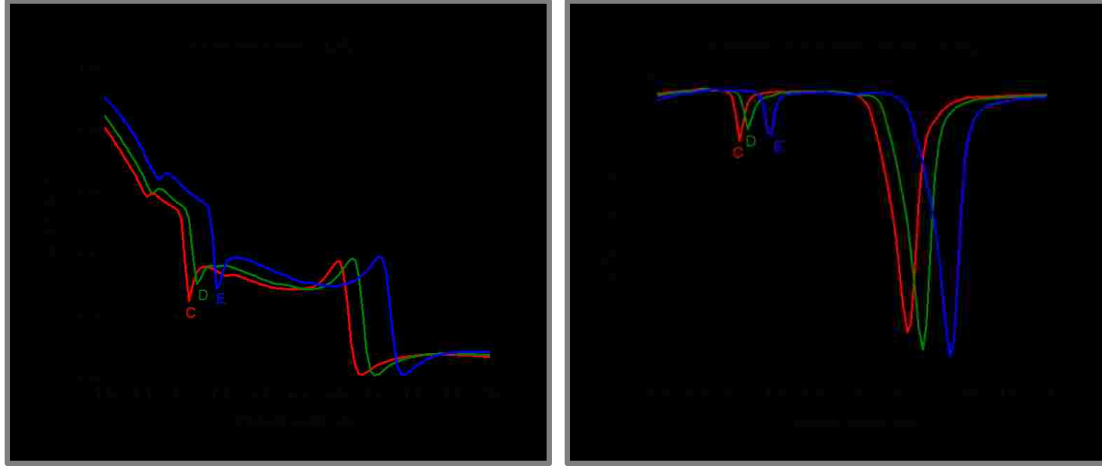


Fig. 4.27 Achievable gradient in negative refractive index (right) and corresponding transmission variation (left) for the Si_3N_4 based fishnet structure. $\lambda_{\text{resonance}} = 1.58 \mu\text{m}$; $\Delta n = 2.81$; $\Delta t = 0.7$; total thickness of the structure $L = 100 \text{ nm}$. $\Delta n L / \lambda = 0.178$

Phase shift from Eqn. 4.1 of 0.356π and the maximum transmission of ~ 0.37 can be obtained for the 40 nm worth of Silicon Nitride. The geometrical parameters that were used to generate this set can be found in the Table 4.16.

Table 4.16 List of physical parameters (pitch and cd) for each individual curve for the sapphire based fishnet grin lens. Fishnet structure responses are shown on Figure 4.27.

Curve	Pitch (a_x, a_y), nm	CD d_x , nm	CD d_y , nm	n	L, nm
B	435	217	100	2.4	100
C	445	222	100	2.4	100
D	455	227	100	2.4	100
E	475	237	100	2.4	100

And the final responses from the fishnet structure with α - silicon as a dielectric material with the thickness of 40 - and 20 - nm are shown on the Figure 4.28.

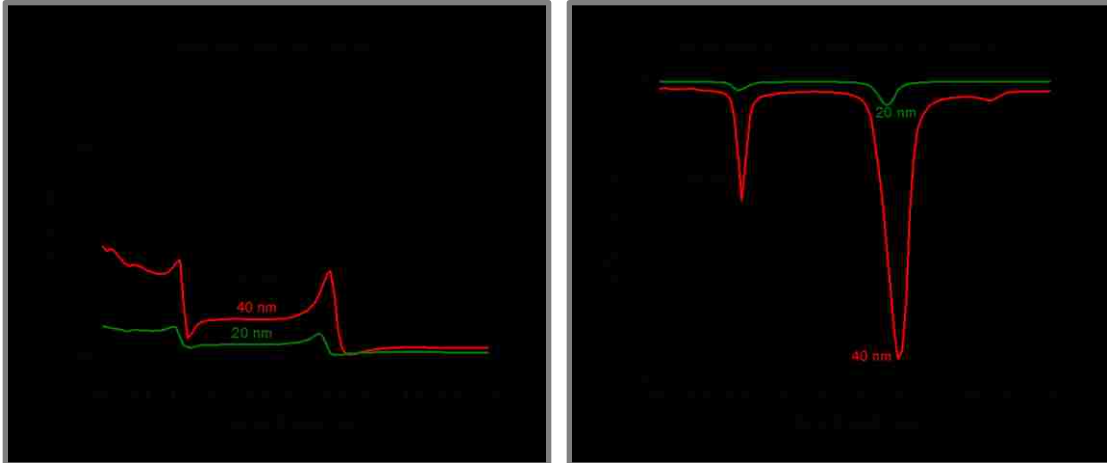


Fig. 4.28 Transmission (left) and effective refractive index (right) responses for the fishnet metamaterial with α - silicon dielectric and 3 different thicknesses.

The decrease in the dielectric layer thickness leads to a rapid decrease in the maximum transmission value. Because of that no further improvement for this structure can be achieved.

Table 4.17 represents the results of the evaluation study for the decreased thickness of the dielectric layer. Maximum transmission and achievable phase shift are indicated.

Table 4.17 Best results of the evaluating different dielectric layer thickness for 3 dielectrics. Table shows maximum transmission and achievable phase shift for each case.

Dielectric Material		Sapphire	Si ₃ N ₄	α - silicon
L (total), nm		100	100	100
Transmission, T	L	0.64	0.30	n/a
	H	0.72	0.37	n/a
Index, <i>n</i>	L	-2.22	-3.09	n/a
	H	-0.26	-0.28	n/a
Available phase shift, ϕ		0.248 π	0.356 π	n/a

This section concludes our numeric parametric study. Now we can summarize our results by looking at each individual dielectric material and choosing the best configuration based on the maximum transmission and achievable phase shift. This will be discussed in the following section.

4.3.2.6 Summary and the results of the numeric parametric study

As it was mentioned earlier we can summarize the results of our parametric study by looking at each individual dielectric and picking the best configuration based on the maximum achievable phase shift and transmission value. Those best picks will be brought together in the Table 4.18.

Thicknesses of metal/dielectric/metal layer will be indicated in this table as well. Proposed designed of the experiment will be discussed in details later, but here we need to mention that the Imaging Interferometric Lithography (IIL) setup will be used to

produce the sample. Details about this IIL setup can be found in the Chapter 3. One of the limiting factors of this setup is its field of view, which is only $\sim 100 \times 100 \mu\text{m}$. That means that for the fixed resonance wavelength at $\sim 1.55 \mu\text{m}$ we can generate a sample with $\sim (64 \times 64)\lambda^2$ area. Having the information about the area of the sample and phase shift that can be generated across it we can estimate the focal length of our GRIN metamaterial lens. That estimate has been included in the table as well.

Table 4.18 Final results of the complex parametric and optimization study. Best achievable phase shift, peak of transmission value and estimate for the focal length for each dielectric material are presented.

Dielectric material	Au/Dielectric/Au thicknesses (nm)	Peak transmission (%)	Phase shift, ϕ	$(64 \times 64)\lambda^2$ sample focal length (mm)
Sapphire	60/60/60	85	0.290π	5.56
Silicon nitride	60/120/60	76	0.520π	3.2
α -Si	30/120/30	47	0.592π	2.67

To the best knowledge of author there has been no other work in this direction except the report by Driscoll *et al.* in 2005 [5] in the microwave regime. Because of that we will compare results of our parametric study with the results reported by Driscoll. However, Driscoll never showed measurement results for the single layer lens, so we have to obtain those numbers using the information provided with in the paper and then make our comparison.

In order to make this comparison more visual and make it easier to read we will represent in the form of the Table 4.19. There results from Si_3N_4 and α - silicon base structures and the original Driscoll work are presented.

Table 4.19 Two best results of the complex parametric optimization study compared to the work reported by Driscoll *et al.*

	Driscoll [5]	Si_3N_4	$\alpha - \text{Si}$
Phase shift, ϕ	0.234π	0.520π	0.592π
Sample size, W	10.3λ	$(64 \times 64)\lambda^2$	$(64 \times 64)\lambda^2$
F number, f/W	11	32	26.7
Sample size/ wavelength, W / λ	10.3	64.5	64.5
Operating wavelength, λ	29 mm	1.55 μm	1.56 μm

If we take our best result based on the α - silicon dielectric fishnet GRIN metamaterial lens then we see that:

- We have demonstrated twice as large of an available phase shift for a single layer lens than the previous RF work;
- We have a large area sample and the ratio of sample size to the wavelength is high. That means that in our case we will have a much stronger confinement of

the beam and will not have edge effects problems like one will have for the sample with smaller ratio;

- We estimate our F number to be ~ 26.7 . However for the same sample size as reported by Driscoll (~ 10 wavelengths across) we can have an F number at ~ 4.7 . Also we see potential for significant improvement in F number by stacking a multiple layers of the NIM structure;

In the next section we will discuss the design of experiment.

4.4 Design of experiment

Imaging Interferometric Lithography (IIL) setup will be used to manufacture our experimental sample. Details about this setup and principal of IIL operations can be found in the Chapter 3 of this thesis. Using of this setup has its own advantages and some disadvantages. This is a mask based setup with the 22 x reduction system, which makes cost of masks low and their manufacturing process is very robust due to large scale features at the mask size. This setup can resolve individual lines down to 100 nm, which is within our resolution requirements. However, field of view of IIL setup is only 100 x 100 μm and this is a limiting factor. But for the purposes of initial demonstration this is perfectly suitable. In the future sample size can be significantly increased by switching to a 193 nm, 0.7NA lens system, which has a field of view of ~ 1 mm.

At first we will demonstrate convergence of the incident collimated beam for the one dimensional case. That means that gradient in the negative index will be along one axis of the sample as it schematically shown on the Figure 4.29.

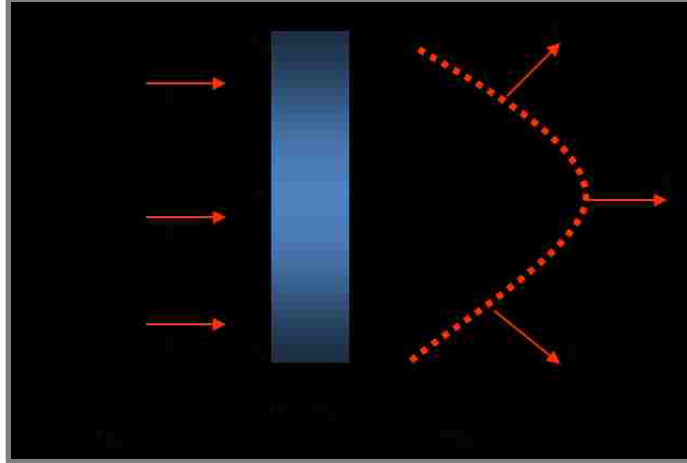


Fig. 4.29 Schematic illustration of the converging 1D gradient negative index metamaterial lens.

Index n_2 should be greater than n_1 , in order for our lens to be converging one. Also on this schematic illustration we have a continuous gradient in the index. However for the simplicity of our work we will create a step gradient at first. Number of steps can be increased and the step itself can be decreased in order to approach continuous gradient in the index. For the first experiment demonstration we will have 5 and 10 steps in our gradient. Figure 4.30 show overlapped “ideal” continuous and our stepped gradient index distribution across the sample.

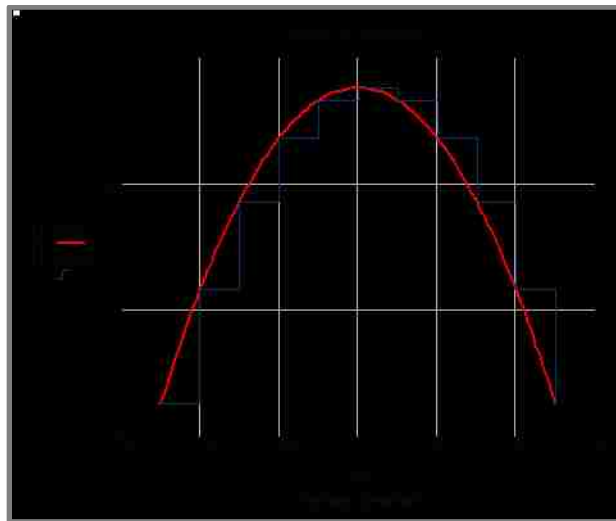


Fig. 4.30 Generated plot showing gradient index distribution across the sample. Red line shown continuous gradient in the index and the blue line represents 5 step index gradient for the experimental demonstration.

For the sample with 5 steps in the index we will have 16 unit cells per step and for 10 steps in the index, 8 unit cells/set will be produced.

Sample preparation and exposure were done following the lithographical procedures described in great details in the Chapter 3 of this thesis. Once the sample was developed and examined under the Scanning Electron Microscope (SEM) it was transferred in the cleanroom for further processing. In the cleanroom PR pattern on the top of the sample will be etched in the anti-reflection layer. Then the metal deposition and a lift-off process will be performed in order to create a hard mask on the top of the sacrificial layer. Once the mask is formed it will then be etched in that layer. Next step will include 2 metal and 2 dielectric evaporations followed by the stripping of the sacrificial layer. This way fishnet patterned metal/dielectric/metal structure will be formed on the top of the substrate.

Sapphire based metamaterial structure was chosen for the first experimental demonstration because at the moment cleanroom facilities and it's equipment provides much better control over the dielectric deposition of the Sapphire material than any other. Also, having a relatively low refractive index, $n = 1.75$, in the dielectric let us have a large pitches and CD of the fishnet structure.

From the results obtained in the previous sections we found out that for the Au/Sapphire/Au layers structure with thicknesses of 60/60/60 nm we can get transmission of ~ 0.85 with the phase shift of $\sim 0.290 \pi$. For the 5 step gradient index at the resonance wavelength of 1.55 μm we generate transmission and effective refractive index plots that can be found on the Figure 4.31.

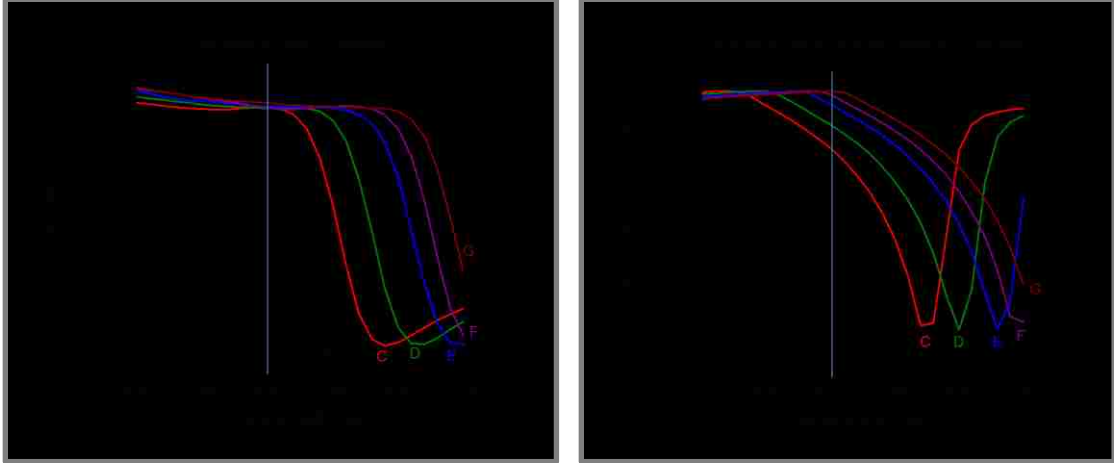


Fig. 4.31 Designed and RCWA calculated transmissions (left) and effective refractive index (right) responses of the 5 step gradient negative index metamaterial lens. Dielectric material is sapphire and Au/Sapphire/Au layers have thicknesses of 60/60/60 nm. Resonance wavelength of 1.55 μm is assumed.

Table 4.20 show physical parameters used to generate each curve in this set as well as transmission, modeled (according to Figure 4.30) and designed (according to RCWA calculations) effective refractive index.

Table 4.20 List of geometrical parameters used to calculate transmission and effective refractive index curves shown on the figure 4.31. Transmission, modeled and designed refractive index values at the resonance wavelength of 1.55 μm .

Curve	Pitch (a_x, a_y), nm	CD d_x , nm	CD d_y , nm	T	n, modeled	n, designed
B	665	332	100	0.795	-1.35	-1.35
C	677	338	100	0.839	-0.907	-0.906
D	689	345	100	0.840	-0.563	-0.579
E	701	350	100	0.846	-0.317	-0.306
F	709	355	100	0.842	-0.169	-0.171
G	715	357	100	0.858	-0.12	-0.125

For 10 steps in the gradient additional curves will be added in between calculated ones, making just smaller steps between edge curves B and G.

Last step in the design of the experiment will be test of exposure parameters in the PROLITH™ modeling software. In this software tool we can simulate stack thicknesses of the sacrificial layer (PMMA in this case), anti-reflection coating (ARC) and photoresist (PR) as well as off-axis illumination schemes. Results of this simulation will be presented in the form of an aerial image, PR image and plots of intensity crosscuts in the orthogonal directions.

Four by four unit cells mask was designed as a test subject for the simulation. This mask and its Fourier transformation with applied off-axis illumination are shown on the Figure 4.32.

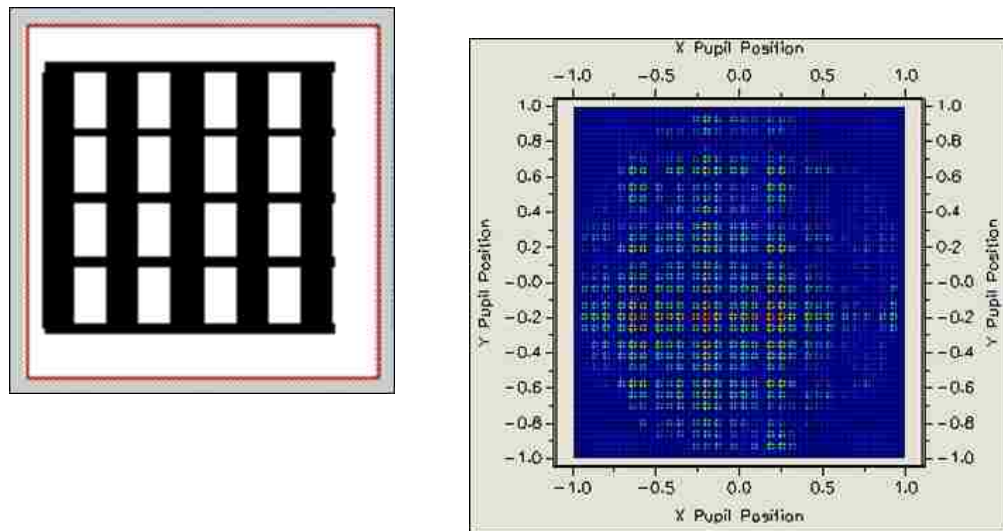


Fig. 4.32 4 x 4 mask designed as a test subject in the PROLITH™ simulations (left) and its Fourier transformation with applied off-axis illuminations at $-0.2 NA$ in the x and y directions (right).

Single pass exposure was used to generate an aerial image of the mask. Then it was transferred in the PR layer and final image of the developed pattern was generated. These aerial and developed pattern images are shown on the Figure 4.33.

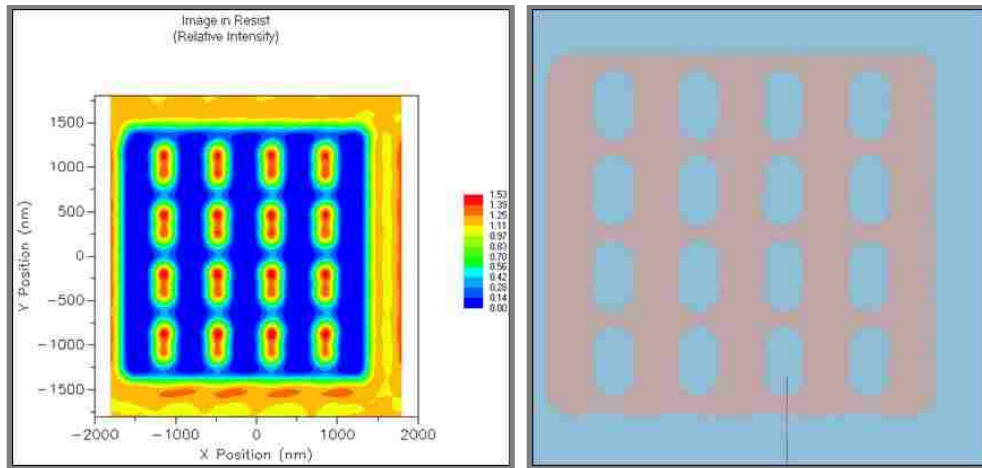


Fig. 4.33 Aerial image (left) and developed PR pattern (right) of the 4 x 4 mask generated in the PROLITH™ simulation software. Good resolution of the lines in both x and y direction is observed.

If one should take a crosscut of the aerial in the two orthogonal directions than plots of intensity variation vs. position can be generated. Those plots are presented on the Figure 4.34.

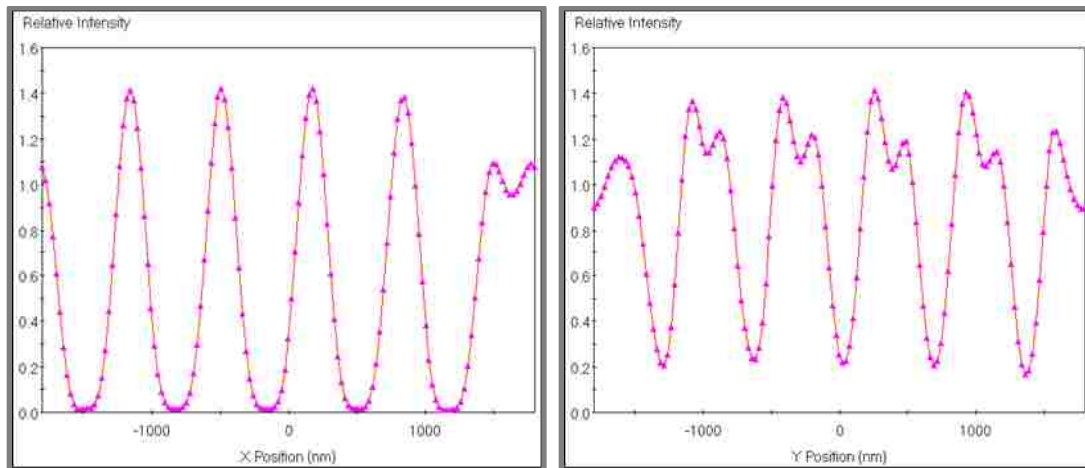


Fig. 4.34 Crosscuts of the Aerial image (see fig.4.33) in the x and y directions shown a very good line/space resolution. This indicates that our stack and illumination scheme were chosen correctly.

Aerial image, PR developed pattern and crosscuts shows a very good resolution and successful image transfer indicated that our film stack and illumination scheme were chosen correctly.

Demonstration of the preliminary experimental results and there discussion can be found in the Chapter 5.

4.5 Conclusions

Theoretical numerical calculations for the *first gradient index optical lens with inhomogeneous NIM structure operating at $\sim 1.55 \mu\text{m}$* have been demonstrated. Parametric studies and the optimization process for the maximum achievable phase shift with smallest variation in transmission have been demonstrated. A simple and reliable technique known as imaging interferometric lithography – IIL [13] was proposed for the fabrication of the experimental samples.

Table 4.21 shows result of the complex numerical parametric study demonstrated in this Chapter compared to the only experimental demonstration of the NIM lens performed by Driscoll *et al* [5] in 2006. Our numerical model demonstrates higher achievable phase shift and advance in the operation wavelength from RF in the IR regimes.

Table 4.21 Result of the numerical parametric study in the form of optimized fishnet structure based on α -silicon compared to the only experimental demonstration reported by Driscoll *et al* in 2006.

	Numerical model	Driscoll's experiment
Wavelength, λ	$\sim 1.56 \mu\text{m}$	$\sim 29 \text{ mm}$
Phase shift, ϕ	0.592π	0.234π
Sample size, W	$(64 \times 64)^2 \lambda$	10.3λ
F number, f/W	26	11

Experimental samples with a $(64 \times 64) \lambda^2$ area (matching our lithographic capabilities) will have small edge effects due to a large sample size/wavelength ration and acts as $f/26$ lens, for the α -silicon optimized fishnet structure. Driscoll *et al* has

reported a 0.234π phase shift across the 10.3λ diameter sample which acts as $f/11$ lens, in our case, for the compatible size sample, $f/4.7$ lens can be achieved. We see a potential improvement in the value of the f number by stacking a multiple layer of the NIM structure.

Experimental demonstration of the lens effect by the means of inhomogeneous metamaterial structures will be a significant step towards possible applications for the NIM, as well as an advance in design complexity and construction techniques. Future work that could be done in this direction is discussed in the Chapter 5.

4.6 References

- 1 V. G. Veselago, "The electrodynamics of substances with simultaneously negative values of ϵ and μ ," Sov Phys. Uspekhi **10**, 509 (1968).
- 2 D. R. Smith, W. J. Padilla, D. C. Vier, S. C. Nemat-Nasser, and S. Schultz, "Composite medium with simultaneously negative permeability and permittivity," Phys. Rev. Lett. **84**, (2000).
- 3 S. Zhang, W. Fan, N. C. Panoiu, K. J. Malloy, R. M. Osgood and S. R. J. Brueck, "Experimental demonstration of near-infrared negative-index metamaterials," Phys. Rev. Lett. **95**, (2005).
- 4 G. Dolling, M. Wegener, "Negative index metamaterial at 780 nm wavelength", Optics letters **32**, 1 (2007)
- 5 T. Driscoll, D.N. Basov, A.F. Starr, P.M. Rye, S. Nemat-Nasser, D.Schurig and D.R. Smith, "Free space microwave focusing by a negative-index gradient lens", Appl. Phys. Lett. **88**, (2006).
- 6 S. Zhang, W. Fan, N. C. Panoiu, K. J. Malloy, R. M. Osgood, S. R. J. Brueck, "Demonstration of metal–dielectric negative-index metamaterials with improved performance at optical frequencies", J. Opt. Soc. Am. B **23**, 3 (2006).
- 7 S. Zhang, W. Fan, K. J. Malloy and S. R. J. Brueck, N. C. Panoiu and R. M. Osgood, "Near-infrared double negative metamaterials," Opt. Express **13**, 13 (2005).
- 8 Z. Ku and S. R. J. Brueck, "Comparison of negative refractive index materials with circular, elliptical and rectangular holes," Opt. Express **15**, 8 (2007).
- 9 M. G. Moharam and T.K. Gaylord, "Rigorous coupled-wave analysis of planar-grating diffraction," J. Opt. Soc. Am. **71**, (1981).

-
- 10 B. K. Minhas, W. Fan, K. Agi, S. R. J. Brueck and K. J. Malloy, “Metallic Inductive and Capacitive Grids: Theory and Experiment,” *J. Opt. Soc. Am. A* **19**, (2002).
- 11 D. R. Smith and S. Schultz, “Determination of effective permittivity and permeability of metamaterials from reflection and transmission coefficients,” *Phys. Rev. Lett.* **B 65**, (2002).
- 12 M. A. Ordal, L. L. Long, R. J. Bell, S. E. Bell, R. R. Bell, R.W. Alexander, and C. A. Ward, “Optical properties of the metals Al, Co, Cu, Au, Fe, Pb, Ni, Pd, Pt, Ag, Ti and W in the infrared and far infrared,” *Appl. Opt.* **22**, (1983).
- 13 S. Smolev, A. Biswas, A. Frauenglass and S. R.J. Brueck, “244-nm imaging interferometric lithography test bed”, *Proc. SPIE* **6154**, (2006).

Chapter 5 Future Work

5.1 Potential application for the hybridization of magnetic and dipole resonances

As discussed in the Chapter 2, we have experimentally and numerically demonstrated a new effect of magnetic hybridization of the electric dipole resonance in the metamaterial structure. This effect is of interest from the fundamental physical point of view because the presence of the *electric dipole* resonance in the dielectric of the fishnet structure manifest itself in a modification of the *magnetic permeability* (structural resonance), which in turn modifies the negative index of refraction.

Usually we do not have a coupling of the electric dipole resonance in the magnetic resonance, but the interesting physics of the negative index metamaterials opens that possibility. We have constructed a good numerical model that will allow us to investigate this phenomenon more deeply and increase it understanding.

Wavelength regime where coupling effect was demonstrated is attracting a lot of attention in the research community for different number of applications. At the long wavelength infrared (LWIR) there is a peak of black body radiation which can be used for defense and security as well as medical applications. It is logical to extend our work from the fundamental to application points. We think that this hybridization may allow construction of some optical switches or some novel optical sensors. Model for this optical sensor can be constructed and some comparing with the existing sensors needs to

be performed in order to understand if use of the hybridization effect can provide any advantages.

All that should be addressed in the future work and would be a next step in understanding and expanding of demonstrated hybridization effect.

5.2 Experimental demonstration of the GRIN optical lens

Here we demonstrate preliminary results for the 1 dimensional GRIN slab lens in the form of scanning electron micrograph (SEM) images of inhomogeneous structure transferred in the photoresist layer.

Figure 5.1 demonstrates the SEM image for the fishnet structure that is transferred in the photoresist pattern with the physical parameters: $a_x = a_y = 687$ nm; $d_x = 340$ nm, $d_y = 100$ nm.

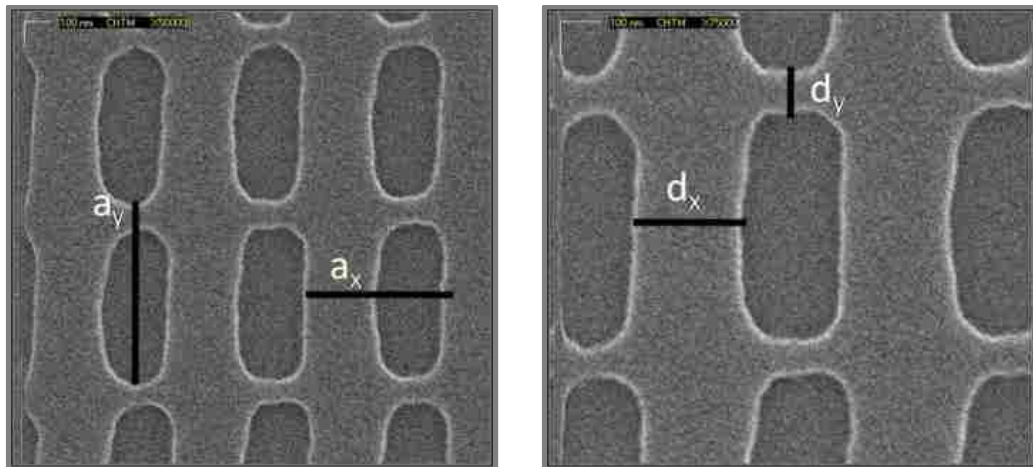


Fig. 5.1 SEM images of first preliminary experimental sample demonstrating inhomogeneous fishnet structure transferred in photoresist with marked physical dimensions $a_x = a_y = 687$ nm; $d_x = 340$ nm, $d_y = 100$ nm. Good resolution and adequate overall uniformity is observed.

Photoresist images show very good resolution for the required minimal dimensions. We see that our image has some distortion: we have holes that have a shape of rectangular with rounded corners; some of the holes have some astigmatism. We would

like to address those issues in the future work in particular, see the effect of hole roundness on the performance of our structure.

Figure 5.2 shows the SEM images of inhomogeneous fishnet structure transferred in photoresist. Here *stitching* of two homogeneous regions in the one inhomogeneous area is demonstrated. Region A have structure with dimension $a_x = a_y = 687$ nm, $d_x = 340$ nm, $d_y = 100$ nm; while region B have structure with dimensions $a_x = a_y = 705$ nm; $d_x = 350$ nm, $d_y = 100$ nm. These two homogeneous regions set one next to another create inhomogeneous structure on the large scale.

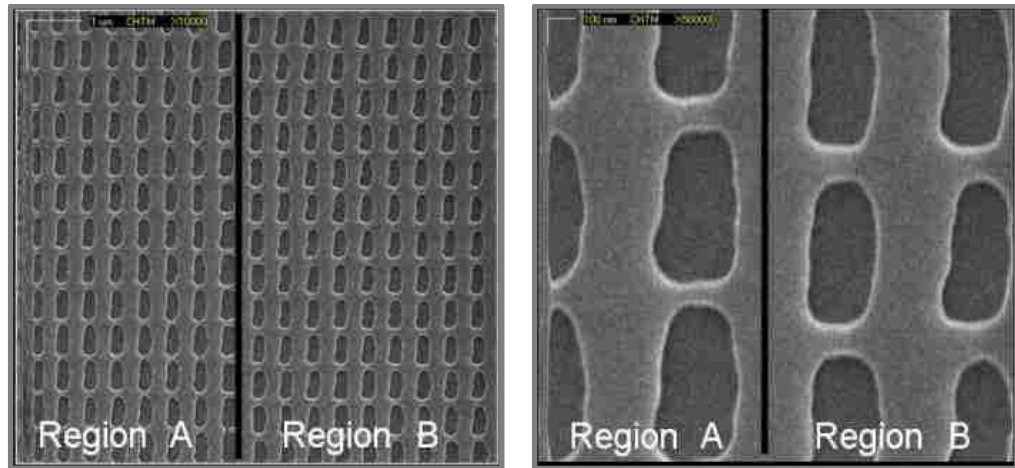


Fig. 4.36 SEM images of inhomogeneous fishnet structure created by *stitching* two homogeneous regions a ($a_x = a_y = 687$ nm, $d_x = 340$ nm, $d_y = 100$ nm) and b ($a_x = a_y = 705$ nm, $d_x = 350$ nm, $d_y = 100$ nm). Photoresist patterns shows very good resolution of minimal dimensions, adequate overall uniformity and defect free overlapping of regions A and B.

Photoresist images show good resolution of required minimal dimensions and have a defect free overlapping of regions A and B. However some of the holes are distorted and we see a room for the improvement that can be addressed in the future work.

Next step in sample processing will require complex cleanroom processing including metal deposition, lift-off, etching and pattern transfer in the sacrificial layer.

Follow by the metal/dielectric/metal depositions. This work along with creation of the experimental setup and the focal length measurement for the grin lens could be also addressed in the future work.

5.3 Imaging Interferometric Lithography

We have experimentally demonstrated the 244 nm, 0.9 NA Imaging Interferometric Lithography optical tool with ultimate resolution limit, for the arbitrary pattern, of $\sim \lambda/3NA$ without use of any Resolution Enhancement Techniques.

As the future work we plan to optimize the exposure parameters for the 3-exposure IIL, continue experiments with the illumination scheme using ND attenuation of the zero order beams in the high frequency exposures and evaluate the resolution limit of the optical system. Also because with the first introduction of the ND attenuation scheme we did not investigate the effect of the phase change of the zero order beam as it passes through the ND files, we think that this issue need to be addressed in the future work. We would like to print different patterns on the current setup, such as via holes. We would like to check the resolution capabilities of the optical system in printing dense arrays of via holes as well as printing isolated features. This will address the challenges that industry is currently facing.

As a next step we would like to extend existing setup to the 193 nm laser source and a 1.05 (1.35) NA immersion lens. At this setup new resolution limits as well as polarization and hyper-NA effects can be investigated.

Appendix A

During course of this work results demonstrated in this dissertation were presented at following peer-reviewed conferences and workshops:

- Dr. Julie Bently, Christian J. Schwarz, S. Smolev, S.R.J. Brueck: Printing 0.1 mm structures with a 244nm μ CATTM Cheetah Objective using Imaging Interferometric Lithography. SPIE Advance Lithography meeting, February, 2003.
- A. Fraunglass, S. Smolev, A. Biswas and S. R. J. Brueck: 244 – nm imaging interferometric lithography. The 48-th International Conference on Electron, Ion and Photon Beam Technology and Nanofabrication (EIPBN), June, 2004.
- Svyatoslav Smolev, A. Biswas, A. Frauenglass and Steven R.J. Brueck: 244 – nm imaging interferometric lithography test bed. SPIE Advance Lithography meeting, February, 2006.
- Svyatoslav Smolev and S. R. J. Brueck: Graded index optical lens using inhomogeneous metamaterial. The Conference on Lasers and Electro-Optics (CLEO) and The International Quantum Electronics Conference (IQEC), May, 2008.
- Svyatoslav Smolev and S. R. J. Brueck: Graded index optical lens using inhomogeneous metamaterial. The 45th NMAVS Symposium on *Nanomaterials: Science and Technology*, May, 2009.

- S. Smolev, Zahyun Ku, S. R. J Brueck, I. Brener, M.B. Sinclair, G. A. Ten-Eyck, W. L. Langston, and L.I. Basilio: Resonant coupling to a dipole absorber inside a metamaterial: anti-crossing of the negative index response. The Third International Congress on Advanced Electromagnetic Materials in Microwaves and Optics - *Metamaterials 2009* (Metamorphose), September, 2009.
- S. Smolev, Zahyun Ku, S. R. J Brueck, I. Brener, M.B. Sinclair, G. A. Ten-Eyck, W. L. Langston, and L.I. Basilio: Resonant coupling to a dipole absorber inside a metamaterial: hybridization of the negative index response. Material Research Society (MRS) Spring, 2010 meeting.
- S. Smolev, Zahyun Ku, S. R. J Brueck, I. Brener, M.B. Sinclair, G. A. Ten-Eyck, W. L. Langston, and L.I. Basilio: Resonant coupling to a dipole absorber inside a metamaterial: hybridization of the negative index response. The Conference on Lasers and Electro-Optics (CLEO) and The International Quantum Electronics Conference (IQEC), Spring, 2010 (accepted).
- S. Smolev, Zahyun Ku, S. R. J Brueck, I. Brener, M.B. Sinclair, G. A. Ten-Eyck, W. L. Langston, and L.I. Basilio: Experimental demonstration of resonant coupling to a dipole absorber inside a metamaterial: hybridization of the negative index response. The 54-th International Conference on Electron, Ion and Photon Beam Technology and Nanofabrication (EIPBN), Summer, 2010 (accepted).

WORKSHOPS

- S. Smolev and Steven R. J. Brueck: Graded index optical (1.55 μm) lens using inhomogeneous metamaterials. Aspen Metamaterial Workshop, September, 2008.

Also results of this work we published in:

- A. Frauenglass, S. Smoley, A. Biswas, and S. R. J. Brueck: 244-nm imaging interferometric lithography., *J. Vac. Sci. Technol. B* Volume 22, Issue 6, pp. 3465-3469, November (2004).
- Svyatoslav Smoley, A. Biswas, A. Frauenglass and Steven R.J. Brueck: 244-nm imaging interferometric lithography test bed. *Proceedings of SPIE 6154*, 61542K (2006).
- S. Smoley and S. R. Brueck, "Graded Index Optical Lens Using Inhomogeneous Metamaterials," in *Conference on Lasers and Electro-Optics/Quantum Electronics and Laser Science Conference and Photonic Applications Systems Technologies*, OSA Technical Digest (CD) (Optical Society of America), paper CThBB4 (2008).

Currently articles for the: Gradient index optical lens using inhomogeneous metamaterials and Experimental demonstration of resonant coupling to a dipole absorber inside a metamaterial: hybridization of the negative index response are being prepared for the publication.